January 2019

Novel Cathode Framework, Effective Electrolyte Modification, And Electrode Structural Modification Of High Performance Lithium Sulfur Batteries

Wenduo Zeng
Wayne State University, zengwenduo@foxmial.com

NOVEL CATHODE FRAMEWORK, EFFECTIVE ELECTROLYTE MODIFICATION, AND ELECTRODE STRUCTURAL IMPROVEMENT OF HIGH-PERFORMANCE LITHIUM SULFUR BATTERIES

by

WENDUO ZENG

DISSERTATION

Submitted to the Graduate School

of Wayne State University,

Detroit, Michigan

in partial fulfillment of the requirements

for the degree of

DOCTOR OF PHILOSOPHY

2019

MAJOR: MATERIALS SCIENCE

Approved By:

_____

Advisor Date

_____

_____

_____

_____

DEDICATION

To my parents and their unconditional love and support

ACKNOWLEDGEMENTS

Above all, I would like to express my deep gratitude to my advisors, Dr. Simon Ka-Yuen Ng, and Dr. Mark Ming-Cheng Cheng for their patience, advice and support, for which I am extremely grateful. This thesis would not have been possible without their enlightenment, encouragement, and continuous optimism.

I would also like to acknowledge my committee member, Dr. Gholam-Abbas Nazri, Dr. Da Deng, and Dr. Steven Salley for the friendly guidance, constructive suggestions contributions and their valuable time serving on my committee.

I would like to thank all my friends and colleagues, who have supported me along the way, Dr. Junheng Xing, Dr. Xinghua Meng, Dr. Jian Zhu, Mr. Wissam Fawaz, Mr. Zhao Wang, and Mr. Zhuolun Tang for their help and the great friendship that make it enjoyable time in the lab.

Last, but not least, I greatly thank my parents, Ke and Funian. Their love, support, understanding and encouragement, helped me through the hard times of this program.

TABLE OF CONTENTS

LIST OF TABLES

LIST OF FIGURES

1 CHAPTER 1 INTRODUCTION

1.1 Science and technology of batteries

Through electrochemical reactions, batteries are the devices to store chemical energy and convert into electrical energy as power supply.[1] The conventional configuration of a battery cell is composed of a positive electrode, a negative electrode, a porous polymer membrane as separator between two electrodes, and a media as ionic conductor (electrolyte).[2] Two chemical reactions happen at positive and negative electrodes separately, where oxidative agents will be reduced at positive electrode (cathode), and reductive agents will be oxidized at negative electrode (anode). In the meantime when ions flow in electrolyte through separator, the electrons will be transferred through the external circuit. The current is generated and power is provided to electrical appliances, such as electric vehicle (EV) and portable devices like laptops and cellphones.[3] The batteries are divided into two main categories based on their properties: primary and secondary batteries. Primary batteries could be considered as non-rechargeable items, as their electrochemical reactions are irreversible.[4] The discharging process starts when the cell provides power supply from the oxidation of the anodes and the reduction of the cathodes, enabling the active materials to have a one-time discharge only. The commonly used primary batteries are alkaline, lithium, silver oxide and zinc air cells. Secondary batteries are also called rechargeable batteries.[5] Since the redox reactions are reversible, the flow of ions through electrolyte could be moved forth and backwards as the electrons could from cathode to anode through external circuit or vice versa (charging and discharging). Nowadays, many secondary batteries have been commercialized, including Lead Acid, Nickel Cadmium, Nickel Metal Hydride, and Lithium ion batteries.

1.1.1 Lead Acid batteries

The electrochemistry of lead acid batteries is developed for decades and its principle has been understood well now.[6] Even though its excellent properties of low-cost, high power density and wide temperature-range of usage, the severe drawbacks limit its further applications such as low stability and specific energy. Furthermore, the use of lead is strongly against the environmentally-friendly operation if not handled properly. The application of such kind batteries is usually falling in such different fields: Starter in vehicles and crane used power supply.

1.1.2 Nickel cadmium batteries

The usage of nickel cadmium batteries is usually suitable for small-sized digital products or devices requiring power supply.[7] The cell of nickel cadmium batteries is composed of a nickel oxide hydroxide cathode, and a cadmium metal anode, as well as a potassium hydroxide contained alkaline electrolyte. There are several attractive aspects of nickel cadmium battery making it surpassing other rechargeable batteries. However, the cost of raw materials for nickel cadmium is quite high. And the operation and disposal of toxic cadmium also requires a lot of attention.

1.1.3 Nickel metal hydride batteries

The electrochemistry of nickel metal hydride battery is based on the cell configuration similar to the that of nickel cadmium batteries.[8] The cathode is nickel oxide hydride while the difference is that the anode is hydrogen-absorbing alloy instead of cadmium metal. The characteristics of nickel metal hydride batteries is well suited in many applications, such as consumer electronics and EV. As for small rechargeable batteries, the

nickel metal hydride batteries could be considered as an alternate to replace nickel cadmium batteries.

1.1.4 Lithium ion batteries

The higher energy density of lithium-ion battery has a great potential for wide applications.[9] Usually, the cathode of lithium ion batteries is lithium-containing compound and the anode is graphite. There are many advantages of li-ion battery, including but not limited to low self-discharge, higher energy density and low maintenance due to no memory effect compared to Ni-metal batteries. On the contrary, disadvantages like aging, protection of overcharging and under-developing technologies currently limits its further applications.

1.1.5 Lithium sulfur batteries

Due to the theoretical limitation of energy density of conventional lithium ion batteries, the need of developing next generation batteries is urgent to meet the rapidly growing requirement of EV driven range.[10] Compared to lithium ion batteries, lithium sulfur batteries own an almost ten-fold energy density, ~2700 Wh Kg^{-1}, with a brand electrochemistry. Also, it benefits from non-toxicity and low cost as well. In lithium sulfur batteries, the sulfur incorporated with conductive matrix is acting as the cathode due to its insulating nature, and lithium metal is used as anode. Unfortunately, it has several technological challenges to overcome such as low stability, high self-discharge and capacity fading. More electrochemistry will be discussed in chapter 2.

1.1.6 Lithium air batteries

The design of lithium air batteries is quite similar to lithium sulfur batteries. The notable difference is that oxidizing agent on cathode has replaced by oxygen to make use

of its higher energy density than sulfur.[11] Technically, the combination of lithium metal and oxygen generates the highest energy density. However, it still suffers from shortcomings like practical power output and endurable cycle life to meet the requirements of a real market. With these challenges being tackled, the lithium air batteries should have a promising future due to its marvelous intrinsic electrochemical property.

1.2 Scope of the dissertation

Limited by the specific energy and power of lithium ion batteries, and its lack of capability of keeping pace up with the growth of electric/hybrid electric vehicle (EV/HEV) industry, alternate next generation lithium battery system is being researched to replace the conventional lithium ion battery.[12-14] Although some researchers have been proposing new techniques and novel materials to improve and widen the applications of lithium ion battery, lots of attention and interest have been attracted to the field of alternate energy storage and conversion systems beyond current electrochemical systems. Among all the options considered, the lithium sulfur battery stands out for its excellent performance and advantages.[15-17] The specific energy of lithium sulfur batteries is about five-fold of that of conventional lithium ion batteries with sulfur material as an inexpensive and safe raw material due to its natural abundance and non-toxicity. In spite of all the obvious outstanding superiorities of lithium sulfur batteries, it still suffers from some intrinsic drawbacks limiting its further development and practical applications. Disadvantages, such as low cyclability, decreased conductivity and high self-discharge, significantly hinders the lithium sulfur batteries to achieve applicable electrochemical performance. In this work, rational design of cathode material, protection of lithium anode and electrode structural modification were investigated

as an approach to deliver a lithium sulfur battery with outstanding performance and enhanced stability.

Firstly, TiN nanotube arrays have been investigated as a cathode framework to improve lithium sulfur battery performance from several aspects. TiN exhibited several outstanding properties such as its high chemical and thermal stability, superior electrical conductivity, and their capability of trapping the soluble polysulfides. Moreover, we applied for a facile method of synthesizing nanotube arrays grown on Ti metal foil. Thus, the cathode material was investigated its superiority in lithium sulfur batteries, and also the effect of nanotube arrays dimension, nanotube diameter and length, was testified on the battery performance.

To develop a practical method of further decreasing the drawback of capacity fading, hybrid structured cathode material, nanostructured TiN with graphene, were synthesized. TiN nano-particles/tubes with graphene were studied as a conductive cathode framework in lithium sulfur batteries. Furthermore, the hybrid cathode framework with various ratio of TiN nanotubes and graphene were studied. It is evident that the battery performance, cycling stability, charge transfer impedance change, and sulfur content retention were characterized for charging/discharging process. Therefore, an optimal ratio was then proposed.

As the volume change during cycles due to density difference between sulfur and its lithiated product is one of major issues causing rapid capacity fading and low cyclability in lithium sulfur batteries, the research was extended to the level of cell structural design from merely the electrochemistry. In order to accommodate the intense internal stress of electrodes, especially to cell with thicker active material film, the structural design was

modified with buffer layer. Between active material film and current collector, this structural modification was able to show an improvement compared to conventional ones.

Lastly, the effect of a group of electrolyte additives of transition metal acetate on battery performance and cycling stability on lithium sulfur batteries were investigated. Copper acetate has been reported to be able to promote the formation of a smoother, stronger, and more stable and homogeneous solid electrolyte interface (SEI) film on lithium metal anodes. In our study, the research has covered a wider range of transition metal as salt cations to study their different capability of forming metal sulfide, which could contribute to the stability of SEI film. Moreover, electrochemical quartz crystal microbalance was used to study the mass change of lithium anode during cycles.

1.3 Significance of research

Lots of researchers has proposed numerous techniques to improve lithium sulfur battery performance and stability. It should be noted that scientific realization of battery technology can greatly minimize the manufacture cost, enhance cycling stability, and reduce safety issued caused by conventional method and chemistry. This technological advancement could strongly and positively affect the following fields.

Currently, lithium ion battery is widely used in portable electronics and EVs. Nevertheless, the module or pack of lithium ion batteries in EVs is count as more than 50% of overall cost of vehicle. To become a powerful competent over the conventional gasoline-powered vehicle, the cost reduction significantly needs to be addressed with an alternate battery system with lower cost compared to today`s lithium ion batteries. Benefitting from the natural abundance of sulfur element, engineering of lithium sulfur batteries could solve the manufacture issue of high cost.

Moreover, better appliance with larger scale energy storage and longer driving range of EV keeps demanding for a higher energy density and specific energy. Therefore, the lithium sulfur battery stands out for its high theoretical specific energy compared with to its competent, providing a potential of satisfying gradually increasing needs. The employment of sulfur as novel cathode material serves as one important aim to optimize the battery performance and further realize practical applications.

Furthermore, the decreasing natural storage of oil and gas has attracted the emphasis of importance on developing novel alternate energy system. The trend will drastically affect countries like US, which gasoline usage is more than one fourth of the global oil consumption. The prosperity of new electrochemical system can serve as an outstanding supplement to fossil fuel and enhancement to the social economics worldwide. Also, less usage of fossil fuel could significantly reduce the emission of green-house gases, which could notably mitigate the severe global warming nowadays.

2 CHAPTER 2 LITERATURE REVIEW AND BACKGROUND INTRODUCTION

2.1 Li-S battery

Lithium sulfur batteries is attractive in the market of rechargeable battery due to their theoretical specific energy of around 2700 mAh g^{-1}, which is nearly 10 times higher than those of lithium ion batteries (LIB).[18] Moreover, the advantages of low-cost and non-toxicity exhibit critical attractiveness, compared to cobalt, nickel, and manganese used in LIBs.[19-20]

2.2 Cell configuration and electrochemistry of Li-S batteries

Fig.1 depicts a typical configuration of lithium sulfur battery, which is composed of cathode containing sulfur, lithium anode and electrolyte between two electrodes and current collectors as media for electron transfer.

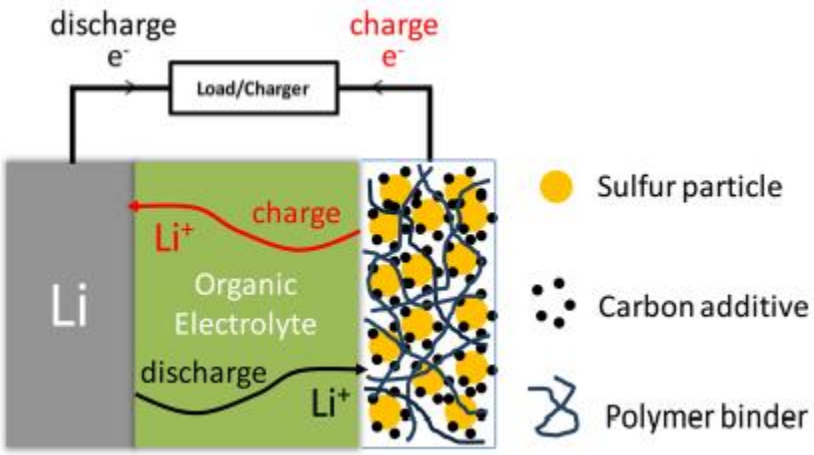

Figure 2.1 Schematic diagram of a Li−S cell with its charge/discharge operations.[21]

The battery would demonstrate a maximum voltage when no outer circuit is connected, which is referred as open circuit voltage and directly related to the difference of reduction potentials of lithium and sulfur elements. Actually, there are two different

configurations of lithium sulfur batteries, although they do share the basically same electrochemistry process. Both cell configurations can employ either liquid electrolytes or solid electrolytes. In the most common configuration investigated thus far, lithium metal serves as the negative electrode and is electrochemically coupled with sulfur as the positive electrode.[22-23]

Once discharging process starts, lithium ions move spontaneously through the electrolyte from the negative electrode to the positive electrode while electrons flow through the external circuit, providing electrical energy. Thus, sulfur reacts with lithium by a two-electron reduction process to form polysulfide intermediates (Li_2S_x, x=2~8), and eventually introduce the generation lithium sulfide (Li_2S) at the end of discharge as the final reduced product. Although solid sulfur (S_8 is the most stable form at standard temperature and pressure) is employed in most cases as the electrode material, the solid sulfur is reduced to form polysulfides at the beginning of discharge. These polysulfides are soluble in many organic solvent based electrolytes.[24-26] In fact, lithium/sulfur cells were explored as electrochemical power sources employing a liquid polysulfide positive electrode, although the fully oxidized state (S_8) and the fully reduced state (Li_2S) are solid. Actually, based on these thoughts, some previous researchers were studying the function and performance of so called “flow cell”, in which the sulfur element has already been dissolved into the electrolyte while electrocatalytic-active material is employed at the corresponding cathode area.[27-28]

When S_8 is being subjected to electrochemical reduction in discharging, two plateaus could be observed in discharge curve, or sometimes three plateaus based on the selection

of electrolytes. Typical cyclic voltammograms and charge–discharge profiles of lithium/sulfur cells are shown in Fig. 2.

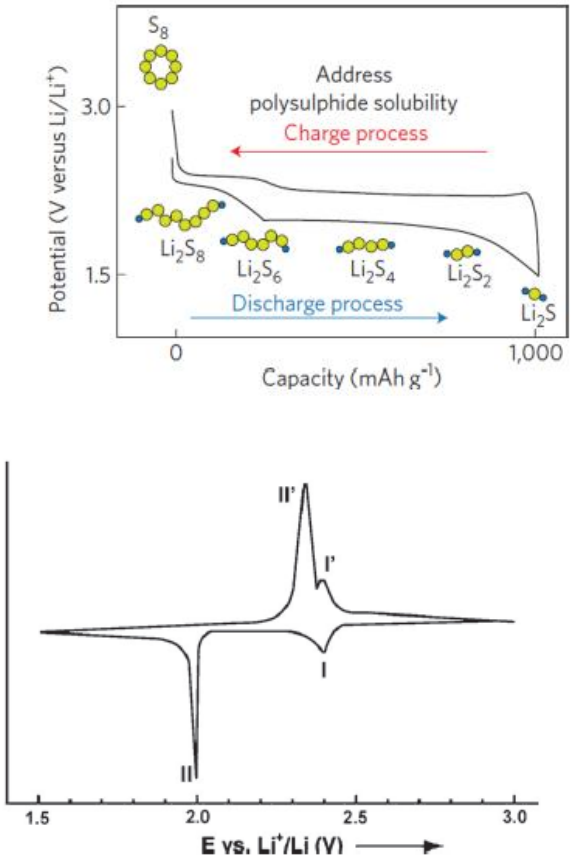

Figure 2.2 Typical charge–discharge profiles and cyclic voltammograms of lithium/sulfur cells.[21, 29]

During the cathodic scan of Fig. 2, two main reduction peaks at around 2.4 and 2.05 V appear. The peak at about 2.4 V can be assigned to the reduction of elemental sulfur to higher-order polysulfides (Li_2S_n, $n \geq 4$). The peaks at about 2.05 V correspond to the further reduction of high-order polysulfides to low-order polysulfides (Li_2S_n,$1< n < 4$) and Li_2S. Similarly, during the constant-current discharge of Fig. 2, in general, two or three plateaus

are observed. The high-voltage plateau (2.4 V) is related to the reduction of elemental sulfur to the higher-order lithium polysulfides (Li_2S_n, $n \geq 4$).

$$S_8 + 2Li \rightarrow Li_2S_8$$

$$Li_2S_8 + 2Li \rightarrow Li_2S_6$$

$$Li_2S_6 + 2Li \rightarrow Li_2S_4$$

Further reduction of high-order polysulfides (Li_2S_n, $n < 4$) to low-order polysulfides (Li_2S_n, $n < 4$) and lithium sulfide occurs at the low-voltage plateau around 2.05 V.

$$Li_2S_4 + 2Li \rightarrow Li_2S_2$$

$$Li_2S_2 + 2Li \rightarrow 2Li_2S$$

Since the near insolubility and thus relatively slow reaction kinetics of Li_2S_2 in conventional conditions, final reduction step of Li_2S_2 being further reduced to Li_2S might not be complete. To date, the detailed mechanistic procedure of the electrochemical reduction process of lithium polysulfides are very complex and need deeper understanding. Reaction pathways may be also quite different depending on the composition of the electrolyte, due to the reaction between electrolyte component and electrode and different solubility for various polysulfides in electrolytes.[25, 30-31]

2.3 Technological barriers of Li-S batteries

Although lithium sulfur batteries have been widely recognized as the next generation lithium batteries, several disadvantages still hinder its more industrial applications. Obstacles of low cyclability, low utilization of active material sulfur, and suppressed efficiency are discussed in detail in this section.[32-33]

2.3.1 Low conductivity of cathode material

The overall capacity of lithium sulfur batteries strongly depends on the sulfur cathode. But, sulfur itself and some intermediate polysulfides formed during charging/discharging reactions is nearly insulating. As a result of very poor electrical conductivity, there is a necessity of constructing a conductive framework for sulfur cathode.[34-38] These cathode additives not only need to exhibit an outstanding electrical conductivity, but also a superior ionic conductivity to facilitate lithium ion transportation within the cathode network. A possession of vacant pores could provide sufficient electrolyte accessibility to active material to enhance the efficiency of redox reactions. Furthermore, this conductive matrix should be able to retain its structural completeness and stability over cycles. The internal stress generated, because of volume shrinkage and expansion, should effectively suppress to maintain its conductive path for electrons and ions. Last, thermal and chemical stability is an important property here.

2.3.2 Volume expansion

It is reported that elemental sulfur and lithium sulfide have different densities of 2.1 and 1.7 g cm^{-3} respectively, the expansion of volume observed in lithium sulfur battery system would be up to nearly 80% during cycling.[39-40] The drastic volume change in structure will induce internal stress, which could result in severe mechanical fracture and failure. This mechanism will also impair the overall conductivity of the framework and cause rapid capacity decay and low cycling stability. The factors to accommodate the volume change is including the mechanical strength of cathode framework, pore size of matrix and structural design, etc.

2.3.3 Shuttle reactions

During the discharging procedure, long-chain higher order polysulfides would be reduced to lower order polysulfides.[41] It should be noted that the dissolved higher order polysulfides will migrate from the sulfur cathode to the Li metal anode through electrolyte, and then reduced chemically on the lithium metal surface.[41-45]

$(n-1)\,Li_2S_n + 2Li^+ + 2e^- \rightarrow nLi_2S_{n-1}$ Electrochemical Reduction

$(n-1)\,Li_2S_n + 2Li \rightarrow nLi_2S_{n-1}$ Chemical Reductios

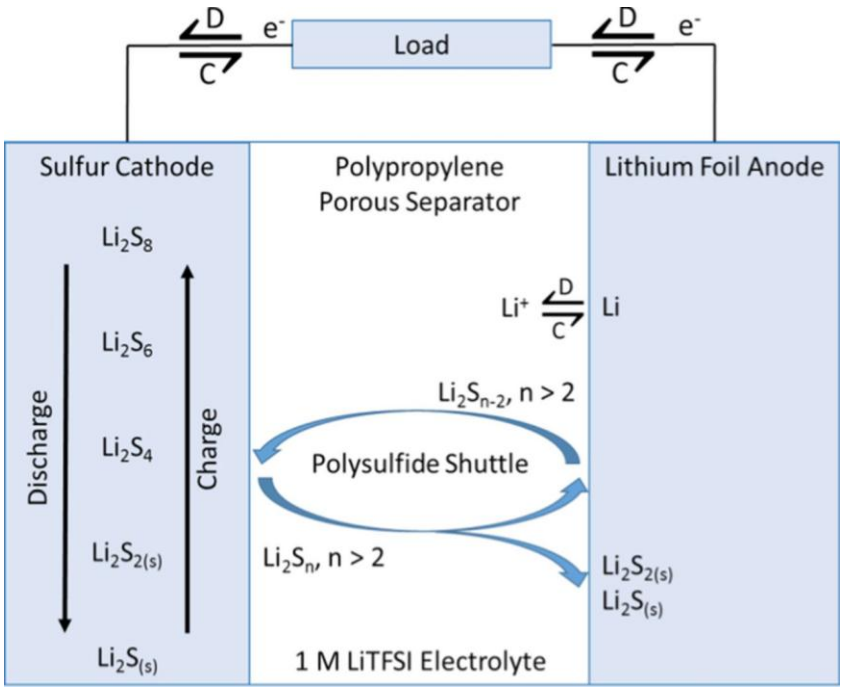

Figure 2.3 The shuttling mechanism in lithium sulfur batteries.

The above reduction reactions introduce an unavoidable self-discharge, rendering a significant fading of capacity and battery failure at last. The final reduced product, short-chain polysulfides, are no longer soluble and will form precipitate onto lithium metal surface, introducing an inevitable capacity decay over cycles.[46-47]

2.3.4 Non-soluble lithium sulfide and sulfur plating

The final reduced product, short-chain polysulfides (Li_2S and Li_2S_2), are no longer soluble and will form precipitate onto lithium metal surface, introducing an inevitable capacity decay over cycles due to the loss of active material.[48] Moreover, the insoluble polysulfides at cathode electrode will form a passivation layer on electrode surface and reduce the surface area, leading to a lower utilization rate. Also, the intrinsic electronic insulation will generate a larger charge transfer impedance.[49-51]

2.3.5 Lithium anode

The corrosion resulting from the parasitic reactions between lithium metal and soluble polysulfides is undesirable.[52] Also, the lithium metal can react with organic electrolyte molecules. Lithium can be consumed significantly by these reactions, with a passivation film formed onto its surface with large insulation for electrons and ions, which increases charge transfer impedance.[53] On the other hand, the passivation layer itself is considerably fragile and inhomogeneous, uneven lithium plating and stripping can easily break off the SEI film and introduce more harmful consumption of lithium, sulfur, and electrolyte.[52, 54]

2.3.6 Electrolyte

An ideal option of electrolyte for lithium sulfur batteries should possess such beneficial properties as: low reactivity with lithium metal anode, outstanding ionic conductively for lithium ions, poor polysulfide solubility, and wide electrochemical window in which electrolyte exhibits good chemical stability.[54] To the best of our knowledge, there is no organic electrolyte that can simply satisfy all these requirements. Consequently, various kinds of organic solvents and electrolyte additive with different ratios are utilized to optimize the battery performance. Conventionally, lithium salts such

as LiTFSI, $LiSO_3CF_3$, and $LiN(SO_2CF_3)_2$ are widely used for their proven chemical stability with dissolved polysulfides and good conductivity of lithium ions.[45, 55-57]

2.4 Research focus

As stated above, the majority of Li-S problems are related to the dissolution and diffusion of polysulfides in the electrolyte and following chemical and electrochemical reactions with lithium metal anodes. Therefore, to inhibit the dissolution and migration of polysulfides is important for battery performance and stability of lithium sulfur systems. Much of study has been conducted on developing novel cathode additives for the sulfur electrode. The enhancement methods include various structure of trapping polysulfides, bonding with sulfur species through chemical or physical adsorption.

2.4.1 Sulfur cathode

Since the design of lithium sulfur batteries was proposed three decades ago, it was noted that the insulating property of sulfur and the shuttling mechanism of its reduction products have been considered as major issues here. The solution to the issue of high cathode impedance is easy to be applied: an adequately effective electrical conductor needs to be incorporateded and well-dispersed in sulfur material to guarantee efficient electron transport between the cathode additive and the active material. About one decade ago, conductive carbons and conductive polymers were utilized as cathode additives to form (1) sulfur−carbon composites and (2) sulfur- polymer composites.[58-63] The conductive carbon was incorporated to sulfur-carbon composites to improve the electrical conductivity and utilization rate of the sulfur. For instance, the carbon black, which could serve as a good electrical conductor, is very frequently used for preparing the S-C mixture slurry. The active carbon should possess a high specific surface area and abundant micro/meso pores

to confine and adsorb the sulfur and polysulfides, which is important for suppressing polysulfide dissolution. On the other hand, the sulfur-polymer composites were initiated with the use of polyacrylonitrile (PAN) and showed a high initial discharge capacity of 850 mAh g^{-1}.[64] As a consequence, various types of conductive additives have been utilized into sulfur cathode in the past.

Among these cathode additives, porous carbon has attracted numerous attention because to its porous structure and higher electrical conductivity compared to that of conductive polymers, which are important properties for simultaneously satisfying the reactivity, adsorption and enhancing the cathode conductivity. Moreover, the engineered micro/meso porous carbon network not only promote retention of sulfur but also improve the electron and electrolyte transport in the electrodes. Thus far, different materials and synthesis methods have provided significant improvements in the battery performance of lithium sulfur cells.

2.4.2 Sulfur-carbon composite material

The innovative work were the sulfur−carbon composites designed by Wang et al, as Fig. 2.4 shows.[65] The utilized active carbon serves as an cathode additive for increasing the cathode conductivity and also impose strong confinement effect for the polysulfides in its micropores. This design enabled sulfur cathodes to show better cycling stability as a comparison to the pure sulfur electrodes. After study on sulfur-carbon composites, a sulfur−mesoporous carbon composite that showed a high discharge capacity and stable cycling performance was reported by Ji et al. in 2009.[66]

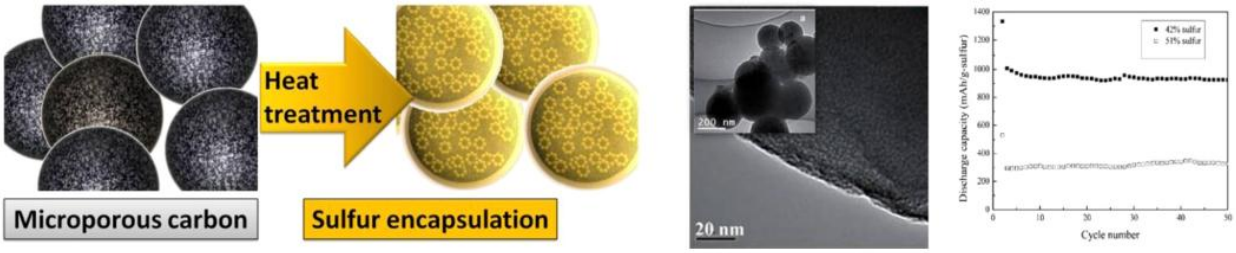

Figure 2.4 Schematic models, SEM observation, and cell performance of a representative S−microporous carbon composite.

A high specific capacity of 1320 mAh g^{-1}, with an utilization rate of 80%, and outstanding cycling stability were achieved by loading sulfur into a highly ordered mesoporous carbon (MPC).[67] The hierarchical MPC satisfies the requirement of providing pathways for efficient lithium ion transport within the carbon framework. The adequate contact among the electrons, sulfur, and organic electrolyte with the conductive network results in high utilization of sulfur. Moreover, the hierarchical spatial arrangement confines the sulfur within the network and inhibits the diffusion of polysulfides, resulting in a reversible cyclability. Based on this concept, numerous and various porous carbon networks have been developed. However, facile treatment usually introduces side effects as they solve the major shortcomings. Zhang et al. indicated the side effects related to the sulfur carbon composite cathode: good cycling performances are rooted in a very low sulfur to carbon ratio in the cathode.[68] The applicable sulfur content (65%) and active material loading (2 mg/cm^2) for the cathodes should be the bottomline for lithium sulfur battery development. On the other hand, several target-oriented researches show that the initial spatial arrangement of sulfur may not improve the capacity. It is resulted from that the originally elemental sulfur is reduced into soluble polysulfides during discharge, and then the polysulfides freely diffuse to anodes.[69-71] As a result, it is reasonable to consider that the morphology and state of the sulfur in the composite electrodes is determined by the

host and the interaction between them. So, it is imperative to look composites that is inpacting the cycling performance of the resultant cathodes. The porous carbons are subcategorized by their pore size and morphology. According to the pore size, the porous structure of these materials has been divided into three major types, and each type of porous carbon possesses distinctive advantages: (i) the micropore, with pore size smaller than 2 nm, has been demonstrated to be able to ideally confine the active material; (ii) the mesopore, with pore size between 2 nm and 50 nm, can improve sulfur impregnation and can improve lithium ion transport and electrolyte penetration; (iii) the macropore, with pore size larger than 50 nm, is usually resulted from an interconnected network of carbon nanotubes (CNTs) or carbon nanofibers (CNFs) which can inhibit polysulfide diffusion due to its good electrolyte absorbability.[69, 72-77] Moreover, CNT or CNF networks can be cooperated with various porous material to from composite porous structures via different synthesis methods, which could result in enhanced cycling performance.[78-80]

The effect of the porous structure on the battery stability was elucidated by the carbon sphere containing the sulfur material via a two-step heat treatment process. Zhang et al. developed the microporous carbon spheres to confine the active material and reactions inside their interior space by their strong adsorption.[81] As a consequence, the cathodes showed a cycle life for 500 cycles with the remaining capacity of 650 mAh g^{-1}.

The mesoporous carbon has been identified as an ordered sulfur encapsulation substrate. After systematically analyzing a series of mesoporous carbon materials with tunable pore sizes and pore volumes, Li et al. indicated that mesoporous carbon with a large pore size can introduce a higher sulfur loading and show good cell performance as Fig. 2.5 indicates, which improves the sulfur loading in current sulfur composite

cathodes.[67] On the other hand, under partial sulfur-filling conditions and surface modification, the encapsulated sulfur has an optimized electrical contact with the mesoporous substrate, which can limit the dissolution/diffusion of polysulfides and ensure a steady supply of lithium ions.

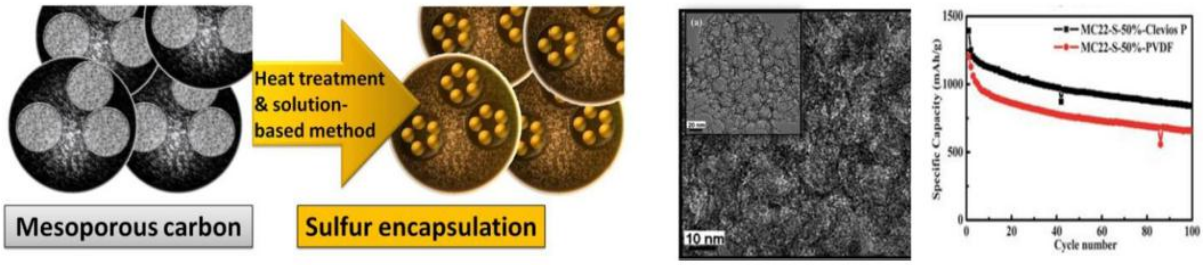

Figure 2.5 Schematic models, SEM observation, and cell performance of a representative S−mesoporous carbon composite.

Conventionally, carbon black is only used as a conductive additive in the cathode. However, the low cost and high electrical conductivity of carbon black offer advantages for sulfur cathodes. After carbon black is coated on the sulfur particle or sulfur is distributed in the carbon black clusters, the sulfur−carbon black composites can improve the sulfur utilization. The hollow carbon spheres, which are synthesized by a hard template route, possess a large interior void space with a diameter of 200−500 nm and a mesoporous shell with a thickness of 30−50 nm. Jayaprakash et al. reported porous hollow carbon−sulfur composites with excellent cycling performance: high capacity retention of 91% after 100 cycles. In the composite, the large interior void space of the porous hollow carbon allows the starting active sulfur and polysulfides to be stabilized within the conductive carbon sphere.[82] Furthermore, the mesoporous shell ensures a stable supply of lithium ions and electrolyte.

The CNTs function as an interwoven conductive network in the sulfur-based composites. In Han et al.'s work (Fig. 2.6[35]), a S−multiwall carbon nanotube composite cathode that has 20 wt % MWCNTs, 20 wt % conductive carbon, 50 wt % sulfur, and 10 wt % poly(vinylidene difluoride) (PVdF) manifested a higher discharge capacity and longer cycle life than the regular sulfur cathode containing 0 wt % MWCNTs, 40 wt % conductive carbon, 50 wt % sulfur, and 10 wt % PVdF.[83] This is because the MWCNTs have a high surface area for absorbing polysulfides and can form a three-dimensional (3D) conductive network structure to enhance electron transport. After combination of the advanced sulfur encapsulation technique with CNTs, several cycle-stable sulfur cathodes have demonstrated that the CNT network is a promising host material.

Figure 2.6 Schematic models, SEM observation, and cell performance of a representative S−CNT composite.

Guo et al. developed sulfur-impregnated disordered carbon nanotubes in a vacuum environment.[35] After sulfur vapor is infused into the narrow pore channel in a carbon shell, the carbon substrate can avoid severe polysulfide dissolution. It has been reported a self-weaving sulfur−MWCNT composite cathode having a coalescing MWCNT network as the electrical and ionic pathway for facilitating a fast charge/ discharge process. Moreover, the sulfur−MWCNT composite has good electrolyte absorption ability, which confines the soluble polysulfides within the electrode and avoids the irreversible loss of the active materials during cycling.

The CNFs have a nanosized shape similar to that of the nanotubes and, therefore, several morphological advantages similar to those of CNTs but without a hollow space in the middle.[84-85] The CNFs are also well-known for their good electrical conductivity and high structural strength. The high conductivity ensures the CNFs to be a suitable carbon conductor. Moreover, the CNF additives can form a network-like structure for suppressing the S/Li_2S agglomeration that normally coat on the sulfur cathode and inactivate the reactions. Rao et al. reported a nanocarbon/sulfur composite that has a CNF cluster as the 3D conductive network with nanoscale sulfur well dispersed in the CNF substrate, which enhances cathode conductivity and suppresses active material agglomeration.

Graphene is a novel 2-dimensional carbon monolayer is regarded as an ultra-light, thin, and hard material with high stability and conductivity. With these distictive and beneficial properties, graphene has been considered as excellent candidate material in many different industrial and academic fields. The flexible characteristics of graphene make it suitable to be the sulfur carrier in lithium sulfur batteries. The graphene in the composites coating or wrapping the sulfur can suppress the loss of active sulfur species due to dissolution during cycling.[84, 86-88]

2.4.3 Binder-free sulfur−carbon composite electrode

Binders, which are usually polymeric materials (e.g., poly- (tetrafluoroethylene) (PTFE) or PVdF), are widely used in conventional Li ion and other batteries in which they only act as a binding additive to hold the active material and carbon additives together without contributing any capacity. They are effective and interrupt the electrochemical processes in these batteries less prominently. However, in Li−S batteries, binders could play a critical role in the cell performance. As the structure and morphology change upon

cycling, binders cannot hold all the active materials, especially the soluble polysulfides. In addition, they could become "dead" sites for the electrochemical reactions between lithium and sulfur which can deteriorate the cell performance further. Therefore, functional or smart binders become more important in Li−S batteries than in Li ion batteries. In this section, binder-free sulfur electrodes are discussed. The binder-free electrode structure has shown unique advantages in some electrodes in Li ion batteries, such as Co_3O_4/graphene films, TiO_2 anodes, and silicon anodes.[89-95] Some of these materials, like sulfur, also undergo significant compositional and structural changes upon cycling in Li ion batteries. Without a binder, electrodes should be able to maintain the supportive and integrated structures while ensuring efficient electron and ion access to the active materials. Carbon is the most effective additive in electrodes to provide electron pathways. Carbon can also be fabricated into various morphologies, e.g., spheres, particles, fibers, tubes, etc., which makes binder-free sulfur−carbon composite electrodes possible. In addition, N-methyl-2-pyrrolidone (NMP) is a solvent generally used in fabricating Li ion battery electrodes to disperse the polymer binder and active materials. However, NMP is harmful to human health and the environment. Without a binder, such solvents can be eliminated, facilitating "green" fabrication processes with these binder-free electrodes. Moreover, the active material loading and electrode conductivity can also be increased without a binder. Elazari et al. have utilized microporous activated carbon fibers as a binder-free substrate to impregnate sulfur.[96] The carbon fiber cloth provides sufficient mechanical strength and electron conduction pathways. In addition, sulfur can diffuse into the voids (≤2 nm) in the carbon fibers. The sulfur content, however, is relatively low (ca. 33 wt %), which is due to the large dense fibers used. An accessible capacity of 1250 mAh g^{-1} hand a reversible

discharge capacity higher than 800 mAh g^{-1} after 80 cycles were obtained. The authors suggested that the maximum accessible capacity is limited by the electrochemical kinetics. Doarfler et al. utilized vertically aligned carbon nanotubes (VACNTs) grown on a metal foil as a substrate to hold sulfur with a high sulfur content of up to 70 wt %.[97] The VACNT was synthesized by a chemical vapor deposition process. The CNT films on the metal foil had a thickness of up to 100−200 μm and a density of about 0.06−0.13 g/cm^3. The calculated free volume in the CNT films was about 94 vol %, which can hold high sulfur loadings. In addition, CNTs have high electronic conductivity and a high retention of the integrity of the conductive network because of the high aspect ratio. These favorable properties led to a discharge capacity of over 1300 mAh g^{-1} (800 mAh g^{-1} based on the mass of the electrode) with the binder-free sulfur−CNT electrode. A similar approach was developed by Hagen et al., showing an even higher sulfur loading of 90 wt % with reasonable capacities and cyclability.[80] Zhou et al. used a sulfate-containing AAO template to directly grow aligned S−CNTs without metal substrates.[98] Sulfur contents of 23 and 50 wt % in S−CNTs have been demonstrated with discharge capacities of, respectively, 712 and 520 mAh g^{-1} over 100 cycles. Huang et al. modified the aligned S−CNT electrode by covering one end of the electrode with a PEG barrier to suppress the shuttle of polysulfides. The electrode with the PEG barrier showed a higher initial discharge capacity than that without the PEG barrier.[99] In addition, the electrode showed good cyclability with a capacity decay of 0.38% per cycle over 100 cycles without $LiNO_3$ in the electrolyte.

2.4.4 Sulfur−polymer composite material

Polymers are playing a more significant role than binders in Li−S batteries, especially functional polymers with favorable properties such as conductive polymers (e.g.,

polypyrrole, polyaniline, poly(3,4-(ethylenedioxy)thiophene) (PEDOT), etc.).[100-105] Since polymers can be synthesized by different methods and sulfur can be synthesized at low temperatures, a variety of sulfur−polymer hybrid materials have been developed with the target of reducing the dissolution and shuttle effect of polysulfides, improving electronic conductivity, and controlling the morphology of sulfur−polymer composite electrodes. A few strategies exploring polymers as a conductive matrix and/or barrier for blocking polysulfides are presented in the sections below.

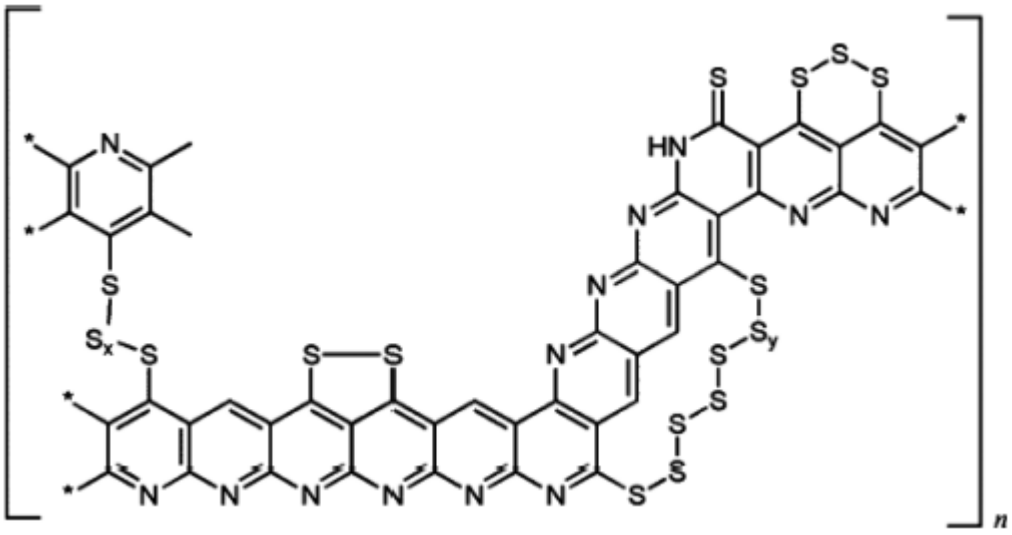

Figure 2.7 Proposed chemical structure of a sulfur−PAN composite.[105]

The first sulfur−conductive polymer hybrid material (Fig. 2.7) was developed by Wang et al.[105] They used elemental sulfur as a dehydrogenating reagent coheated with PAN at 280−300 ℃. The −CN groups in PAN form heterocycles, while the main chain of the polymer becomes like that of polyacetylene, which is a conductive polymer. The composite is in the form of nanoparticles with an average diameter of 200 nm. Extra sulfur (53.4 wt %) was stabilized in the composite, which is electrochemically active. However, the discharge voltage profile of the composite consists of a voltage slope at ca. 2.1−1.8 V without the

clear upper discharge voltage (2.3 V) and lower discharge voltage (2.1 V) plateaus that sulfur electrodes usually display. The composite material showed a capacity of 850 mAh g^{-1} in the first cycle, indicating almost all the sulfur was reduced to Li_2S. The cell showed decreasing cyclability with a remaining capacity of 600 mA h/g after 50 cycles in cells with a geltype polymer electrolyte. Yu et al. further characterized chemically and physically such sulfur−PAN composite materials, which were prepared at different temperatures, and examined their cycling performance. What they found was that the carbon matrix and sulfur react with each other, forming −C−S−S−C− bonds besides the dehydrogenation and cyclization of PAN when a mixture of sulfur and PAN are heated. The sample heated at 450 ℃ showed a stable capacity of 480 mAh g^{-1} over 240 cycles. Wang et al. synthesized sulfur−polypyrrole (PPy) composites first for Li−S batteries.[100] The composite was synthesized by a chemical polymerization method. Sulfur powder was dispersed in a solution of sodium p-toluenesulfonate as a dopant, 4- styrenesulfonic sodium salt as a surfactant, and pyrrole. $FeCl_3$ was used as an oxidant to polymerize pyrrole to form the S−PPy composite. The PPy particles were in the range of 200−500 nm, and the authors claimed that the sulfur particles were uniformly coated with the PPy nanoparticles. The discharge voltage profile showed the two typical plateaus of sulfur electrodes. The capacities of the S−PPy composite were higher than those of bare sulfur electrodes, which was attributed to the presence of PPy nanoparticles. Liang et al. and Sun et al. studied S−PPy composites with different morphologies, e.g., granular, tubular, and nanowire, in Li−S batteries.[106-107] Polyaniline (PANI) is another conductive polymer that has been widely used in making S−PANI composites. PANI can be used as either a conductive coating of sulfur materials or a conductive matrix after pyrolization. Wu et al. used an in

situ polymerization method to coat S−MWCNT composites with a layer of PANI.[108] The sulfur-coated MWCNT composite was prepared by ball-milling and thermal treatment. The initial discharge capacity was 1334.4 mAh g^{-1}, and the capacity was 932.4 mAh g^{-1} after 80 cycles. Similarly, Li et al. coated a S−C composite with a nanolayer of PANI via a two-step process.[109] The electrochemical performance of the composite was improved with high-rate performances, which was thought to be because of a cooperative effect of the conductive carbon black as conductor and the PANI coating to further enhance the conductivity in the sulfur cathode. A discharge capacity of 636 mAh g^{-1} was obtained at a rate of 10C, and the discharge capacity retention was above 60% over 200 cycles. Duan et al. introduced a layer-by-layer assembly technique to fabricate PANI-coated sulfur particles.[110] The positively charged poly-(allylamine hydrochloride) and negatively charged poly-(styrenesulfonate sodium salt) were first alternatively adsorbed onto the surface of sulfur particles, and then a layer of PANI was formed on the outer shell of the polymer-coated sulfur by an in-situ polymerization method. The composite was characterized, but no cell performance was presented.

2.4.5 Sulfur−metal oxide/nitride/chalcogenide composite material

Except for carbon and conductive polymers, other materials could be applied in the composite synthesis with sulfur. The additive should act as an absorbing agent for trapping the soluble polysulfides or may function as a supporting active material for generating extra capacity. To serve as the absorbing agent, the alternative material must have a redox potential not overlapping with that of sulfur (1.5− 2.8 V vs Li^+/Li) to prevent unwanted electrochemical reactions and structural change during cell cycling. The density and the amount of the alternative materials should not be too large; otherwise, the energy density

of the whole battery would deteriorate. To work as the secondary active material in a hybrid cathode, the alternative material must operate well under a voltage window similar to that of the primary active material, sulfur. The alternative materials should also have good compatibility toward the same electrolyte system as the primary sulfur active material.

From 2001, the application of vanadium oxides, silicates, aluminum oxides, and transition-metal chalcogenides has been proposed to sulfur cathodes for inhibiting the shuttling mechanism of polysulfides.[50, 111-115] However, the large particle size of these absorbing agents limits the absorbing ability, especially the electron transport properties, leading to limited improvement. Considering the size effect, Song et al. used nanoparticles of Mn-Ni oxide (30−50 nm) into S cathodes as polysulfide adsorbent, which led to outstanding battery performance with a capacity retention of 85% for 50 cycles.[116] It is seen that a suitable absorbing additive may possess the following properties: small size, porous structure to contain chemicals, and high surface area to enhance reaction kinetics. The representative metal oxides involve manganese nickel oxide, γ-alumina, silica, and titania.[112, 117-120] These nanosized additives have a polysulfide adsorbing effect for effectively addressing the polysulfide diffusion issue and thereby improving the cycle stability. Interestingly, such significant improvement wasb achieved by introducing a small amount of additive in cathode framework.

Tarascon et al. utilized the method of carbon coating $LiFePO_4$ to enhancing its conductivity, and introduced a design of carbon coating an effective host of the sulfur.[121] Their work utilized an insulating metal-organic framework (MIL-100) consisting of an open framework of small mesopores (~2.5-2.9 nm) and micropores (~0.5 and ~0.9 nm). Sulfur was incorporated through the melt diffusion method, forming a composite with 48

wt % sulfur. Because of the nearly insulating nature of MIL-100, 50 wt% of composite material needs to be with carbon intimate contact since the transfer of electrons should be guaranteed. Cui et al. proposed a novel nanosized design of sulfur cathode based on a yolk–shell architecture with sulfur contained within TiO_2.[122] It was proven that the hollow space of shell is capable considerably of accommodating the internal stress due to volume expansion and shrinkage of sulfur. An initial capacity of 1,030 mAh g^{-1} at 0.5 C and Coulombic efficiency of 98.4% over 1,000 cycles are achieved. Furthermore, the capacity indicated an average capacity degradation of 0.033% per cycle after 1000 cycles, demonstrating an outstanding battery stability for high performance lithium sulfur batteries over long cycles. Goodenough et al. [123] found that higher electrical conductivity and the capture of the soluble intermediate polysulfide by mesoporous TiN as a result of physical or chemical interaction lead to enhanced specific capacity and high rate of charge/discharge. Titanium nitride (TiN) has several exceptional properties for a ideal host of sulfur including: (1) low resistance, and (2) outstanding chemical and thermal stability. In their paper, it firstly reported that the use of a mesoporous TiN as a framework to form a sulfur cathode that performs much better than solely either mesoporous TiO_2-S or Vulcan C-S. After 500 cycles at a C-rate of 0.5C, the TiN-S composite cathode indicated a specific capacity of over 644 mAh g^{-1} with a capacity decay of 34.8%.

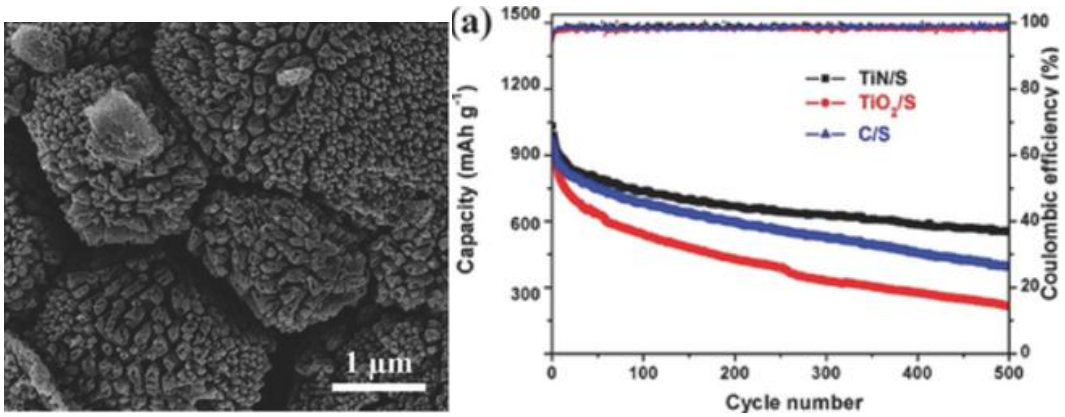

Figure 2.8 SEM images of mesoporous TiN and Cycling performance of TiN-S, TiO_2-S, and Vulcan C-S over 500 cycles at a charge/discharge rate of 0.5 C rate.[123]

2.4.6 The passivation of Li metal anode

Protection of lithium metal anodes plays an important role in all lithium metal batteries. In the electrolyte environment rich of polysulfides, the formation of passivation layer becomes more complicated due to the chemical and electrochemical reactions between polysulfides and lithium metal other than reactions between lithium and electrolyte as well as additives only. To fully achieve the stable, smooth and stable passivation layer on lithium metal anode, such standard should be met: (1) It needs to remain insoluble in liquid electrolyte; (2) It needs to be chemically inert to lithium metal, organic electrolyte, and polysulfides; (3) It should allow lithium ion flow through freely.

Gel polymer electrolyte indicates a strong capability of adhering the lithium anode and polymer separator in batteries, which could suppress the lithium plating. Mikhaylik et al. utilized an electrolyte layer between lithium metal and polymer separator to testify its effect on retaining capacity and mitigation of thermal runaway because of lithium dendrite extrusion.[124] An in-situ polymerization procedure promotes the formation of a crosslinked polymer layer, leading to a smoother morphology on lithium metal anodes.

Alloying of lithium metal could introduce a mechanical strong and structurally dense passivation film. Zheng et al.[125] used sputtering method to coating a layer of platinum onto lithium metal, resulting in an alloyed film consisting of lithium and platinum. This alloy film demonstrates a high capability of complexed with polysulfides, greatly improving the battery performance and enhancing its retention rate after cycles.

Pre-passivation of lithium metal surface is considered as one of the effective methods of protecting the lithium metal over cycles. Ma et al.[53] introduced a pre-passivated lithium anode by directly reacting lithium metal with nitrogen gas to form a polycrystalline layer of Li_3N. This layer not only efficiently blocks the reaction among lithium metal, organic solvent and polysulfides, but also indicates a strong ability of inhibiting the dendritic growth of lithium, thus resulting in an improved capacity retention and battery stability. The utilization of electrolyte additive is regarded as the most common and practical method of imposing an effectively protective passivation layer. The passivation layer could be in-situ formed, requiring no extra treatment. Lithium nitrate and similar compounds are considerable useful in suppressing the polysulfide shuttling mechanism. With detailed surface analysis, the product between $LiNO_3$ and lithium metal could assist to form a favorable passivation layer on lithium surface with its desirable properties.[57, 126]

3 CHAPTER 3 STRUCTURED TITANIUM NITRIDE NANOTUBE ARRAYS/SULFUR COMPOSITE AS NOVEL CATHODE MATERIALS FOR ADVANCED LITHIUM SULFUR BATTERIES*

3.1 Introduction

There is an increasing demand for energy storage devices with high energy and power density for electric vehicle/hybrid electric vehicle (EV/HEV) and other industrial applications. The increase in consumption of fossil energy has provoked significant concern about environmental pollution.[127-129] In order to overcome these limitations, there is an urgent need of developing reliable, stable and green power energy storage devices to further reduce the possible negative effects of fossil fuel. Consequently, there is extensive research on the conversion, storage and application of electrochemical energy from scientists and engineers of academics and industry.[19, 130]

Lithium sulfur batteries have long been considered one of the most promising electrochemical systems due to its outstanding specific capacity of up to 1675 mAh g^{-1}, which is based on the sulfur element in solid cathode materials.[22] This almost five-fold increase of specific capacity, compared to the conventional lithium ion batteries, indicates the potential of this electrochemical system for EV applications.[131-133] Despite the considerable advantages of Li-S batteries, the industrial application of these batteries has been greatly hindered by several intrinsic drawbacks.[31, 134-135] Due to the insulating nature of sulfur and inevitable polysulfide diffusion through electrolytes, the low utilization rate of active material becomes a formidable challenge when it comes to actual commercialization. Extensive research has been focused on mitigating these limitations, by mainly introducing a stable, conductive and flexible framework to host sulfur.[136-138]

Also, efforts have been aimed to improve Li–S battery performance by stabilizing the lithium anode, exploring new electrolytes, and the use of selective membrane between electrode and separator.[139-140]

The recent interests in developing novel sulfur cathodes leads to an extensive enhancement to the Li–S battery technology. A set of strategies has been proposed to improve the electrochemical properties (including specific capacity, rate capability, Coulombic efficiency, and cycling stability) with the facilitation of different cathode materials. The materials studied include nanostructured carbons (e.g., porous carbon with various pore size, carbon nanotube, carbon nano-fiber, graphene, etc.), functional polymers that acts as conductive matrix (e.g., polyaniline, polypyrrole, polythiophene, poly(3,4-ethylenedioxythiophene), etc.), and metal oxide/nitride/chalcogenide.[75, 131, 133, 135, 137, 141-145] Attempts have also been made to improve electronic conductivity and to limit polysulfide dissolution from the cathode. Nanostructured materials, in general, may improve overall electron transfer, provide more electrochemical active sites, and alleviate mechanical fracture during cycles.[126, 146-148] However, the dimension effects of nanostructured materials on battery stability and performance have not been fully elucidated. Goodenough et al.[123] introduced mesoporous TiN as a matrix hosting sulfur in lithium sulfur battery to improve its performance, resulting in a specific capacity of 644 mAh g^{-1} after 500 cycles at a current rate of 0.5 C. Moreover, TiN nanoparticles/sulfur composites were investigated as cathode materials in lithium sulfur batteries by Mosavati et al[28] and Hao et al.[149] Specific capacities of 1100 mAh g^{-1} and 660 mAh g^{-1} were obtained after 100 cycles at 0.1 C[28] and 200 cycles at 0.5 C,[149] respectively. Since titanium nitride (TiN) has a number of desirable properties as a potential host material of sulfur, including: (1) high electrical conductivity

(better than titanium metal and carbon), and (2) excellent chemical stability owing to the formation of an oxide passivation layer; this metal nitride has been studied as conductive matrix to host S within the cathode architectures.[28, 150-151]

Herein, the dimensional effects on electrochemical performance of a highly structured TiN as host material are investigated. The 3D highly structured nanotubes of TiO2 grew vertically onto the surface of the conductive Ti foil, which can be converted to TiN nanotube after nitridation with NH3. The correlation between TiN nanotube length and diameter, BET surface area, morphology, active sulfur composition, and their electrochemical performance was studied. Results indicated TiN nanotubes with longer length and smaller diameter were found to exhibit the best performance among all as-synthesized nanostructures, and were also better than other reported nanostructured additives/sulfur compounds for lithium sulfur batteries.[34, 152] Overall, the matrix, composed of titanium nitride nanotubes, shows an enhanced capability of limiting the diffusion of soluble polysulfide, decreasing the charge transfer impedance, and maintaining a good capacity over long cycles.

3.2 Experimental

3.2.1 Preparation of titanium nitride nanotubes

In order to synthesize titanium nitride in the form of nanotube arrays, a two electrodes setup was used to first prepare highly-ordered TiO_2 nanotubes arrays by a two steps anodization method.[153-154] This set up has a Ti working electrode (titanium foil, 99.6 % purity, 1.0 mm thickness, GoodFellow) and a Pt counter electrode. To obtain TiO_2 nanotubes with different diameters and lengths, Ti foil were anodized under different anodization voltage and time, in an ethylene glycol (EG, 99.8% anhydrous, Sigma-Aldrich)

solution containing 0.5 wt% NH_4F and 2 vol% deionized water.[153] Subsequently, the TiO_2 aggregated layer was peeled off using ultrasonication for 10 min. Then, the second anodization step was started with the same solution and under the varying voltages and desired time duration. The resultant TiO_2 nanotubes and Ti substrate were calcined under ammonia in a tubular furnace. The powder was first loaded into a zirconia boat and placed in a tubular reactor, which was connected to the gas feed system. Initially, the reactor was purged using 150 mL min^{-1} Argon (Ar) gas for 1h; followed by 200 mL/min pure NH_3 gas for 30 min to stabilize the gas flow. The reactor was then heated to 250 ℃ in 8 h, held for 40 min, then raised to 800 ℃ over 3 h and maintained for 1 h. The furnace cooled down to room temperature followed by flowing 150 mL min^{-1} Ar gas overnight.

To synthesize titanium nitride nanotubes with different lengths and diameters, the corresponding anodization voltage and time need to be properly chosen and optimized. After 10 hours, 6 hours and 10 minutes of anodization, the lengths of 30 μm, 15 μm and 4.5 μm are obtained, respectively. Also, with anodization voltage of 75 V, 60 V and 45 V, different diameters, 100 nm, 65 nm and 35 nm, of titanium nitride nanotubes are synthesized, respectively. Tube length of longer than 30 μm is not possible since nanotubes would peel off from the substrate. On the other hand, smaller nanotube diameter (< 35 nm) cannot be synthesized using a lower anodization voltage.

3.2.2 Fabrication of electrodes and cell assembly

After the desired titanium nitride nanotubes have been synthesized, the electrode slurry was prepared by firstly incorporating sulfur with conductive additive (nanostructured titanium nitride or Super P carbon black) with a wt. ratio of 7:3 by melt-diffusion method. The mixture was first heat above the melting temperature of sulfur

around 115 °C and maintained for 30 minutes. 10 wt% of poly(acrylonitrile-methyl methacrylate) AN/MMA (94:6, Polysciences Inc) was added as binder and N-methyl pyrrolidinone (NMP) as solvent to the slurry. The slurry was then coated on Al foil and dried at 80 °C under vacuum for 10 h.

1,3-Dioxalane, 1,2-Dimethoxyethane, LiTFSI, $LiNO_3$ were purchased from Aldrich and used as received. An electrolyte with 1 M of 1,3-Dioxalane, 1 M of 1,2-Dimethoxyethane, 1 M LiTFSI, and 2 wt% $LiNO_3$ was prepared by stirring at 80 ℃ for 6 h. 8 μL of electrolyte solution was added onto TiN cathode. In addition, a Polypropylene separator (Celgard 2400), and lithium foil anode were used to assemble coin cells (CR2032) inside an argon filled glove box.

3.2.3 Materials characterization

Phase purity and crystal structure of electrode materials were characterized using a Rigaku Miniflex 600 X-Ray Diffractometer. Morphological features of the TiN nanotubes were observed with scanning electron microscopy (TESCAN). The specific surface areas and pore size of the electrode materials were measured by Braunauer-Emmet-Teller (BET) multimolecular adsorption method (Accelerated Surface Area and Porosimetry System (ASAP) 2020 Plus). For characterizing the weight ratio of the sulfur composite, a thermogravimetric analysis (TGA, Q500 model from TA instruments) was performed on the composite in a temperature range of 30 – 700 ℃ with a heating rate of 5 ℃ min^{-1} under a nitrogen gas atmosphere.

3.2.4 Electrochemical measurements

Galvanostatic discharge-charge tests were conducted using a Maccor Model 4200 Automated Test System between the voltage range of 1.6 to 3 V (vs. Li/Li+) at room

temperature. Electrochemical Impedance Spectroscopy (EIS) experiments were performed using a Gamry potentiostat reference 3000. The minimum amplitude of AC voltage was 0.1 mV. The frequency was swept from 0.1 Hz to 100 kHz.

3.3 Results and Discussion

TiO_2 nanotube arrays were formed from Ti foil in the EG solution as described previously. The formation mechanisms can be attributed to the result of two separate competitive procedure: anodization and chemical dissolution. As the anodization of Ti foil starts, O^{2-} anions generates from the dissociation of the trace amount of water, and the formation of a layer of compact anodic oxide can be observed.[153, 155] These reactions are described as below:

$$H_2O \rightarrow H^+ + OH^- \quad (1)$$

$$2\ OH^- \rightarrow O^{2-} + H_2O \quad (2)$$

$$Ti + 2\ O^{2-} - 4e^- \rightarrow TiO_2 \quad (3)$$

When the dense TiO_2 layer thickens to a certain value, O^{2-} migrates inside of the dense oxide layer, a portion of anions will lose electrons resulting in oxygen gas.[156] Also, chemical dissolution of oxide layer to soluble fluoride compound[153-154, 156-157] happens both at the surface and inside layers.

$$TiO_2 + 6F^- + 4H^+ \rightarrow [TiF6]^{2-} + 2H_2O \quad (4)$$

The SEM images (Fig. 1a, b, c) are recorded at micron level and shows TiN nanotube structures with diameter of about 65 nm and length of 4.5, 15, and 30 μm, respectively. These nanostructures tend to be vertically oriented on the surface of Ti foils, forming a

nanotube array structure. The TiN nanotubes show a scraggly surface as a result of the lattice shrinkage, which can be attributed to the structure transformation from TiO_2 to TiN.

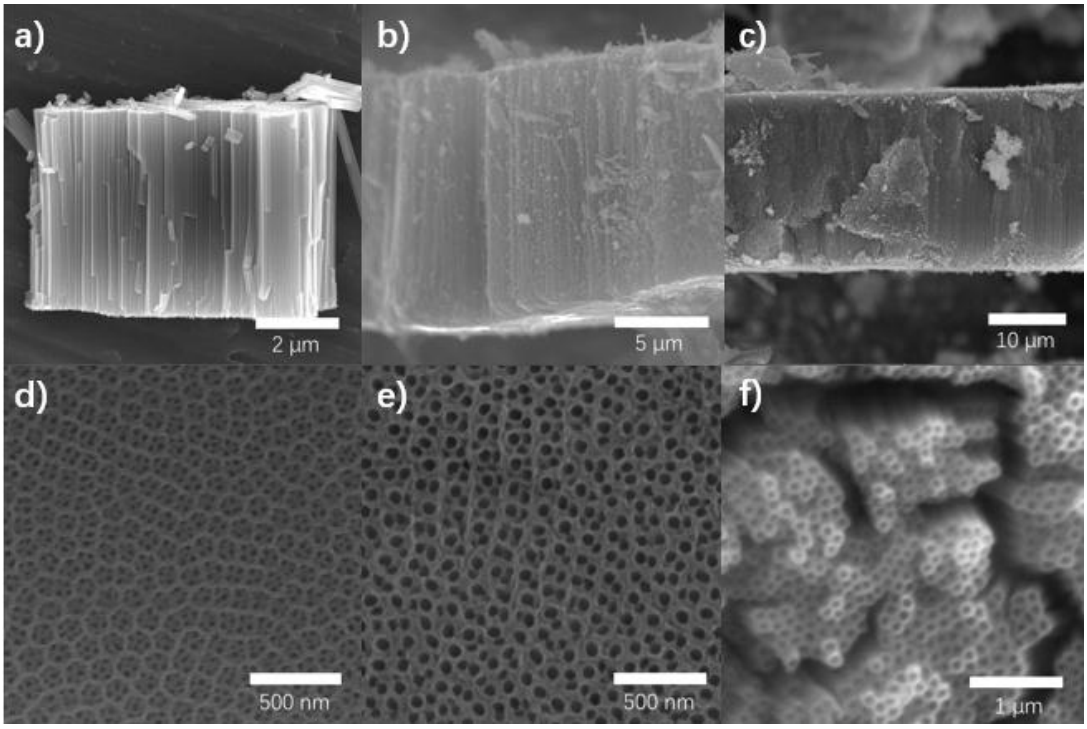

Figure 3.1 SEM images of TiN nanotube of diameter of 65 nm and (a) 4.5 µm, (b) 15 µm and (c) 30 µm in its length from side view, and nanotube of length of 4.5 µm and (d) 35 nm, (e) 65 nm and (f) 100 nm in its diameter from top view.

In order to further investigate the effect of TiN nanotube diameter on capacity performance and cycling stability of Li-S battery, TiN nanostructures of different diameters, by applying various anodization voltage, were prepared on Ti foil. Fig. 1d, e and f shows the SEM images of TiN nanotubes with a 4.5 µm length and different diameter of 35, 65, and 100 nm, respectively. It is known that one of the factors determining electrocatalytic activity is the accessible surface area. Therefore, with different nanotube diameters, this ultrafine nanotube 3D structure could provide an even larger specific surface to volume ratio which could promote electroactivity on the surface. These 3D structures will allow effective migration of the electrolyte and thus enhance mass/charge transfer at the electrode/electrolyte interface.[158]

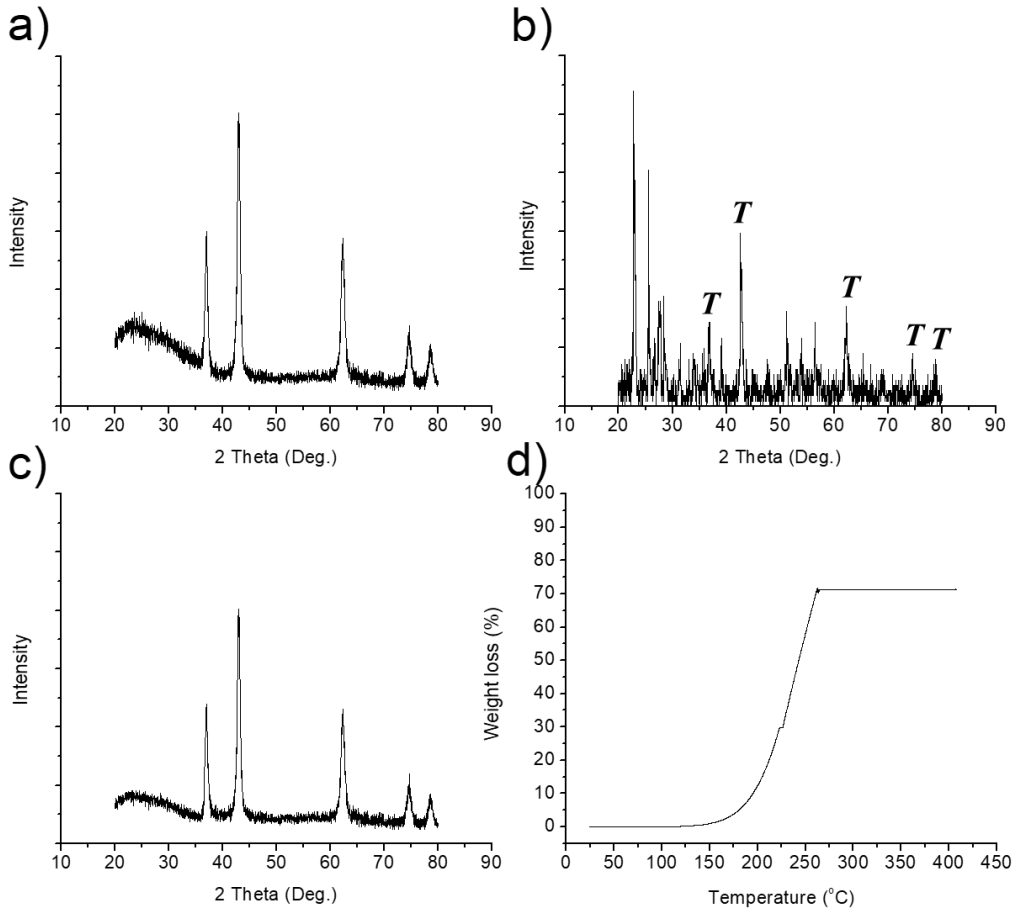

Figure 3.2 XRD spectra of (a) TiN nanotube, (b) the mixture of TiN nanotube and sulfur with typical peaks of TiN indicated, and (c) the composite after melt-diffusion process. (d) TGA analysis of sulfur loading.

Fig. 2a shows the X-ray diffraction (XRD) spectra of the prepared TiN with five diffraction peaks corresponding to the TiN (111), (200), (220), (311) and (222) crystal planes. The positions and intensities of TiN diffraction peaks can be indexed to the face-centered cubic structure of TiN (JCPDS file no. 38-1420) with a lattice constant a = 0.424 nm. After mixing sulfur with TiN nanotubes, XRD spectra indicate both typical peaks from titanium nitride and sulfur (Fig. 2b), indicating the chemical composition of the mixture. After heating this mixture above the melting temperature of sulfur and maintained for 3 hours, XRD spectra (Fig. 2c) exhibit almost no sulfur peaks, suggesting sulfur becomes amorphous after melt-diffusion procedure.[159-160] Thermal gravimetric analysis (TGA) were

conducted with a TGA/DSC (Q500 instrument) in argon at a scan rate of 10 ℃ min^{-1} from room temperature to 400 ℃.[161] As evidenced by TGA result (Fig. 2d), the sulfur loading in the TiN nanotube materials was to be 71.2 wt%. The corresponding areal sulfur loading is 8.7 mg cm^{-2}.

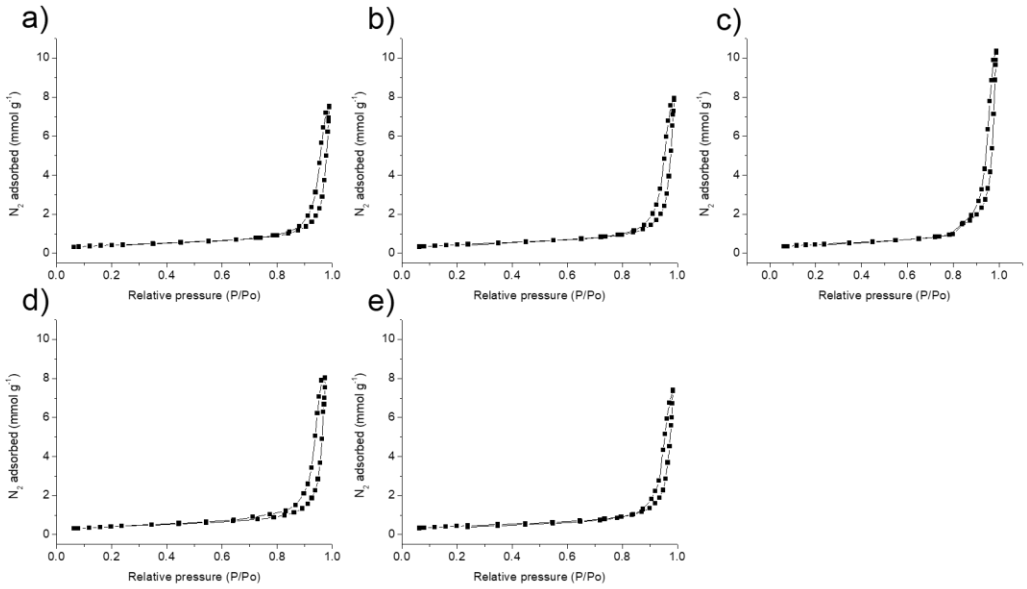

Figure 3.3 N_2 adsorption/desorption isotherms of TiN nanotube with dimension of (a) 4.5 μm and 65 nm, (b) 15 μm and 65 nm, (c) 30 μm and 65 nm, (d) 4.5 μm and 35 nm and (e) 4.5 μm and 100 nm.

Nanotube length (μm)	***4.5***	***15***	***30***	***4.5***	***4.5***	***4.5***
Nanotube diameter (nm)	***65***	***65***	***65***	***35***	***65***	***100***
BET surface area (m^2 g^{-1})	***34.14***	***33.97***	***35.32***	***45.15***	***34.14***	***21.76***

Table 3.1 The BET surface areas derived from nitrogen isotherm, of TiN nanotube structure with varying size.

Fig. 3 shows the N_2 sorption isotherms of TiN nanotube with different size dimensions. All nanostructures exhibit a type IV isotherm according to IUPAC and indicated the existence of a pore size range from mesopores to macropores.[162] In Fig. 3a, b and c, the N_2

sorption isotherms of nanotube structures with a diameter of 65 nm and varying length from 4.5 μm, 15 μm and 30 μm are shown. At relative pressure of above 0.1, the samples show almost no increment in N_2 adsorption capacity, which shows that the limited amount of mesopores.[32, 61] While, the final increased tails in the curves at a relative pressure from 0.9 to 1.0 suggest the increment of macroporosity.[61] As expected, there is no an obvious change in BET surface area (34 m^2 g^{-1}) as a function of nanotube length, as shown in Table 1. From Fig. 3a, d and f, the N_2 sorption isotherms are demonstrated for 4.5 μm long nanotube structures with diameters of 65, 35 and 100 nm, respectively. The larger hysteresis between adsorption and desorption branches within the range of relative pressure from 0.7 to 0.9 in Fig. 3d indicates the appearance of mesopores.[163] Moreover, the increasing narrowness of the hysteresis loops, with a decreasing diameter, with steep and nearly parallel adsorption and desorption branches suggests a decrease of pore size and surface area.[163-164] The specific surface areas of these samples are 45.15, 34.14 and 21.76 m^2 g^{-1} for 35, 65 and 100 nm, respectively (Table 1). The smaller diameter nanotube arrays lead to an increasing surface area, which could in turn provide more electro-chemical active sites to enhance chemical reactions and mass transport. Also, the structure with more confined space will become a more effective host for soluble lithium polysulfides in charging and discharging cycles.[61, 162]

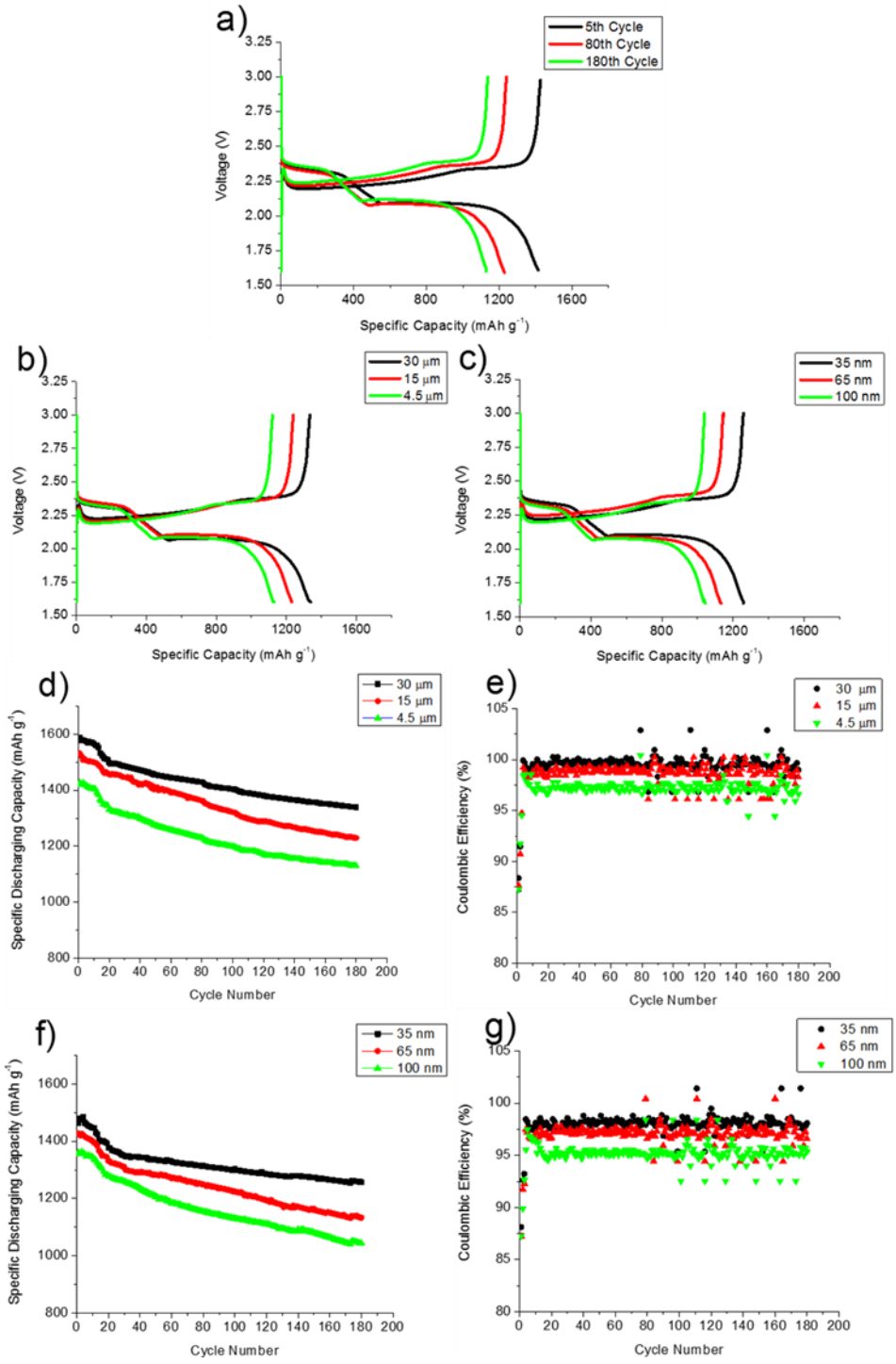

Figure 3.4 Galvanostatic charge-discharge voltage profiles of cells with TiN nanotubes and cycling performance of the sulfur–TiN nanotube composites.

Fig. 4a shows the galvanostatic charge-discharge voltage profiles of the S/TiN cell for different cycles (TiN nanotubes of length as 4.5 μm and diameter as 65 nm). Voltage-

capacity curves demonstrate two typical discharge plateaus located at 2.35 V and 2.05 V, and one charge plateau at 2.35 V, which are consistent with previous results.[28, 149] Fig. 4b and c shows the voltage-capacity curves of TiN nanotube diameter of 65 nm and lengths of 4.5, 15, and 30 μm, and TiN nanotube length of 4.5 μm and diameters of 35, 65, and 100 nm, at 180th cycles, respectively. These results indicate that the better capacity retentions are observed with longer length and smaller diameter TiN nanotubes. Fig. 4d shows the cycling performance of the titanium nitride nanotubes with lengths of 4.5, 15, and 30 μm and diameter of 65 nm cycled at a rate of 0.1C for 180 cycles. The discharge capacity of 180^{th} cycle at 0.1C is remained as 1338 mAh g^{-1} for the cell with longest length of 30 μm, compared to the 1229 and 1128 mAh g^{-1} for nanotube length of 15 μm and 4.5 μm, respectively. Capacity decays of 0.064%, 0.086% and 0.097% per cycle are observed for 30 μm, 15 μm and 4.5 μm TiN nanotubes, respectively. This finding suggests longer TiN nanotubes will provide a more stable sulfur host matrix leading to lower capacity decay. The charge/discharge capacity with TiN nanotube of diameters of 35, 65, and 100 nm, and length of 4.5 μm is shown in Fig. 4f. The first cycle charge/discharge capacity of almost 1480 mAh g^{-1} sulfur was observed with smallest nanotube diameter, indicating nanotubes with higher surface area provide better performance. In general, the capacity fades monotonically, probably due to partial dissolution of the polysulfides and escaping from the nanotube pores. However, even after 180 cycles a reversible discharge capacity of 1338 mAh g^{-1} sulfur could be obtained as the best result. Thus, the remarkable cycling stability and specific capacity of this electrode can be attributed to the stable electrodeposited active materials hosted by the TiN nanostructure. These nanotube materials all show a coulombic efficiency above 96% after initial cycles, indicate good reversibility of the electrochemical

reactions (Fig. 4e and g). Furthermore, a good capacity retention with high columbic efficiency is found as a result of good utilization of the active mass and minimizing the Li-polysulfide shuttle mechanism. These results suggested the coulombic efficiency was improved with longer length and smaller diameter of TiN. This could be attributed to the fact that more polysulfide has been inhibited from migrating through electrolyte thus minimize shuttling reaction and self-discharge. This process will also minimize undesired formation of insulating layer onto anode surface, as well as loss of active materials.[149] Thus, one of the most severe issues of lithium-sulfur batteries, i.e. cyclability, has been mitigated.[146, 165]

Fig. 5a shows the rate capability study of the TiN nanotubes with lengths of 4.5, 15, and 30 μm and diameter of 65 nm. With the increase in the current rate from 0.1 C to 1 C, the sample with TiN nanotube performs better than sulfur cathode with carbon material, usually lower than 700 mAh g^{-1} at 1 C.[34, 75, 141] At a current rate of 1 C, the sample with longest nanotube length delivers a capacity of 820 mAh g^{-1}, a remarkable result for a sulfur cathode at this high rate.[18, 75, 146] Moreover, the discharge capacity can be mostly recovered when the current density is decreased again from 1 C to 0.1 C, suggesting good abuse tolerance of the TiN nanotube under different current densities.

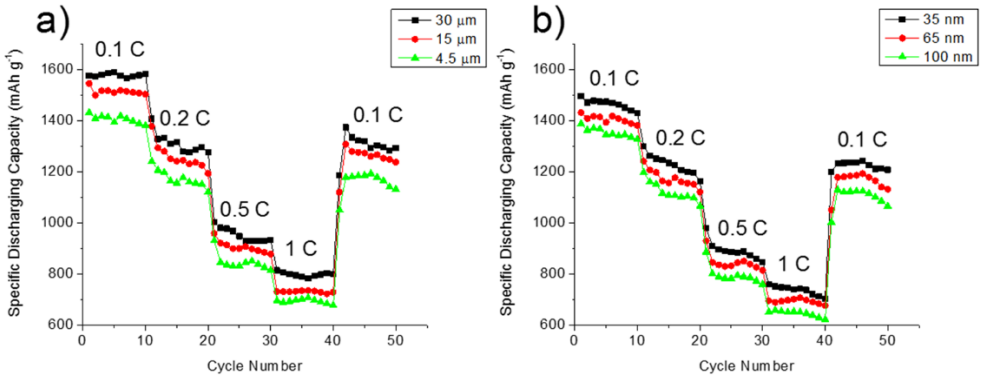

Figure 3.5 Cycling behavior of TiN/S cathode materials at different discharge rates with (a) lengths of 4.5, 15, and 30 μm and diameter of 65 nm and (b) diameters of 35, 65, and 100 nm and length of 4.5 μm.

The rate capability of different TiN electrodes with 35, 65, and 100 nm diameter and 4.5 μm length were investigated (Fig. 5b). It is known that one of the factors determining electrocatalytic activity is the accessible surface area. As expected, the electrode of 35 nm diameter TiN nanotube with higher surface area displays a higher discharge capacity of 1450 mAh g^{-1} after 180 cycles, contrasting with the 1390 and 1340 mAh g^{-1} discharge capacity of the 65 nm and 100 nm electrodes, respectively. With the current rate gradually increases to larger current 1 C, these electrodes display the corresponding discharge capacity of 780, 720 and 650 mAh g^{-1} in Fig. 5.

EIS measurements before and after the rate capability cycles (Fig. 6a and b) also suggest that the charge transfer resistance increased almost 13 Ω for the cell with Super P carbon black. As a comparison, only 5%, 13.0% and 14.8% increase in charge transfer resistance were observed for the cells with TiN nanotubes of 65 nm in diameter and 30, 15, and 4.5 μm in length, respectively (Table 2). The difference between the two materials can be attributed to the high conductivity, as well as chemical and thermal stability of titanium nitride.[28, 123, 149] Furthermore, it has been confirmed that by introducing longer TiN nanotubes, the initial value and increasing value of charge transfer resistance have decreased.

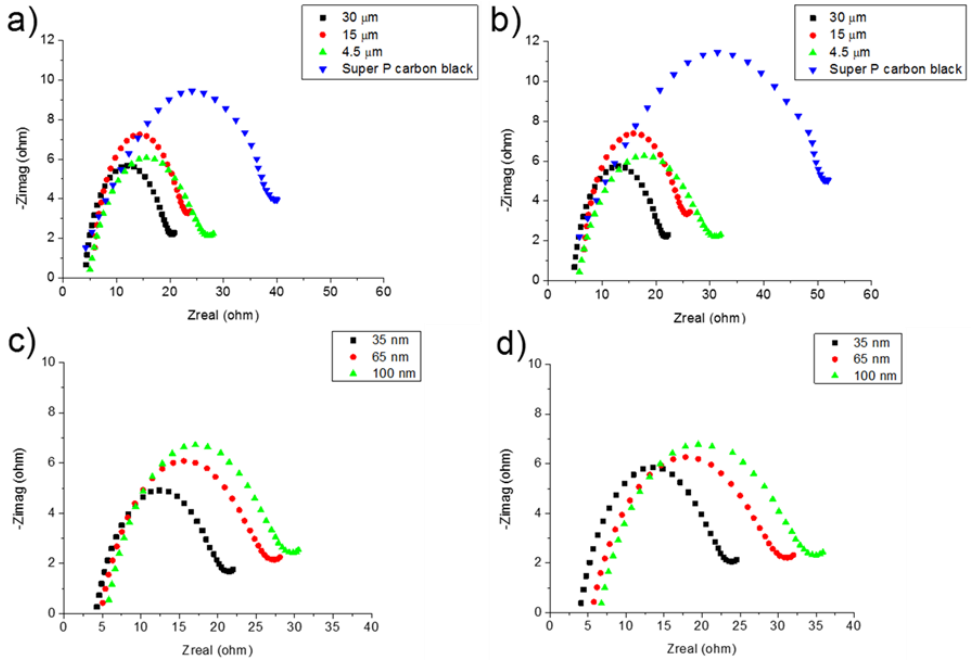

Figure 3.6 EIS spectra of Super P carbon black and TiN/S cathode materials for lengths of 4.5, 15, and 30 µm and diameter of 65 nm (a) before and (b) after 50 cycles; as well as (c) before and (d) after 50 cycles for diameters of 35, 65, and 100 nm.

Materials	***TiN***						***Super P carbon black***
Length (µm)	***30***	***15***	***4.5***	***4.5***	***4.5***	***4.5***	***N/A***
Diameter (nm)	***65***	***65***	***65***	***35***	***65***	***100***	***N/A***
Initial resistance (ohm)	***20***	***23***	***27***	***21***	***27***	***29***	***39***
Resistance after 50 cycles (ohm)	***21***	***26***	***31***	***24***	***31***	***35***	***52***
Resistance increase (ohm)	***1***	***3***	***4***	***3***	***4***	***6***	***13***
Resistance increase (%)	***5.0***	***13.0***	***14.8***	***14.2***	***14.8***	***20.6***	***33.3***

Table 3.2 The initial and after 50 cycles charge transfer resistance, derived from EIS spectra, of Super P carbon black and TiN nanotube structure with varying length and diameter.

The effect of titanium nitride nanotube diameter on the electrochemical performance has been tested with the EIS measurement (Fig. 6c and d). It is observed that with

increasing diameter of TiN nanotubes, the initial charge transfer resistance is increased. Also, 14.3%, 18% and 21% increase in charge transfer resistance after rate capability cycles were observed for nanotubes with length of 4.5 μm and diameters of 35, 65, and 100 nm, respectively (Table 2). The lower resistance of the smallest diameter could result from improvement of the current collecting capability of cathodes due to higher surface area of active material host, as well as the spatial confinement to insulating sulfur and precipitated polysulfide molecules.[144, 162]

Goodenough et al. [123] found that higher electrical conductivity and the capture of the soluble intermediate polysulfide by mesoporous TiN as a result of physical or chemical interaction lead to enhanced specific capacity and high rate of charge/discharge. However, the issue of capacity fading, though much alleviated, still needs to be addressed. Also, carbon nanotube materials were found to have a significant improvement compared to other porous carbon matrix[35, 166-167]. Since the sulfur confined in void space of mesoporous structure is still accessible to electrolyte in which polysulfides are dissolved, thus, minimize the effectiveness of the material to retain polysulfides. Therefore, poor capacity retention and rapid decay is still being observed for mesoporous structure. Furthermore, the size effect of nanostructure has been investigated on mechanical and electrical properties, chemical kinetics and battery performance.[168-172] It has been shown that nanostructure with a smaller pore size could exhibit better electrochemical performance, which is attributed to higher specific surface area allowing the charge process to occur more easily and more reversibly.[170] Also, the significant effect of length, diameter, wall thickness and aggregate size have been demonstrated on physical and electrochemical properties of composite with nanotubes.[168, 173]

The high specific capacity and good cycling stability of structured titanium nitride nanotube/sulfur composite suggested TiN is a promising material for future lithium sulfur batteries with high energy density. It is worth noting that the titanium nitride with smaller diameter and longer tube structure exhibits higher energy density and better cyclability than reported in literature.[123, 149]

Firstly, smaller diameter of nanotube structure increases the accessible surface area to enhance electro-catalytic activities. The active material, sulfur, is effectively confined in the titanium nitride nanostructure, the contact is improved owing to the relatively smaller diameter (~35 nm) of the nanotubes compared to larger diameters, and hence the reaction kinetics are also enhanced.[145, 170] Also, more uniform distribution of sulfur material separated by nanostructure of smaller size may minimize internal stress. Thus, the loss of electrical contact within electrode due to mechanical failure, such as cracking and bulky delamination will be alleviated.[35, 66]

Secondly, the titanium nitride here acts as the host of active material sulfur. The nanotube structured titanium nitride with longer length performs better as a sulfur "trap". Moreover, the nanotube of absorptive titanium nitride may minimize the egress of bulky polysulfide molecules out of the confinement of nanostructures into the electrolyte. Thus, nanotubes with larger length provide more physical barrier to further trap the highly polar polysulfide species.[31, 35, 166] In addition, Yuan et al.[174] and Cheng et al.[175] found that there is an increase in the amount of bulky sulfur particles attachment and entrapment of polysulfide in nanotube structures with well-preserved length. As a result, the batteries have a better stability and electrochemical performance. In addition, since sulfur itself is insulating as indicated previously, the matrix constructed of titanium nitride provides a

more conductive pathway for electron transfer.[66, 145, 162] Moreover, similar findings have been observed for longer hierarchical carbon nanotubes as additives.[166, 174] Therefore, the enhanced electrochemical behavior of longer TiN nanotube can be attributed to a more conductive matrix that promote the efficiency of electron transfer to the sulfur mass and accessibility to the Li^+ electrolyte.

3.4 Conclusion

In summary, we demonstrated the synthesis of nanotube structured titanium nitride with tunable length and diameter through a facile approach of anodization and nitridation of Ti metal foil. The as-prepared highly structured TiN nanotubes exhibit varying length from 4.5 to 30 μm and diameter from 35 to 100 nm. Cells using this TiN nanotube, used as a host matrix of sulfur for Li−S battery, show high capacity (1338 mAh g^{-1} after 180 cycles at 0.1 C rate) and long-cycle life (only 0.064 % decay per cycle on average) at high sulfur contents. In addition, TiN nanotubes electrode with varying diameter and length indicates that increase in nanotube length from 4.5 to 30 μm and decrease in nanotube diameter from 100 to 35 nm enhance capacity by 19.1% and 24.7% after 180 discharge/charge cycles, respectively. This outstanding improvement is due to unique characteristics of the TiN naotubes with larger length and smaller diameter: a higher surface area, ability to buffer the stress, suppression of diffusion of soluble polysulfides, and the formation of a more effective matrix. This research thus presents a promising path for further development in Li−S batteries, as it not only demonstrates an effective cathode material, but also indicates the importance of size effect of materials on battery performance

4 CHAPTER 4 NOVEL CATHODE FRAMEWORK OF NANOSTRUCTURED TITANIUM NITRIDE/GRAPHENE FOR ADVANCE LITHIUM SULFUR BATTERIES*

4.1 Introduction

The demand for developing clean and sustainable energy technology has been increasing because of the steadily growing pollution problem caused by fossil fuels.[18, 128, 133, 135] The market of electric vehicle (EV), hybrid electric vehicle (HEV) and portable electronic devices is currently dominated by conventional lithium ion batteries due to their high energy and power density, low self-discharge, and availability of various types.[176-177] Nevertheless, the improvement of energy and power densities of rechargeable lithium batteries is still attracting significant attention aiming to providing longer driving range of EV and further decreasing the emission of greenhouse gases.[19, 128, 130, 133] One of the main challenges to realizing a longer driving range is to develop cathode materials with much higher specific capacities to match with those of the anode materials.[133] The theoretical specific capacity of sulfur (1675 mAh g^{-1}) makes it a promising cathode material, with ~5 times higher capacity than those of traditional Li-ion cathode materials. Also, it is worthy noted that sulfur possesses other advantages such as natural abundance and environmental friendliness.[18, 126, 135, 143]

Though all these significant advantages, there are a number of challenges in Li-S battery systems. The first one is low electrical conductivity of elemental sulfur to hindering electron transfer.[143] Both elemental sulfur and its lithiated product are non-conductive, producing an inevitable need of incorporating S into conductive matrix to facilitate reductions.[178] The second one is high self-discharging and loss of active materials as a

result of migration of highly soluble higher-order polysulfide (S_x^{2-}, $2 < X \leq 8$) in organicelectrolyte. These intermediate reduction products can diffuse through the electrolyte to the anode (Li metal) as a result of concentration gradient, where they will be further reduced to form precipitates (Li_2S_2, Li_2S) on lithium metal surface.[148] The third one is capacity fading as a result of drastic electrode volume shrinkage and expansion.[38] The deterioration of the electrochemical performance during cycles[22, 31, 135, 143, 146-148, 151, 179-180] is due to density differences of elemental sulfur and lithium sulfide products. These hindrances of Li-S systems can lead to loss of active materials, low Coulombic efficiency, self-discharging and rapid capacity fading of the battery.

The rational design of the cathode, lithium anode protection, and electrolyte modification have been extensively investigated to improve the electrochemical performance of Li-S batteries.[160] There are increasing attentions to incorporate sulfur with conductive matrix in order to immobilize the dissolved polysulfides. Carbon materials, with high electrical conductivity, mechanical durability, and low-cost, have been widely used as a host matrix to be impregnated with sulfur. Numerous cathode materials are designed and developed by hybridizing various nano-structured carbon materials with sulfur (e.g., porous carbon with desirable pore size,[82] single/multi-walled carbon nanotube,[83] carbon nano-fiber,[181] graphene,[34, 182-183] and the composite mixture of fore-mentioned materials[132, 184]). It is worthy noting that the electrochemical performance of lithium sulfur battery systems has been effectively enhanced by these well-designed and high-structured C/S compounds. However, the challenge of rapid capacity decay still needs to be addressed, although some studies have shown promising capacity retention results.[165,

[185] Thus, a series of metal-oxides, nitrides, and chalcogenides have been investigated as cathode matrix materials for their adsorption capability of polysulfides. Metal oxide (e.g.

TiO_2, TiO, Al_2O_3, MnO_2, VO, Mn-Sn oxide, etc.), metal sulfide (CuS, CoS_2 and FeS_2), and metal chalcogenide have been proposed as immobilizer for polysulfide, but they still suffer from various shortcomings with only limited success.[123, 137, 142, 151-152, 186-191] Many metal oxides/sulfides have intrinsically poor electrical conductivity, thus the adsorbed polysulfides are difficult to be reduced directly on the host surfaces, resulting in relatively lower sulfur utilization. Recently, titanium-based materials, including Ti_4O_7, Ti_2C, TiC, TiN, TiCN and TiO, have been demonstrated to be an effective cathode material matrix as highly promising Li polysulfides (LiPS) immobilizers and good media for electron transfer.[192-193] Especially, titanium nitride (TiN) stands out for exhibiting significant advantages such as low cost, high electrical conductivity, outstanding mechanical and chemical stability, and excellent entrapment ability towards polysulfides.[28, 123, 187] In our previous work, we have demonstrated the enhanced electrochemical performance of the nano-structured TiN serving as cathode matrix in Li-S batteries. Moreover, the effects of tunable dimension of the TiN nanostructures on electrochemical performance have been elucidated.[194] However, non-negligible fading of capacity still exists. This is attributed to that the cathode matrix gradually lost its retention of the drastically increasing polysulfides, especially when it comes to a higher areal loading of sulfur, associated with a more severe shuttling mechanism. In addition, the structural failure has also been observed due to severe volume change during charge-discharge cycles.[38, 185]

In this study, the electrochemical performance and capacity retention in the Li-S battery using cathode matrix composites of TiN nanotubes (TiN NT) hybridized with graphene are investigated. Nanoscale host of sulfur in TiN nanotubes is packed efficiently and connected closely by graphene who acts as anchoring support.[184, 186, 195]

The combination of 1-D TiN nanotubes and 2-D graphene (G) constructs a 3-D hierarchical framework, which may enable efficient electron transfer, sufficient electrolyte accessibility and flexible composite structure as well as inhibits the detachment of polysulfides. This is the first TiN nanotube/graphene nanostructures study which demonstrated significantly better electrochemical performance than previously reported 3-D nanostructures[159, 195-197] with TiN nanowires, carbon nanowire, and carbon nanotubes. The TiN nanotube, compared to conventional carbon nanotube, could serve as a more efficiently cathode framework since it is not only with better chemisorption effect but also maintain a high conductivity and structural stability.[28]

4.2 Experimental

4.2.1 Preparation of cathode materials of nanostructured TiN and graphene

Synthesis of TiN nanotube arrays has been described elsewhere.[194] In this work, TiN nanotube arrays were synthesized with an anodization voltage of 60 V for 6 hours.

The composite cathode was prepared as follows: Different ratios of TiN nanotubes and graphene were mixed with ethanol (25 wt%) solution. The suspended mixture was then ultrasonicated for 1 h, followed by heating at 50 C for 12 hours. The composite was further incorporated with sulfur at a wt. ratio of 35:65 by melt-diffusion method.[159] The sulfur/composite mixture was first heated above the melting temperature of sulfur at 115 °C and maintained for 30 minutes. 5 wt% of poly(acrylonitrile-methyl methacrylate) (AN/MMA=94:6, Polysciences Inc) was dissolved in N-methyl pyrrolidinone (NMP) to form a binder solution. A wt. ratio of 2.23 of binder solution to S@TiN composite was used to form cathode slurry. The slurry was then coated on Al foil (8.5mg cm^{-2} areal loading of sulfur) and dried at 80 °C under 10^{-5} torr for 10 h.[28, 184, 194] Furthermore, composites with TiN nanotubes:graphene ratios as 1:0, 2:1, 1:1, 1:2, 0:1 were also prepared. TiN nanoparticles were used as to compare the structural effect of TiN on battery performance.

4.2.2 Assembly of coin cells

1,3-Dioxalane, 1,2-Dimethoxyethane, LiTFSI, LiNO3 were purchased from Aldrich and used as received. An electrolyte with 1 M of 1,3-Dioxalane, 1 M of 1,2-Dimethoxyethane, 1 M LiTFSI, and 2 wt% LiNO3 was prepared by stirring at 80 ℃ for 6 h. Stainless steel coin cells (2,032-type) were assembled inside an Ar-filled glovebox with a Polypropylene separator (Celgard 2400), lithium foil (Sigma Aldrich, as rolled, 99.9% purity) anode, and 8 μL of electrolyte solution added onto the cathode.

4.2.3 Material characterization and electrochemical measurement

Phase purity and crystal structure of cathode materials were characterized using a X-Ray Diffractometer (Rigaku Miniflex 600). Morphological features of the cathode materials were observed with scanning electron microscopy (TESCAN, model S9000). To determine the sulfur content of the composites, thermogravimetric analysis (TGA, Q500 model from TA instruments) was performed on the composite in a temperature range of 25 – 700 °C with a heating rate of 5 °C min-1 under a nitrogen gas atmosphere.

Galvanostatic discharge-charge tests were conducted using a battery cycler (Maccor Model 4200) between the voltage range of 1.6 to 3 V (vs. Li/Li+) at room temperature. Electrochemical Impedance Spectroscopy (EIS) experiments were performed using a potentiostat (Gamry reference 3000). The minimum amplitude of AC voltage was 0.1 mV. The frequency was swept from 0.1 Hz to 100 kHz.

4.3 Results

Fig. 1a and b, shows the morphology and microstructure of the TiN/G composite characterized by scanning electron microscopy (SEM). SEM images (Fig. 1a) reveal a 3-dimensional framework of TiN nanotubes and graphene nanoplatelets. The inset image

enlarges a cross-section view of nanotube arrays to indicate their arrangement and size. The TiN nanotubes are typically 65–75 nm in diameter and 15–20 μm in length. Plentiful voids of nanostructure may hold a large amount of sulfur and provide good electrolyte accessibility.[165, 198] On the other hand, the internal stress caused by volume variation of sulfur element may be alleviated during charging/discharging cycles.[83, 166, 194, 199] In Fig. 1b, the SEM image shows the dispersion of TiN nanoparticles (TiN NP) on graphene nanoplatelets. The typical diameter of TiN nanoparticles is 65~75 nm. As shown in Fig. 1c and d, the pristine TiN nanotube arrays on Ti foil indicate clearly their morphology from sideview and topview, respectively.

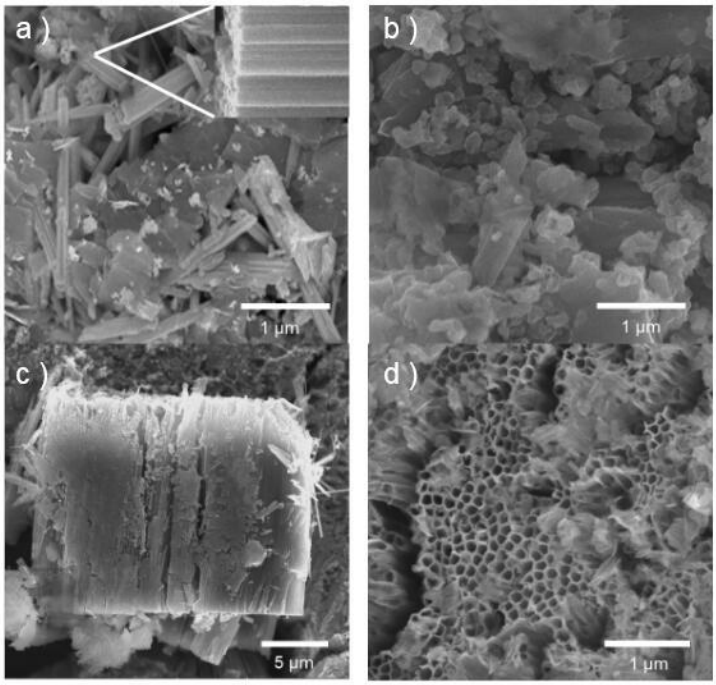

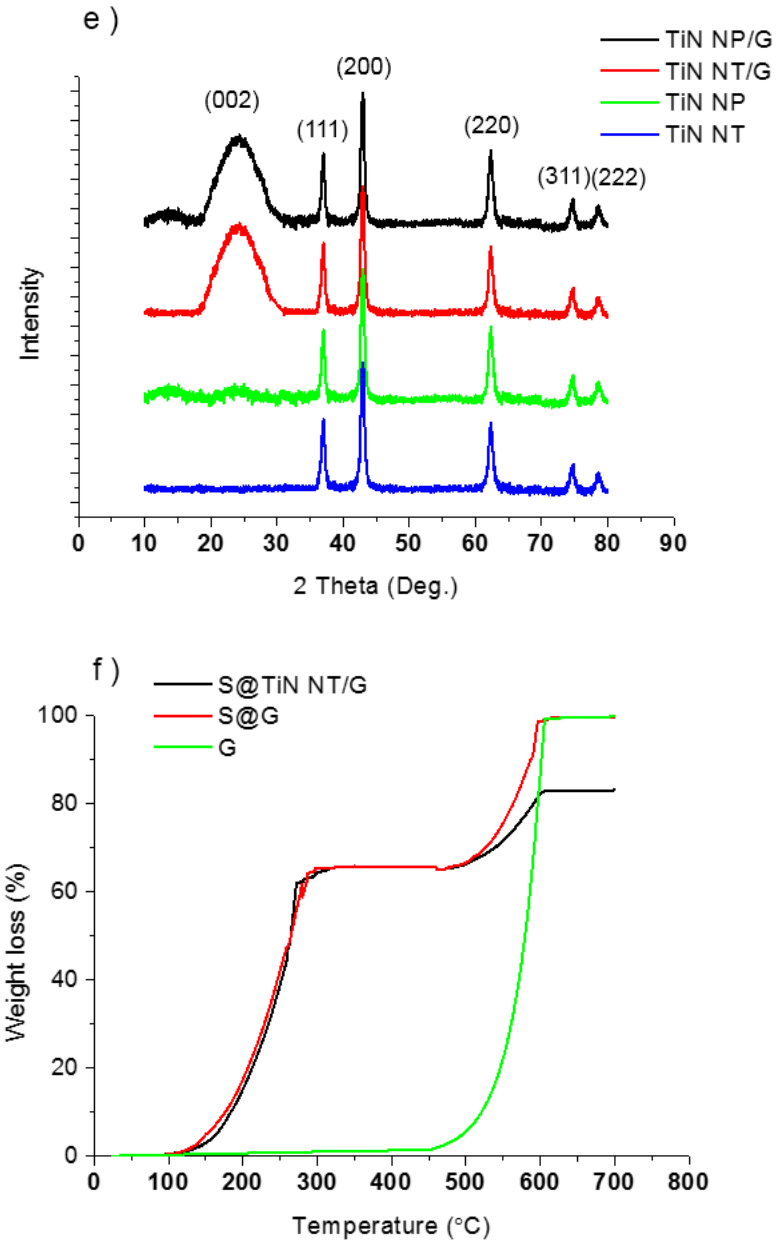

Figure 4.1 SEM images of the surface morphology of the (a) TiN NT, (b) NP with graphene composites, and TiN NT arrays (c) sideview and (d) topview. Inset picture of (a) shows an image of TiN nanotube arrays. (e) XRD patterns and (f) TGA results.

The crystal structure of the TiN nanoparticles, nanotubes and their composites with graphene nanoplatelets were further examined by X-ray diffraction (Fig. 1e). The X-ray diffraction (XRD) spectra of the prepared TiN with five diffraction peaks at around 37 °, 43 °, 62 °, 74.5 °, and 88.5 °, corresponding to the TiN (111), (200), (220), (311) and (222)

crystal planes, respectively.[28, 187] There is no observable difference in the diffraction spectra of of TiN nanotube and nanoparticles. The positions and intensities of TiN diffraction peaks can be indexed to the face-centered cubic structure of TiN (JCPDS file no. 38-1420) with a lattice constant a = 0.424 nm. With the addition of graphene, both composites exhibit a wide peak around 26 ° corresponding to (002) crystal plane of graphene.[184]

Fig. 1f shows the TGA spectra of pure graphene, sulfur/graphene (S@G) and sulfur/TiN/graphene (S@TiN/G) over the temperature range from 25 -700 ℃. Pure graphene exhibits a single step of weight loss over the temperature range of around 460 – 600 ℃, while the S@G indicates a two-step weight loss at around 160 – 290 ℃ and 500 – 600 ℃ which corresponds to the evaporation of sulfur and decomposition of graphene, respectively. Similarly, S@TiN/G indicates a two-step weight loss TGA curve as S@G. However, TiN remains stable in the sample up to 700 C[83, 184].

The weight losses shown in both S@G and S@TiN/G are around 65%, which agrees with the designed sulfur loading. This high sulfur loading allows a higher energy density for practical applications and compared favorably to other studies which sulfur loadings are typical in the 50% range.[200-201] Compared to the S@G composite, the S@TiN/G exhibits a slightly higher sulfur loss temperature. This could be attributed to the 3D structure of S@TiN/G which retards the escape of sulfur. Similar phenomenon was observed in S/G and S-CNT/G.[161, 184] A slightly higher decomposition temperature of graphene was also observed during the second step of weight loss.

To investigate the effects of nanostructure of TiN and graphene support on the electrochemical performance of sulfur cathode, galvanostatic charge-discharge cycles were

measured. Fig. 2a shows the cycling performance of four TiN electrodes (NP, NT, NP/G, NT/G) at a current density of 0.1 C for 180 cycles. S@TiN NT delivers the highest initial discharge capacities of 1,535 mAh g^{-1}, while S@TiN NT/G and S@TiN NP/G provide around 1420 mAh g^{-1}, and S@TiN NP gives only 1385 mAh g^{-1}. After 180 cycles, the discharge capacities of S@TiN NT, S@TiN NP, S@TiN NT/G, and S@TiN NP/G are 1195, 990, 1205, and 1085 mAh g^{-1}, indicating a capacity retention of 78.9%, 69.1%, 87.5% and 78.1%, respectively. It is interesting to note that the graphene supported TiN nanostructures exhibit a >10% capacity retentions compared to the unsupported composites. The findings suggest that highly-structured hollow hosts of TiN NT intercalated with graphene can provide an anchoring effect of stabilizing the structure and suppress the diffusion of soluble polysulfides, thus enhancing the cycling stability.[131-132] It is shown in the Nyquist plots (Fig. 2b) that the smaller semicircle diameter has been observed of S@TiN NT in high-frequency region, demonstrating the lowest initial charge transfer resistance (Rct) as 16 ohms. The electrodes of S@TiN NP and S@TiN NT/G indicate charge transfer resistance of 19 and 22.5 ohms, respectively, which are higher than that of S@TiN NT. Furthermore, the electrode of S@TiN NP/G reveals the highest charge transfer resistance (30 ohms). The difference of charge transfer resistance represents reasonably the conductivity of host materials in cathodes,[202] since all cathodes were synthesized with the mass loading of sulfur. Nonetheless, after 180 cycles, these electrodes show a different extent of resistance increase than that of fresh samples. While the electrode of S@TiN NT/G shows a smallest charge transfer resistance of around 15.5 ohm, the charge transfer resistance of electrodes of S@TiN NT, S@TiN NP/G and S@TiN NP are 18.5, 26, and 34.5 ohm, respectively. It is shown in Fig. 2c that the percentage of increase of charge

transfer resistance after 180 cycles is smallest indicating TiN NT/G is the most stable conductive matrix. It can be attributed to the fact that more effective conductive hosts of sulfur promises better discharge capacity.[34, 186] The enhanced capacity maybe attributed to nano-confinement of sulfur within TiN nanotubes and effective transfer of electrons and ions by graphene, and as well as a more stable, integrated 3-D structure.[197, 203] On the contrary, the S@TiN NP electrode shows the most significant decay with the highest charge transfer resistance after 180 cycles, as a result of the relatively poor stability of TiN nanoparticles matrix.

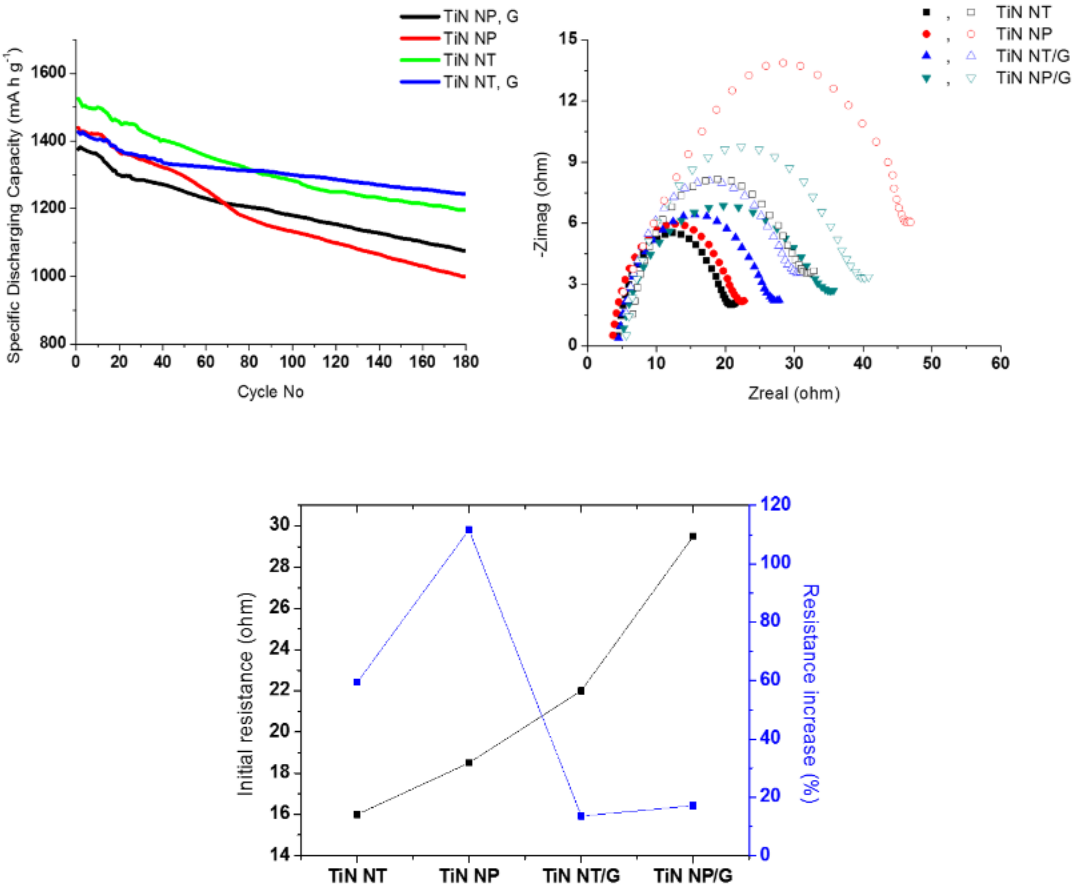

Figure 4.2 (a) Galvanostatic charge–discharge curves of TiN/G composites. (b) EIS plots for TiN/G composites before (solid symbols) and after 180 cycles (open symbols). (c) Initial resistance and % resistance increase of TiN/G composites.

Since integrating 2-D graphene with 1-D TiN nanotube has shown a better performance, the effects of TiN/graphene ratio in the hybrid framework on electrochemical stability and capacity retention are investigated. Fig. 3a and b show the cycling performance of five electrodes at a current density of 0.1 C for 180 cycles. The electrodes deliver increasing initial discharging capacities of 880, 1025, 1420, 1449 and 1521 mAh g^{-1} as the ratio of TiN nanotubes gradually increases from 0, 33.3%, 50%, 66.6%, and 100%, respectively. This can be attributed to higher utilization rate and better reaction kinetics as a result of effective trapping capacity of soluble polysulfide and high conductivity of TiN nanotubes[204]. However, the discharge capacities of the electrodes indicate a different order after 180 cycles, compared to their fresh state. The composite electrodes of S@TiN NT/G with a compositon of TiN ranging from 100% to 66.7%, and 50% exhibit 1179, 1204, and 1247 mAh g^{-1}, with the capacity retentions of 77.4%, 82.6% and 87.3%, respectively (Fig. 3b). The most stable composite cathode was found to be the 1: 1 of TiN to graphene, suggesting that the combination of nanotubes structures and graphene can be more effective in limiting the diffusion of polysulfide into electrolyte. On the other hand, the cathode of S@TiN NT/G with the 33.3 % TiN shows a lower battery performance with a capacity retention of 72.7% after 180 cycles. The lower capacity of 746 mAh g^{-1} at 180^{th} cycle can be attributed to the fact that although a higher graphene content should facilitate electron and ion transportation and provide a better structural support, a lower TiN nanotube content limits polysulfide entrapment. When the matrix is pure graphene, the suppression of polysulfide migration is further hindered.[205] Without the polar and highly structured TiN nanotubes in the composite, S@G indicates the highest capacity fading among all electrodes. The capacity is only 536 mAh g^{-1} after 180 cycles, which is 61.1%

of its initial value. The drastic decay of capacity suggests that 2-D material like graphene does not have effective confined space to trap the polysulfides without the reinforcement of 1-D nanostructured material.[206] The coulombic efficiency of all composites shown in Fig. 3c are above 95% with the 1:1 TiN/G shows the highest reversibility, and follow the same trend as capacity retention.

The rate capability of S@TiN NT composites with different ratio were studied from 0.1 to 0.2, 0.5, and 1 C, and back to 0.1 C, each for 10 cycles. Fig. 3d presents the effects of graphene contents (0, 33.3%, 50%, 66.7%, and 100%) on the rate capability of S@TiN NT/G composites. It is shown that the composite with pure TiN nanotubes possesses the largest capacities as high as 1547~1504 mAh g^{-1} at initial 10 cycles, while the composites with addition of graphene (weight ratio of TiN to graphene being 2:1 and 1:1) exhibit slightly lower capacities around 1457~1391 and 1431~1382 mAh g^{-1}, respectively. As the weight ratio of graphene increased to 66.7%, the capacity of electrode experienced a significant drop to 1025~985 mAh g^{-1}, and the capacity becomes even poorer (878~827 mAh g^{-1}) with pure graphene electrode. When the current density is increased successively, the S@TiN NT electrode delivers decreased specific capacities of 1504, 1193, 832, and 645 mAh g^{-1} at 10^{th}, 20^{th}, 30^{th}, and 40^{th} cycles, respectively. When the current density decreased back to 0.1 C, the specific capacities recovered to 1174 mAh g^{-1} (50^{th} cycles). On the contrary, the composite electrodes with graphene (weight ratio of 1:1 and 2:1) exhibit better rate capability with 802 and 729 mAh g^{-1} at 40^{th} cycle, and 1329 and 1238 mAh g^{-1}at 50^{th} cycle. These findings indicate a good tolerance to the rapid change of C-rates over tests, which could be attributed to a structural framework with better stability.[207] On the other hand, composite electrode with a lower TiN nanotubes content (weight ratio

of 1:2) delivers much lower discharge capacities in tests, which may be caused by the loss of active materials through LiPS dissolution. Due to the lack of nano-confinement structures (TiN nanotubes) as sulfur hosts, the pure graphene electrode shows the worst rate capability among all samples. Fig. 3e shows the galvanostatic charge/discharge curves of pure TiN NT, pure graphene, and composite electrode (weight ratio of 1:1) after 180 cycles. All three electrodes indicate two reduction plateaus and one oxidation plateau, which correspond to the typical redox reactions of sulfur. It is interesting to note the voltage gap between the oxidation and reduction plateaus is the smallest for TiN NT/graphene composite, suggesting better reversibility and lower polarization of electrodes. The voltage gap is higher for the pure TiN NT, while the highest gap was observed for pure graphene.

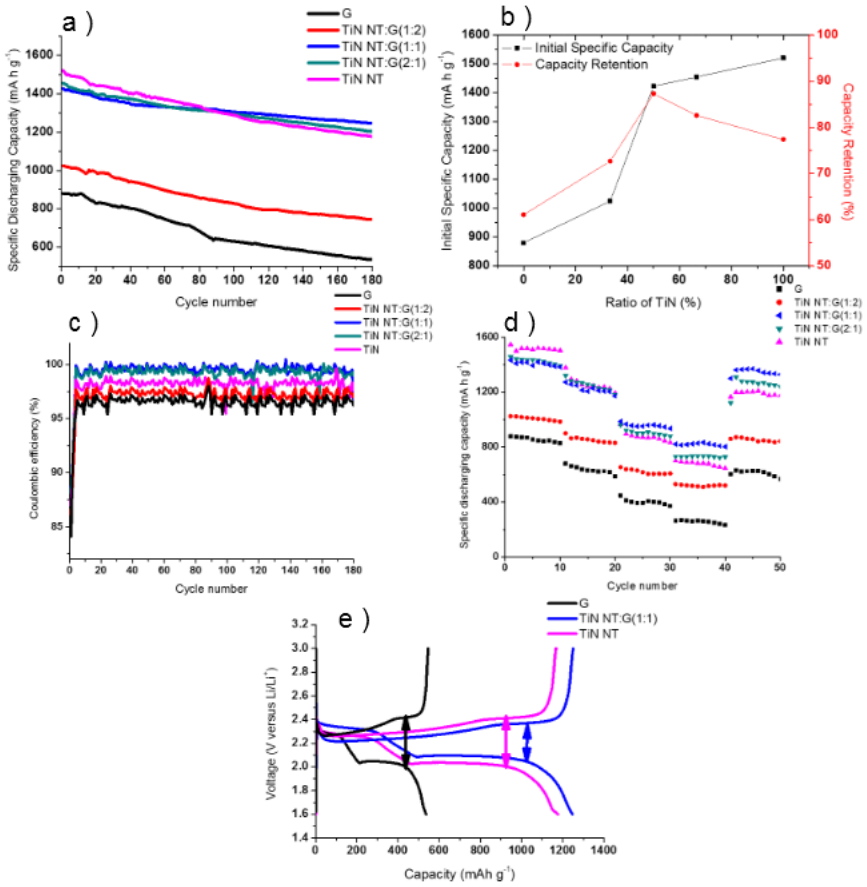

Figure 4.3 (a) galvanostatic charge–discharge curves, (b) initial specific capacities and % of capacity retention after 180 cycles, (c) coulombic efficiency, (d) rate capability, and (e) galvanostatic charge-discharge curves after 180 cycles of TiN/G composites.

The electrochemical impedance spectroscopic (EIS) test of various S@TiN NT/G electrodes are shown in Fig. 4. It is obvious that the initial charge transfer resistance (Rct) of the electrodes become larger as the content of graphene increases (Fig. 4a). The decrease from 31.5 (pure graphene) to 16 ohm (pure TiN nanotubes) indicates an excellent electronic conductivity of titanium nitride nanotubes. Moreover, cathodes with TiN NT:G (2:1, 1:1 and 1:2) have intermediate charge transfer resistance as 18.5, 24, and 28.5 ohm, respectively, which can be explained by lower interfacial electron transfer as a result of decreasing efficient and effective conductive path (TiN nanotubes).

EIS plots for the composite cathodes after 180 cycles further confirm the results and synergetic effect of integrated structures discussed above, as shown in Fig. 4b. The gradually increased charge transfer resistances are exhibited by pure TiN nanotubes, TiN NT/G(1:1), TiN NT/G(2:1), TiN NT/G(1:2), and pure graphene, indicating 27.5, 29, 30.5, 46.5, and 57 ohm, respectively. Fig. 4c clearly shows the percentage increase of charge transfer impedance of the cathodes are 62.7%, 59.5%, 14.5%, 61.4% and 67.7%, for 1:0, 2:1, 1:1, 1:2, and 0:1 TiN:G, respectively. The difference of increasing rates of Rct could be attributed to that the overall completion and effectiveness of conductive framework is damaged, introducing lower efficient conductive path for electrons and less localization of sulfur within confined nanostructure.[82, 147, 185] Thus, a larger increase of charge transfer resistance could be observed.

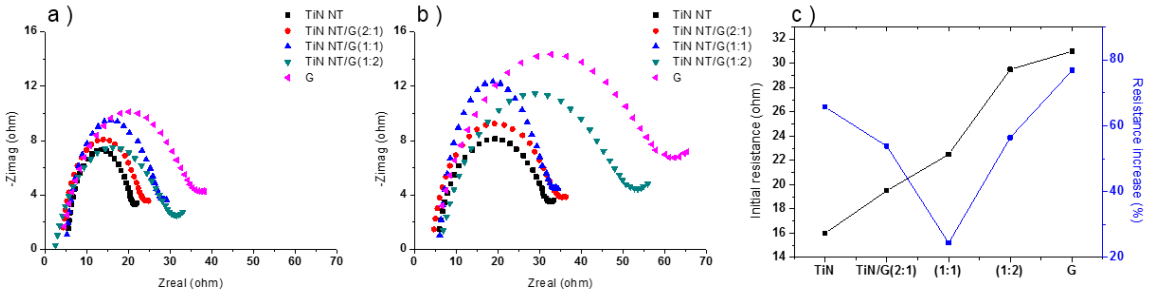

Figure 4.4 EIS plots for TiN/G composites with different ratio (a) before and (b) after 180 cycles, (c) Initial resistance and % resistance increase of charge transfer after 180 cycles.

The morphologies of the composite electrodes were characterized to gain a better understanding between electrode structure and battery performance (Fig. 5). Fig. 5a shows the SEM image of 2:1 TiN/G, higher amount of TiN nanotube bundles were observed as compared to 1:1 TiN/G (Fig. 1a). On the other hand, the 1:2 TiN/G (Fig. 5b) shows a significant amount of graphene sheets, compared to the 2:1 and 1:1 TiN/G samples. It can

be observed that there are no large sulfur particles aggregates among all the three electrode surfaces by SEM, indicating that a quite uniform impregnation of sulfur in the TiN NT/G hybrid nanostructures composite. Fig. 5c shows the SEM image of 1:1 TiN/G sample after 180 cycles. There are no obvious aggregation and mechanical fractures of TiN nanotubes, as well as no large amount of precipitation arises on the surface of the electrode. This suggests the 1:1 TiN NT/G hybrid framework is a well-sustained structure with sufficient trapping sites effectively minimizing the capacity fading by limiting the migration of soluble polysulfides.[208] The 2:1 and 1:2 TiN/G samples appear to be quite stable after 180 cycles as well (images not shown).

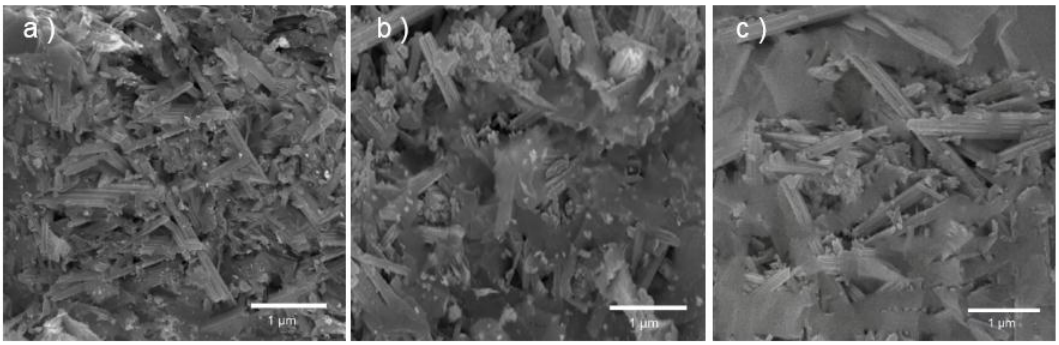

Figure 4.5 SEM images of the surface morphology of the composites with ratios of (a) TiN NT/G (2:1), (b) TiN NT/G (1:2) before cycles, and (c) TiN NT/G (1:1) after cycles.

Table 1 shows the sulfur content (as determined by EDS as a semi-quantitative tool) of the 1:0, 2:1, 1:1, 1:2, and 0:1 TiN/G samples initially and after 180 cycles. The % decrease of sulfur content are 90.1%, 79.3%, 43.3%, 56.2%, and 83.4% for 1:0, 2:1, 1:1, 1:2, and 0:1 TiN/G samples, respectively. Interestingly, the 1:1 TiN/G sample shows the best retention of sulfur among all samples, which are consistent with the trend of capacity retention (Fig. 3b). These results suggest the optimal 1:1 TiN/G sample provides the most effective physical barrier against polysulfide migration from the electrodes. TiN could provide strong chemisorption effect with polysulfide,[28] which can be ascribed to (1)

covalent bond formed between nitrogen and sulfur species because of the electronegativity and polarity of nitrogen; (2) strong Lewis acid-base bond between titanium and sulfur. Apparently, the optimal composition of graphene and TiN nanotubes leads to a synergetic, well-sustained framework providing outstanding electrochemical performance and cycling stability.[59, 192, 195, 200]

TiN/Graphene	0:1	1:2	1:1	2:1	1:0
S content (%) before cycle	42.6	42.1	42.5	41.8	42.8
S content (%) after 180 cycles	4.2	8.7	24.1	18.3	7.1
% decrease in S content	90.1	79.3	43.3	56.2	83.4

Table 4.1 S content (based on EDS analysis) of the composites with different ratios, before and after 180 cycles.

4.4 Discussion

In previous research on lithium sulfur batteries, lots of attempts have been tried to improve battery performance of lithium sulfur systems, based on different design of cathode framework. Wang et al. designed a sulfur cathode wrapped by graphene oxide sheet with poly(ethylene glycol) (PEG) as surfactant, with a specific discharging capacity nearly 600 mAh g^{-1} after 100 cycles under C/5.[38] Similarly, Evers et al. also prepared graphene-sulfur composite as cathode for lithium sulfur batteries.[34] The performance indicates a decay of 19% of capacity and specific capacity around 500 mAh g^{-1} after 50

cycles at a current rate of 0.2 C. Aligned or disordered nanotubes (mostly carbon nanotube, although conductive polymer nanotube in some research) have been incorporated with sulfur to act as conductive network. Xiao et al. synthesized an composite sulfur electrode with polyaniline nanotube,[185] with a capacity higher than 800 mAh g^{-1} after 100 cycles under 0.1 C. Yuan et al. and Cheng et al. both reported a sulfur cathode with carbon nanotube, showing reversible capacities of 670 and 560 mAh g^{-1} after 60 and 90 cycles, respectively.[166, 175] Moreover, Sun et al. integrated carbon nanotubes with graphene as cathode matrix, showing a capacity of 818 mAh g^{-1} after 200 cycles at 1 C.[184]

The integrated structure of 2-D graphene and 1-D nanosized conductive tube differs itself from previously Li-S battery studies with nanoparticles or 1-D nano-tube/fiber cathode composites. Compared to other matrix with complex structures reported in literature,[182, 184, 195, 197] the optimal TiN NT/G hybrid conductive network was found to exhibit the best electrochemical performance with highest stability.

The electrode with pure TiN nanotubes delivers the highest specific capacities in nearly first 90 cycles, the notable electrochemical performance could be ascribed to the excellent properties of TiN nanotube, as described in detail in our previous work.[28, 194] Firstly, each self-confined nanotube structure is acting as a reaction chamber, enabling a fast reaction kinetics of the electrochemical redox reactions of sulfur.[209] This could be ascribed to more reaction sites as a result of the nanoscale framework, thus expedites ionic oxidation and reduction. Moreover, the interior space of nanostructure should provide an effective confinement of soluble polysulfides which further limit their shuttling through electrolyte and minimize the loss of active material.[35, 167] In addition, the segregation of sulfur into smaller particles leads to lower volume change and stress over

charging/discharging.[38, 76, 122] Unfortunately, it should be noted that pure TiN nanotube exhibits nearly 25% specific capacity loss after 180 cycles at 0.1 C, suggesting 1-D nanostructure may not be optimal as a stable framework for Li-S battery. With the addition of 2-D graphene nanoplatelets integrating with 1-D TiN NT, the rate of capacity fading decreases. This could be attributed to that 1-D TiN nanotube with 2-D graphene resulted in a more stable spatial arrangement of 1-D TiN nanotube leading to higher diffusion of polysulfides. The integrated structural design promotes a more uniform dispersion of TiN nanotubes, thus the stability of the framework could be considered to provide more tolerance and flexibility to accommodate internal stress by volume change arises.[205, 210] Interestingly, further increase in graphene content to a 1:1 ratio with TiN nanotubes provides the best long-term (180 cycles) electrochemical performance and cycling stability. However, if the content of graphene is increased to 2:1 ratio with TiN nanotubes, the specific capacity and cycling stability are significantly lower. This suggests the synergistic effects observed with 2:1 and 1:1 TiN NT/G samples do not exist in the TiN NT/G 1:2 sample. Although the addition of graphene as 2-D supportive plate to improve the TiN nanotube matrix to confine more polysulfides, a lower amount of TiN nanotubes with excessive graphene may not allow the formation of a homogeneous and well-dispersed framework. The 1:1 ratio of TiN NT/G sample demonstrated the best battery performance and stability which can be attributed to a conductive and stabilized network which facilitates good charge transfer from/to the nearly insulating active sulfur. Moreover, the pores of hybrid-structure are with sufficient size to enable access by electrolyte and maintain a robust ionic transport of Li^+ to the active sulfur.[28] Though 3-D structure has been utilized previously to study for the improvement of battery performance,[159, 161, 195-196]

this work demonstrated a superior battery performance and cycling stability. The findings of this work should contribute to the rational cathode designs of 3-D composite network for next-generation Li-S batteries,[160, 204] which consists of 1-D conductive nano-confinement of polar materials and 2-D materials as supportive anchor.

4.5 Summary

In summary, we have investigated the effect of nanostructure of titanium nitride (TiN NP/NT) on the battery performance of Li-S batteries, as well as their composite with the addition of graphene. The composite electrode of TiN nanotubes and graphene apparently demonstrates the highest specific capacity and cycling stability after 180 charging/discharging cycles. Its specific capacity still maintains at 1217 mAh g^{-1} with a capacity retention of around 87% after 180 cycles under 0.1 C rate. The 3D conductive network not only promotes the transfer of ions and electrons, but also facilitates the accessibility of electrolyte to enhance the reversibility of redox reactions in each nano-sized reaction chamber. Moreover, the structural stability could be improved by (1) the supportive effect of graphene and (2) the enhanced stress relief because of smaller sulfur particles within the interior space of nanostructure.

A facile method assisted by ultrasonication and melt-diffusion were used to synthesize cathode materials with different ratio of graphene and TiN nanotubes. The composite with ratio of TiN nanotubes and graphene as 1:1 delivered the best battery stability with a retention rate of 87.5% after 180 cycles, although initial specific capacities are not the highest. The optimal balance between specific capacity and retention rate of the composite electrode could be attributed to the synergetic effect stemming from the hybrid framework of 1-D TiN nanotubes and 2-D graphene. The results of this study may lead to rational

design of hybrid nanostructured cathode materials with high energy density, power density and battery durability for the next generation of energy storage systems.

5 CHAPTER 5 DESIGN OF ADVANCED THICK ANODE FOR LI-ION BATTERY BY INSERTING A GRAPHITE/POLYMER BUFFER LAYER: AN IN-SITU MECHANICAL STUDY*

5.1 Introduction

The reality of exhaust gases of automobiles being accounted for a large portion of air pollution and the gradual depletion of fossil fuel has generated a huge demand for emerging hybrid electric vehicles (HEV) and electric vehicles (EV).[27, 211-214] However, traditional lithium ion batteries (LIB) have relatively low volumetric and gravimetric energy densities for electrified vehicles. In order to address this issue, many researchers have investigated new materials with higher energy densities, such as silicon, to replace the traditionally used carbon-based electrode materials in anodes. Nevertheless, silicon could not maintain acceptable cyclability and stability due to inevitable mechanical failure during cycles, causing issues such as cracking of materials and delamination of electrodes from current collectors.[215-216] Numerous structures have been proposed to facilitate stress/strain relaxation and transport of lithium ion, including silicon nanotubes, silicon nanowires, micro/nano-porous silicon, and hybrid silicon/carbon nanostructures.[217-221] While these approaches have been shown effective, it is still challenging for mass production of thick anode electrodes containing silicon, limiting their potential for commercialization. In fact, most studies of nanomaterials use very limited amount of active materials, and it is not clear if they can provide sufficient capacity for EV/HEV in a cell level, especially for long-distance drive.

In conventional LIB, the anodes are typically made of graphite particles mixed with polyvinylidene fluoride (PVDF) binders on the copper current collector. Combination of

*This chapter has been published in Electrochimica Acta, Volume 281, 10 August 2018, Pages 282-291.

thick graphite electrode and silicon materials represents an attractive approach for practical EV/HEV applications.[222-223] However, this design still faces poor mechanical stability where the electrode is typically delaminated from the current collector after a long cycle.[224] In order to mitigate this adverse effect, a new design of advanced LIB electrodes is proposed in this paper, in which a "buffer layer" is added between the active material and the current collector. The buffer layer is designed to have an intermediate elastic modulus to limit the large strain (volume expansion) difference between the active material and the current collector. It is expected the characteristic of the interface between the active material and the current collector could be improved, leading to better structural stability. To further validate the improvement of structure deformation for the novel designed battery electrode in a quantitative way, white light interferometry (i.e. WLI) is utilized to in-situ measure the deformation of electrodes during charging and discharging. In the literature, real-time stress measurements of battery material are typically conducted by multiple beam optic sensors (MOS),[225-230] which required samples to be in a wafer scale and with a thick supporting substrate of lower sensitivity.[231-232] Herein, we demonstrate a new experimental technique using cantilever-shaped microstructures made of conventional electrode materials. Since copper is mechanically elastic and electrochemically inert during cycling, suspended copper cantilevers would be deformed thanks to the volume expansion of active materials during electrochemical reactions.[233-234]

The paper presents a comparative study of how the buffer layer between the conventional active material layer and the current collector has an effect on electrode deformation and electrochemical performances. The theoretical capacity is 372 Ah kg^{-1} if made of pure graphite.[211] To increase the capacity, 6% silicon was added. SEM and EDX

mapping were conducted to demonstrate the specific layered-structures of the modified and the original samples. Moreover, in-situ deformation of the cantilever electrodes was characterized by WLI to indicate the differences of deformation between electrodes with different layer structures. Also, electrodes with different design were tested in coin cells to show the effect of this structural modification on battery performances.

5.2 Experiments

5.2.1 Electrode preparation and cell assembly

The anode (original sample) was made as silicon/graphite composite, of 6% of silicon particles (crystalline, 5-10 μm), 10% of PVDF (Kureha KF1100) and 84% of mesocarbon microbead graphite (MCMB, 15-20 um) coated onto the current collector layer of a thickness of 20 μm. The layer of active materials was controlled as 40 μm. Also, the sample with a buffer layer uses the same material, with the addition of an insertion of buffer layer (10% of PVDF and 90% of MCMB graphite, thickness of 30 μm) between active material layer and current collector. The cantilevers were machined using high-energy short-pulse laser to remove excess active materials and copper. The as-prepared cantilever was mounted into a home-made cell and the experimental setup is shown in Fig. 1c, where a 3D optical microscopy was used to in-situ characterize the deformation of the cantilever-shaped anodes, and the electrochemical cycles were controlled by a potentiostat (Gamry G300). The composite materials of silicon particle and graphite carbon were used as the working electrode, and the lithium foil was employed as the counter electrode. The smooth copper side of cantilevers was faced up. Liquid electrolyte of 1M $LiPF_6$ in ethylene carbonate (EC) and diethylene carbonate (DEC) with 1:1 ratio was used to fill up the cell chamber. The effective areal capacities were calculated as 3.39 mAh cm^{-2} and 1.35 mAh

cm^{-2} for original and modified sample based on their chemical composition and effective area, respectively.[211, 221] Since the cantilever electrode was immersed into the electrolyte and covered with a quartz in the cell. The optical length has been changed. A calibration procedure was performed to compensate the difference in optical lengths between the reflected and reference lights.[235] A liquid lens was added in the path of reference light, which has two quartz windows with total thickness the same of the quartz window in the cell and filled with electrolyte with the same distance between the cantilever and quartz window in the cell.

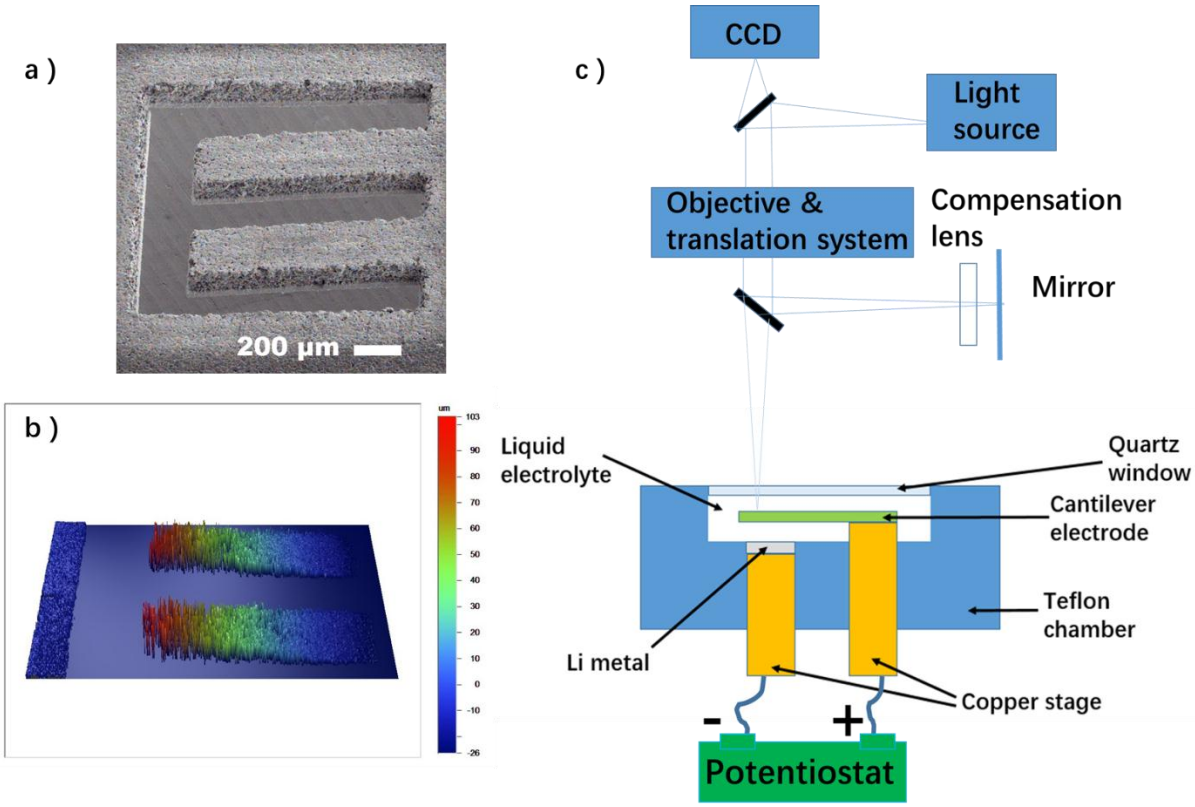

Figure 5.1 (a) SEM image of cantilever-shaped electrode, (b) 3D interferometry image of the cantilever anodes obtained by WLI, and (c) illustrative image of experimental setup for in-situ electrode stress measurement.

5.2.2 Real-time and in-situ strain measurements

WLI was used to measure in-situ 3D profiles. The curvature and deflection were monitored with 3D optical microscope (Bruker Contour GT In-Motion) accompanied with a through

transmissive media (TTM). The difference of optical path between height change of the sample surfaces and reflection from a reference mirror can be detected by an imaging sensor. The pattern of interference would be transformed as varying image signal, demonstrating the deformation of tested sample.[236-237] Corresponding deformation and stress evolution in anodes during electrochemical cycles were measured by detecting the curvature and deflection variation of the cantilever-shaped electrodes.

During lithiation and delithiation in electrochemical cycles, the insertion and extraction of lithium ions into and out of active materials layer would cause corresponding expansion and shrink. By fabricating the working electrode into the shape of cantilever, the stress caused by expansion and shrink in active material layer would induce the whole bilayer or triple-layer cantilever to deform and introduce the mechanical behavior of curling up or down of the cantilever structure. The corresponding change of cantilever curvature could be monitored using WLI. This procedure could be analogous to the case of thermal expansion of a multi-layer cantilever, in which different layers possess varying thermal expansion coefficient (α_1, α_2). The curvature could be correlative to the thermal strain, (α_1–α_2) ΔT, with the relationship as:

$$\kappa = \frac{6(1+m)^2(\alpha_1-\alpha_2)\Delta T}{3(1+m)^2+(1+mn)(m^2+\frac{1}{mn})}\frac{1}{h_t} \qquad (2.1)$$

where h_t means the total thickness of bilayer cantilever, $n = E_1/E_2$ and $m = h_1/h_2$. E_1 , E_2 and h_1, h_2 mean Young's modulus and thickness of the coated thin film and the substrate, respectively.[238]

In our current study, the mechanical stress is induced by the volume changes during electrochemical cycling instead of thermal expansion, therefore the thermal strain term in Eq. (2.1) is replaced by a free actuation strain of the Si/MCMB during lithiation and delithiation when it is not attached to the copper. When an additional buffer layer is added, the cantilever beam turns out a trilayer structure, and the bilayer Timoshenko equation needs to be modified as[239]:

$$\kappa = \frac{6m_a n_a(1+m_a+m_b^2 n_b+m_b(2+m_a n_b))\alpha}{(1+m_b^4 n_b^2+4m_a n_a+6m_a^2 n_a+4m_a^3 n_a+m_a^4 n_a^2+4m_b^3(n_b+m_a n_a n_b)} \frac{1}{h_{Cu}} \quad (2.2)$$
$$+6m_b^2(n_b+2m_a n_a+m_a^2 n_b n_a)+4m_b(n_b+3m_a(1+m_a)n_a+m_a^3 n_a n_b))$$

Where α is the free actuation train of the Si/MCMB layer, h_{Cu} means the thickness of copper substrate, m_{a} and m_{b} mean the ratio of thickness of silicon/graphite layer and buffer layer to copper substrate, n_{a} and n_{b} mean the ratio of elastic modulus of silicon/graphite layer and buffer layer to copper substrate, respectively.[239] The height change was assumed to be linearly proportional to state of charge (SoC) based on the previous literature.[20] However, the active composite material is porous with casing constraint from the substrate and thus results in nonlinear volume expansion. Modeling volume changes in porous electrode has been discussed,[240] and modeling volume and porosity changes coupled to the developed stresses during intercalation was further studied. To simplify the estimation of the thin film thickness, the porous electrode volume expansion model was assumed to be isotropic as

$$\frac{\partial}{\partial t}(1-\varepsilon)+(1-\varepsilon)\frac{\partial \varphi}{\partial t}=-\frac{s\Delta\hat{V}}{n\mathcal{F}}j \quad (2.3)$$

where ε is porosity, φ is volumetric strain, s is stoichiometric coefficient, n is electron number transferred in reaction, $\mathcal{F}$ is Faraday's constant, $\hat{V}$ is molar volume of reaction product, and j is electrochemical reaction rate.[241] In addition, considering the compressibility of the porous electrode C_E treated as continuum of fractions of solid phase and pores from rock mechanics, one obtains the relation[241]

$$C_E=-\frac{1}{V_m}\frac{dV_m}{d\sigma} \quad (2.4)$$

The subscription m denotes the portion of changes from mechanical forces rather than intercalation. From the strain definition

$$V_m=V_m^0(1+\varphi_m) \quad (2.5)$$

one can solve for the strain from Eq. 2.4:

$$\varphi_m = e^{-\gamma\bar{\sigma}} - 1 \tag{2.6}$$

where $\bar{\sigma}$ is dimensionless stress defined as $\bar{\sigma} = C_C\sigma$, and $\gamma = \frac{C_E}{C_C}$.[241] C_C is the compressibility of casing, a concept of a real or virtual case that limits the volume expansion, where C_C = 0 is rigid casing and $C_C = \infty$ implies no constraint. In the case of our electrode, C_C is referred to the substrate. Adding strain due to intercalation, the total strain turns out

$$\varphi = e^{-\gamma\bar{\sigma}} - 1 + \frac{s\Delta\hat{V}}{n\mathcal{F}}j = e^{-\gamma\bar{\sigma}} - 1 + \frac{\Delta\hat{V}}{\hat{V}_{\text{avg}}}\tau \tag{2.7}$$

where $\hat{V}_{\text{avg}} = \frac{\hat{V}_F + \hat{V}_0}{2}$, and $\tau = \frac{I}{Q}t$, the state of charge (SoC).[241] Note the relations $j = I/V_{\text{avg}}$ and $Q = nV_0\mathcal{F}/s\hat{V}_0$ were used. In addition, the total strain is also the casing strain, and by the definition $\varphi_C = C_C\sigma = \varphi$, the dimensionless stress and the porosity can be solved as [241]

$$\bar{\sigma} = \frac{\Delta\hat{V}}{\hat{V}_{\text{avg}}}\tau + \frac{1}{\gamma}\,\text{LambertW}\left(\gamma e^{-\frac{\Delta\hat{V}}{\hat{V}_{\text{avg}}}\tau\gamma+\gamma}\right) - 1 \tag{2.8}$$

$$\varepsilon(\bar{\sigma}) = \left[e^{\bar{\sigma}} + (1-\varepsilon^0)\gamma e^{\gamma-1}\text{Ei}\big(\gamma - 1 - \bar{\sigma}(1-\gamma)\big) + (1-\varepsilon^0)e^{-1}\text{Ei}(-\bar{\sigma}-1) + \varepsilon^0 - (1-\varepsilon^0)\gamma e^{\gamma-1}\text{Ei}(\gamma-1) - (1-\varepsilon^0)e^{-1}\text{Ei}(-1) - 1\right]e^{-\bar{\sigma}} \tag{2.9}$$

LambertW is Lambert W function and Ei denotes the first order exponential integral function as

$$\text{Ei}(x) = \int_x^\infty \frac{e^{-t}}{t}dt,\ x > 0 \tag{2.10}$$

To evaluate height changes h_1 and h_{buffer}, consider the estimated maximum volume change 26.4% of its original value in the active material layer (or 9.4% of buffer layer), based on the theoretical expansion rate of silicon (~ 400%) and graphite (~ 110%) as well as their percentage in electrode.[7] Therefore $\frac{\Delta\hat{V}}{\hat{V}_{\text{avg}}} \approx 0.23$ for the active material and $\left.\frac{\Delta\hat{V}}{\hat{V}_{\text{avg}}}\right|_b \approx 0.09$ for the buffer layer. The compressibility C_E and C_C can be estimated from elastic moduli of the active material, buffer, and the copper substrate. For the active material, we assume C_E =0.13 GPa^{-1}, for the buffer layer, C_{buffer}

= 0.19 GPa^{-1}, and C_{Cu} =0.04 GPa^{-1}. As for the casing, in the sample without buffer, the copper substrate is attached only on one of the six sides of the active material, we assume the effect is 1/6, thus makes C_{C1} = 0.24 GPa^{-1}. The ratio of compressibility γ_1 is then estimated as 0.54. On the other hand, in the sample with buffer layer, the active material has one side attached on the buffer, while the buffer has one side attached to the active material, and another side attached on the substrate. Assume that active material casing makes C_{Ca} = 1.14 GPa^{-1}, and buffer casing makes C_{Cb} = 1.02 GPa^{-1}, which therefore result in γ_a = 0.11 and γ_b = 0.19, respectively. Fig. 2 shows the simulation of evolutions of height strain ϵ_{h1}, ϵ_{ha}, and ϵ_{hb} from their volume strain during $0 \leq \tau \leq 1$, where the height change and height strain are given by

$$h = h_0(1+\varphi)^{1/3} = h_0(1+\epsilon_h) \tag{2.11}$$

$$\epsilon_h = (1+\varphi)^{1/3} - 1 \tag{2.12}$$

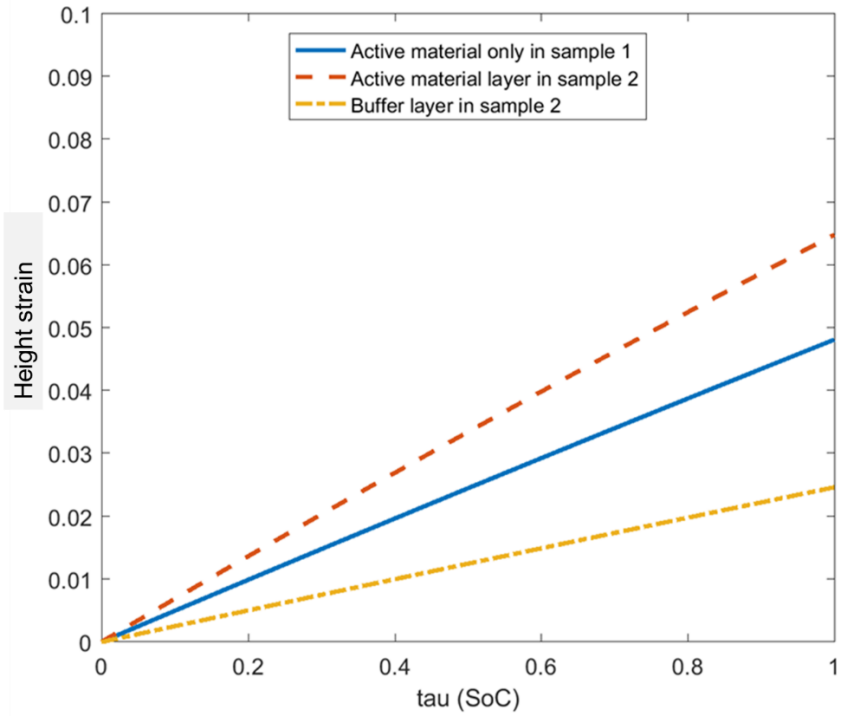

Figure 5.2 Simulation of evolutions of height strain ϵ_h1, ϵ_ha, and ϵ_hb during 0≤τ≤1.

The measurement of elastic modulus is based on the concept of nano-indentation using atomic force microscope (Bruker, NanoscopeV). It is noted that the AFM probe with spring

constant appropriately matching that of the sample should be selected to avoid inaccurate results. The thermal tune method was used to calibrate the spring constant of such AFM probes (Bruker TAP525A),[242] and the force versus indentation depth curves were fitted by the DMT model to yield elastic modulus using the Nanoscope Analysis software.[243] Since the electrode is a composite of silicon, graphite and PVDF polymer, the data of elastic modulus is divided into 3 distinct groups to represent each one. The elastic modulus of each kind of material were calculated as 142, 17 and 4 GPa for silicon, graphite and PVDF, respectively. These values correspond to previous published data well.[244-245] The known methods of mechanics of micro-inhomogeneous media do not allow us to describe the elastic properties of composites with an arbitrary content and strong distinction of elasticity moduli of components. The prediction of effective elasticity moduli of porous composite materials has been demonstrated previously by volume fraction of each component and the porosity of such composite materials.[246] The total elastic modulus of the silicon/graphite layer or the buffer layer could be calculated based on their volume fraction as 3.6% of silicon, 7.8% of PVDF and 88.6% of mesocarbon microbead (MCMB) graphite in upper layer and 7.6% of PVDF and 92.4% of MCMB graphite in the buffer layer. Furthermore, the porosity of 28.6% and 25.3% have been confirmed, based on the comparison of density between theoretical and actual value for materials in upper layer and buffer layer, respectively. So overall elastic modulus for these two layers could be calculated as 20.5 and 16.0 GPa, respectively. Moreover, the elastic modulus of copper thin film has been measured as around 75 GPa by previous study.[247]

5.2.3 Physical characterization, coin cell assembly and electrochemical measurements

To study the change of microscopic morphology and composition of the samples before and after experiments, scanning electron microscopy (SEM) were performed using a TESCAN GAIA instrument equipped with an Energy Dispersive Spectrometer (EDX). The samples with and without a buffer layer were used to assemble coin cells in order to further study their long-term cyclic performance. The coin cells were assembled in Ar filled glovebox based on the published protocol.[5] The cantilever-shaped anode was cut into proper size to fit into coin cells. Electrochemical cycles were performed galvanostatically with a cut-off voltage of 0.01-2 V using a MACCOR Model 4200 potentiostat. Different current rates were applied to detect the rate capacity of different electrode materials. Also, electrochemical impedance spectroscopy (EIS) and cyclic voltammetry (CV) were used to characterize the electrochemical characteristics of samples.[28]

5.3 Results and Discussion

The SEM and corresponding EDX were employed to illustrate the microstructure and element distribution of electrodes with and without a buffer layer (Fig. 3). From the top view of SEM images (Fig. 3a, d), bulk composite materials were shown. In the cross-sectional SEM images (Fig. 3b, e), the layered structure for original and modified electrodes were clearly illustrated. The upper and bottom layer for both samples were identical. The upper layer was composed of MCMB graphite, silicon particle, and PVDF with a thickness around 40 μm, and the bottom layer is thin film copper with a thickness around 20 μm. The buffer layer was delineated using yellow marks shown in Fig. 3e, of about 30 μm in thickness. The composition of this layer was MCMB graphite and PVDF binder. The EDX images further clarified this structure by showing that there was one middle buffer layer without any existence of silicon for the sample in Fig. 3f.

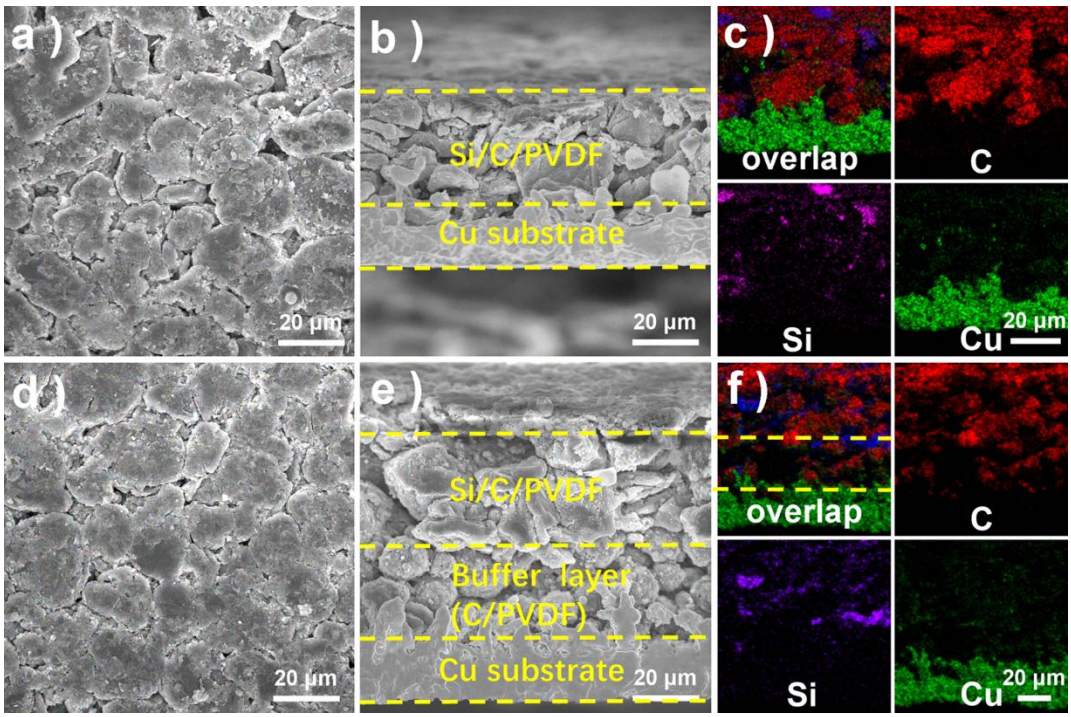

Figure 5.3 (a) Top view and (b) cross-sectional SEM images and (c) EDX mapping results of original sample without buffer layer; (d) top view and (b) cross-sectional SEM images and (c) EDX mapping results of modified sample with buffer layer.

Fig. 4a shows the potential-time profile of modified sample under nearly C/10 current rate in its 1st cycle. During the initial lithiation, the voltage dropped rapidly until a voltage plateau appeared below around 0.2 V. This was in good agreement with previous results of cyclic voltammetry of graphite. The profile indicates two distinct electrochemical processes before and after 0.2 V. Solid electrolyte interface (SEI) was formed on the surface of electrode in stage Ⅰ, and potential profile then reaches the plateau, indicating lithium ion insertion in stage Ⅱ.[248-249] The slight shoulder-like plateau in stage Ⅱ around 0.1 V obviously demonstrated a phase transition during lithium intercalation process. During the 1st delithiation, the plateau indicating lithium ion extraction was around 0.1-0.3 V in stageⅢ.[249] The voltage hysteresis between lithium insertion and extraction was observed due to IR-drop, caused by potential difference through resistance in the system.

The following short shoulder-like plateau in stage Ⅳ could be considered as an indication of Li-Si dealloy phase more than 400 mV. Fig. 4b displays typical CV curves of modified sample. Two anodic peaks around 0.2 and 0.1 V clearly corresponded to previously discussed formation of SEI and phase transition due to gradually increased lithium ion insertion. Also, the broad cathodic peak around 0.1-0.3 V reflected the plateau of delithiation, followed by a small peak around 500 mV being related to Li-Si dealloy phase.

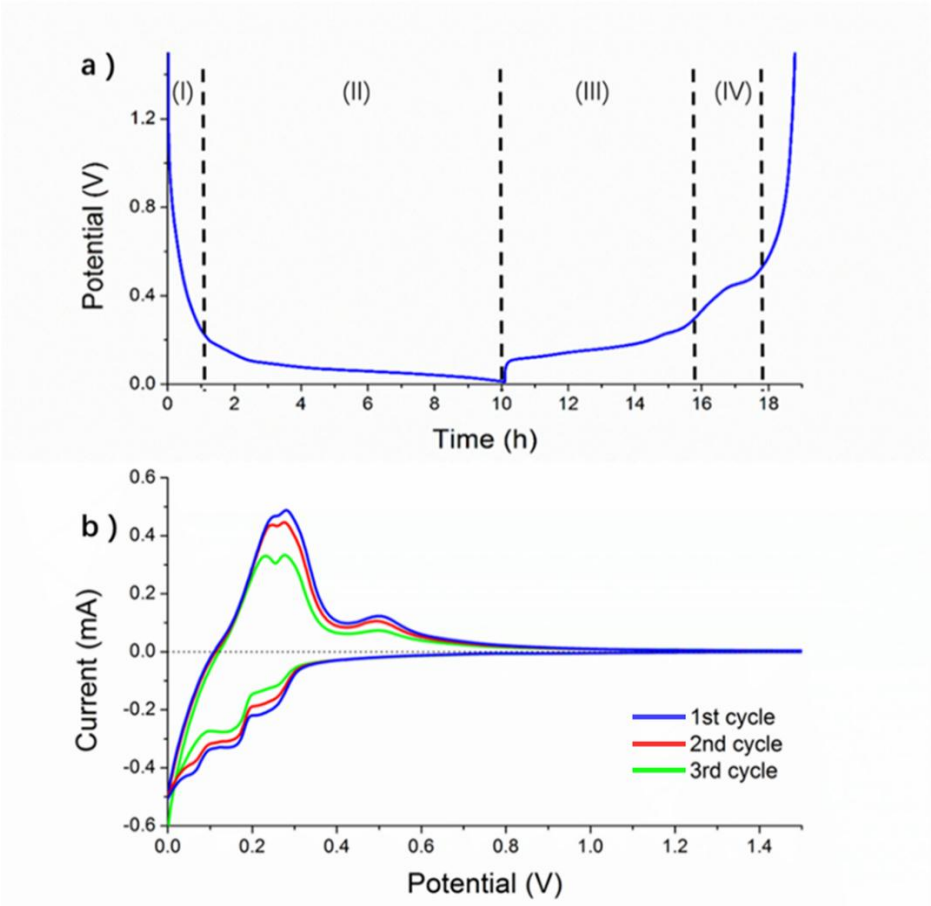

Figure 5.4 Electrochemical properties of modified sample: (a) voltage profile under C/10 in its first cycle and (b) CV curves at scanning rate of 20 mV s^{-1}.

Fig. 5 shows the in-situ deformation of cantilever-shaped electrodes during cycling. The experiments during 3 cycles of lithiation and delithiation were performed using a

constant current of 150 μA. Fig. 5a and b illustrated a potential shift with time associated with SEI formation and capacity degradation. Apparently, the sample with buffer layer showed a more stable cyclability than the other one, and this could be further validated in the corresponding deformation profile. Fig. 5c and d show how the strain of cantilever-shaped electrodes evolved during 3 cycles of lithiation and delithiation, in which both profiles showed a similar pattern for the discharging procedure with the maximum strain change of around -22.4% and -30.5% for the samples with and without buffer layer, respectively. In the first charging procedure, this two samples indicated a different recovery as delithiation takes place. The corresponding part of modified sample could fully recover to its original state, while the original sample still showed a residual strain more than -12%. For the rest cycles, the strain curve of modified sample basically followed the same pattern and extent of the first cycle. The original sample, however, did not indicate a well recovery during delithiation.

Fig. 5e and f show the deflection of the cantilever electrodes. Compared to the large deflection (~90 μm) for sample without buffer layer, the deflection for sample with buffer layer reached around 40 μm. Modified sample indicates similar curves for rest cycles, while original sample still exhibited a weak recovery. Obviously, the deflection profile showed a correspondent relationship to strain profile following the similar pattern. Based on this pair of mutually complementary profiles, modified sample demonstrated a better structural stability by showing smaller strain and deflection than original sample. Lower strain rate of modified sample could ensure that the mechanical dis-integrity would not hinder the activity of electrochemical reaction by avoiding cracking and obstructing of the diffusion channel of ions. Moreover, in difference to that the strain and deflection could recover to

their original position after electrochemical reaction for modified sample, the original sample indicates a much weaker resilience. This behavior could be attributed to permanent damage at the interface between active material layer and copper substrate induced by difference of mechanical deformation in each layer.[250]

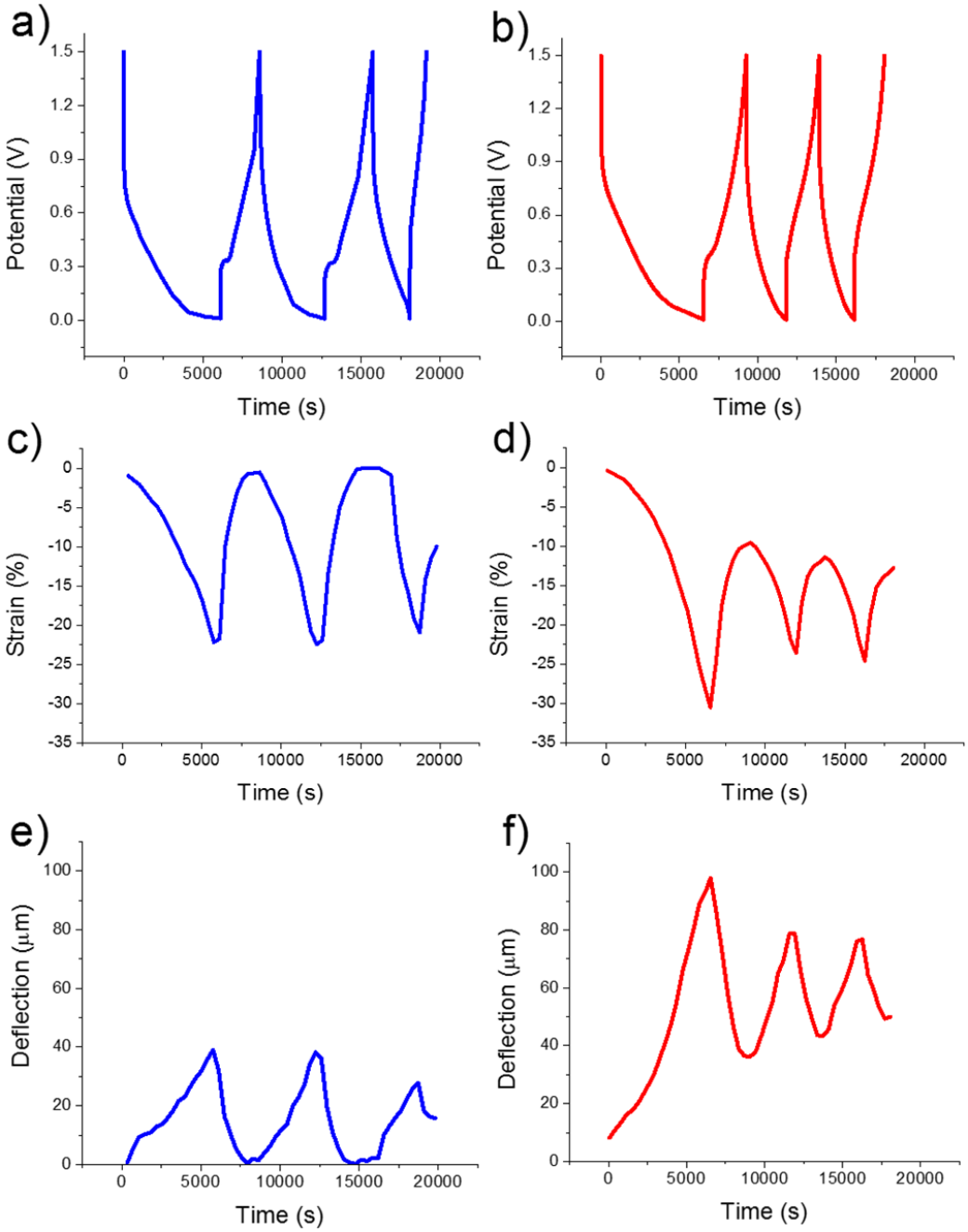

Figure 5.5 (a, b) Galvanostatic charge/discharge curves and in-situ (c, d) strain and (e, f) deflection measurements of modified (left-row) and original (right-row) samples under 150 μA.

Fig. 6a and b show the charge/discharge profiles of different cycles of the modified and original sample under C/10, respectively. In the first discharge step, both of them presented a long electrochemical plateau below 200 mV down to the cut-off voltage of 0.01 V, indicative of typical characteristics of potential for graphite or graphite composite material.[251] The discharge and charge capacities in 1st cycle were 840 and 725 mAh g^{-1} for modified and original sample, respectively. Compared to the theoretical capacity of graphite (372 mAh g^{-1}), the extra capacity of sample should be attributed to the mix of silicon which has a theoretical capacity of 4200 mAh g^{-1}.

In Fig. 6c, there was an obvious decrease of discharge capacity at 2nd cycle. This might result from active material loss induced by the SEI formation. From the 2nd cycle, the modified sample indicated a more stable and better battery performance than the original one. Although the magnitude of improvement by structural novel design was not substantial, the modified sample still showed a discharge capacity of around 750 mAh g^{-1} in its 20th cycle, compared to 650 mAh g^{-1} of the original one. This result indicated that 89.3% of battery capacity remains for modified electrode, demonstrating a significant improvement to 77.4% of original electrode. In Fig. 6d, it is shown that the coulombic efficiency rapidly rises from around 87% in the 1st cycle to 97.5% in the 2nd cycle for both samples. These two curves show a similar pattern of slightly increasing capacity from 2nd cycle to 5th one, followed by basically stable efficiency above 98% for rest cycles.

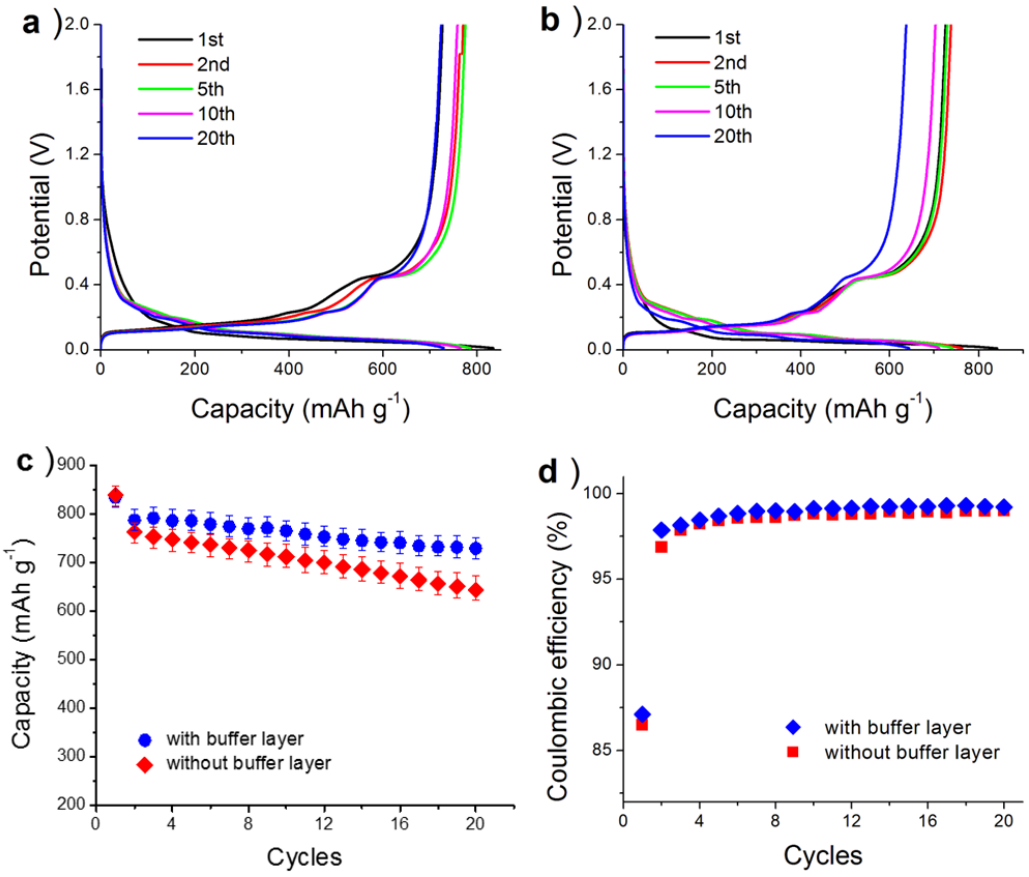

Figure 5.6 Galvanostatic charge/discharge voltage curves for (a) modified sample and (b) original sample, (c) galvanostatic cycling performance, and (d) coulombic efficiency curves of both samples.

In addition, the modified sample exhibited a better rate capacity under the working condition of varying current rate (from C/10 to C/5, C/2 and final 1C, and then gradually go back to its first rate) compared to the original sample. As Fig. 7 shows, the modified sample kept a capacity of 730 mAh g^{-1} after the first 10 cycles under the current rate of C/10, while the original sample only indicated a capacity of 660 mAh g^{-1}. For following cycles at various rate, the modified and original sample show 580 and 525 mAh g^{-1} for 20^{th} cycles at C/5, 250 and 100 mAh g^{-1} for 30^{th} cycles at C/2. This result indicated that only 11.8% of initial capacity has been maintained for original sample after 30 cycles, compared

to 28.1% for modified sample. When the current rate further increased to 1 C, it was observed that for both samples, the capacities are abnormally low, although the capacity of modified sample was relatively higher. This result indicates that with large thickness of electrode, usually tens of microns, one aspect needs to be considered: longer diffusion and migration paths for lithium ions to enter or leave an electrode. So, the transport of lithium ion could not keep up the pace with charge transfer under conditions with a large current rate.[252] Furthermore, when the rates started to return from C/2 to C/5 and final C/10 after 40 cycles, the original sample showed a weaker recovery than the modified one. They showed 500 and 360 mAh g^{-1} for the 60th cycle at C/5, and 540 and 460 mAh g^{-1} for the 70th cycle at C/10. Compared to previously corresponding lower C rate, the difference of capacity for these two samples become larger for C/10 and C/5.

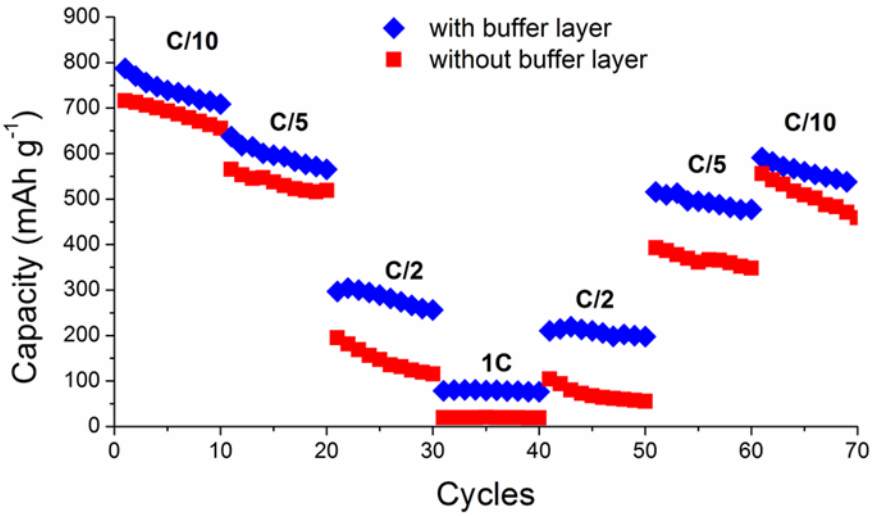

Figure 5.7 Comparison of capabilities recorded at different C-rates.

In order to ascertain the buffering action of modified structure, the interfacial resistance of the two sample was monitored with EIS. Fig. 8a shows the impedance results obtained before and after charging/discharging cycles for modified and original samples.

Both samples exhibit similar EIS performances, indicative of a depressed semicircle at the high-middle frequency and a linear Warburg slope at the lower frequency.[253] The semi-circles were related to processes of electron transfer and the later linear slopes reflect the resistance of ion diffusion. The results show that the electrical impedance of the cell using modified sample as electrode is similar to that of the original sample before cycles. While after cycles, it was obvious that the charge transport was hugely hindered for the sample without buffer layer. On the contrast, the impedance of the cell with mechanical buffer addition barely showed any significant change. The interfaces between battery materials and copper with and without a buffer layer after cycling were shown by SEM images in Fig. 8b and c. With a buffer layer, the electrode was adhered well to the current collectors after cycling. Without a buffer layer, the delamination of the electrode from the copper substrate was clearly shown.

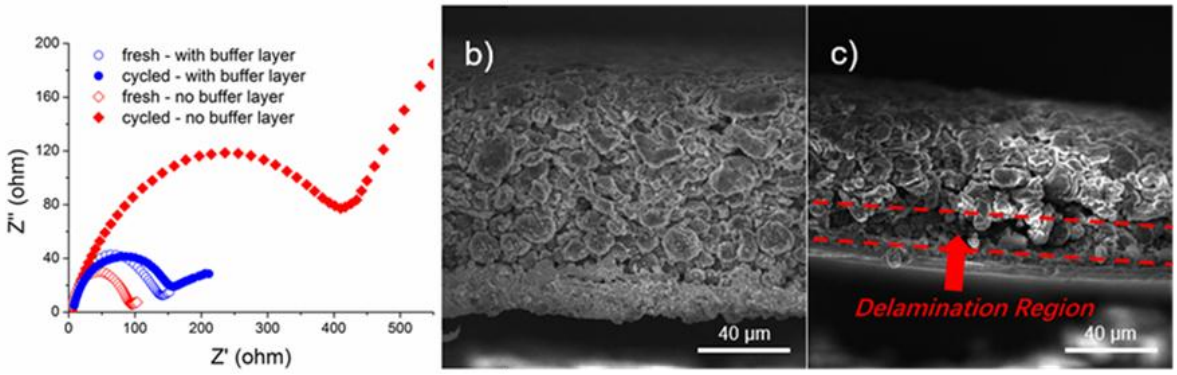

Figure 5.8 (a) EIS Nyquist plots of both samples before and after charging/discharging cycles and (b, c) SEM images showing the cross-sectional area of both samples after cycles.

Fig. 5 shows that the sample with buffer layer has a better mechanical stability than the original sample. In terms of the role of mechanical buffer film, it is proved that this ductile layer, having an intermediate volume expansion, which would therefore effectively alleviate the strain mismatch between the active material film and copper substrate, and

then relieve the crack propagation and following delamination. Coin cell results shown in Fig. 6 further reveal that due to the presence of buffer layer, a better mechanical stability could enhance the battery performance.[254] Since buffer layer could clearly decrease the delamination effect caused by significant difference between graphite/silicon layer and copper substrate, electrical connection and lithium ion diffusion are less affected. Also, severe silicon particle pulverization caused by drastic volume change during electrochemical cycles could be one of the main reasons that results in the electrically-disconnected smaller particles, thus degraded battery capacity and poorer performance.[255-257] The reason why sample without buffer layer demonstrates a weaker capacity resilience (shown in Fig. 7) and a greater internal impedance (see Fig. 8) increase rate after cycles could be also attributed to this mechanical effect. After a long 40 cycles of experiment, there could be possible void and crack sites emerge at the interface between film and substrate, causing disconnected diffusion pathway and worse electron transport.[258] In contrast, the modified design of adding buffer layer could be greatly avoid such unfavorable influences. In short, the deformation and stress evolution data as well as the coin cell results, obtained from sample with and without buffer layer, clearly indicate that this novel structure design of electrodes could alleviate the mechanical damage and delamination between different layers and then improve battery performance.[259-261]

5.4 Conclusion

A novel strategy of inserting a buffer layer between an active material layer and a current collector copper layer was developed in the current study for the fabrication of advanced anodes of LIB. The buffer layer, which has an intermediate volume expansion/shrink rate, is expected to release the stress and mitigate the mismatch at the

interface between the active material and the copper substrate. Therefore, such a modified structural design is capable of effectively utilizing the mechanical flexibility to reduce the maximum strain on the electrode surface by 40% and the cantilever electrode deflection by around 60 μm. As a result, the electrode with this modified structure exhibits a relatively larger reversible capacity (~730 mAh g^{-1} after 20 cycles), more excellent cyclic performance and better capacity recovery after applying various current rates, highlighting the advantages of adding the buffer layer for more effectively maintaining the mechanical and structural stability and improving battery performance for energy devices, especially for those with large volume expansions. This introduction of the modified electrode design with a mechanical buffer could potentially be employed for industrial scale manufacture of high-capacity batteries for EV/HEV.

6 CHAPTER 6 TRANSITION METAL ACETATE AS EFFECTIVE AGENT FOR PASSIVATION OF LITHIUM ANODE IN LITHIUM SULFUR BATTERIES

6.1 Introduction

The increasing need of energy storage devices with higher energy and power density for electric vehicles (EV) and portable electronics is challenging the current state of lithium ion batteries.[133, 262] It is noted that Li-S battery has long been considered as one of the most promising beyond lithium ion energy conversion and storage systems, due to its large theoretical energy density ~2700 Wh kg^{-1}, non-toxicity and cost-effectiveness.[18, 135] Nonetheless, there are significant technical hindrances that limit the practical and widespread application of lithium sulfur batteries, such as poor cycling stability, high self-discharge, loss of active materials, and safety issues caused by thermal runaway and short circuit.[263] The capacity fading over cycles could be attributed to low conductivity of sulfur, shuttling mechanism of soluble polysulfides, loss of active material, and degradation of lithium metal electrode.[18, 135, 137, 146-147] Numerous studies have been made recently on the design and fabrication of sulfur cathodes to alleviate the capacity fading. The composites of sulfur with carbon materials, conductive polymers, or metal oxides/nitrides/chalcogenides are widely developed and used as cathodes.[32, 75, 139, 149-150, 159-160, 162-163] The structural design is usually aimed to trap the sulfur inside of the nanostructure, which is acting as a polysulfide reservoir and providing a more conductive

pathway. This could lead to the enhancement of utilization of active materials and improvement of electrochemical performance and cycling stability.[18, 145, 160]

Though most efforts focusing on designing effective cathode structure hosting sulfur, protection of lithium anode is important for overall cycling stability.[264] Although the theoretical specific capacity of lithium metal in anode is as high as ~3860 mAh g^{-1}, it suffers from dendritic growth, solid electrolyte interface (SEI) film with poor stability, and a limited understanding of surface chemistry on cycling efficiency.[53] The growth of lithium dendrites on the lithium metal surface in secondary batteries could be ascribed to inhomogeneous deposition and dissolution of lithium ions during cycles as a result of uneven surface morphology and structure of metallic lithium anode.[265-266] As lithium dendrites inevitably form and grow, they would intrinsically lead to the punctuation of separator, causing short circuit and safety issues of lithium batteries.[267-269] Moreover, an unstable SEI film which collapses and reconstructs over cycles leads to the continual consumption of lithium metal and electrolyte, resulting in poor Coulombic efficiency and electrochemical performance.[268] On the other hand, the electrochemistry of lithium sulfur batteries leads to more complications for lithium metal anodes.[270] The parasite reactions between metallic lithium and soluble polysulfides generate self-discharge and precipitation of insoluble polysulfides, associated with severe loss of active material.[271-273] The deposited, insulating sulfides can hardly be re-utilized, leading to a rapid decay of capacity.[274] Thus, attempts were made previously to achieve the surface passivation of lithium metal with polymer coatings.[270, 275] The results are mixed due to the inadequate control of the thickness and chemical composition of pre-passivated layer.[270] By utilizing a sputtered solid film of electrolytes, the continual electrolyte decomposition on anode

surface was greatly minimized.[125, 276] However, the issue of high cell overpotential also emerges as a result of the large thickness and low ionic conductivity of the sputtered film. Furthermore, self-anchored carbon spheres were used recently to serve as flexible and strong framework for lithium metal anodes.[277] The deposition and dissolution of lithium ions would be spatially confined within the interior space of carbon spheres without random extrusion. Unfortunately, the method suffers from its incapability of large-scale industrial manufacture and also lower volumetric energy density due to its mass increase.[277]

Electrolyte additives were used as another possible approach to protect lithium anodes of Li-S batteries.[57, 278-280] To restrain the migration of polysulfide in lithium sulfur batteries, especially with higher content of sulfur, $LiNO_3$ was widely used as electrolyte additive.[57] Due to the reduction to Li_xNO_y by lithium metal from $LiNO_3$ and the oxidation of polysulfides to lithium sulfates, the undesired side reactions between polysulfides and lithium metal could be greatly alleviated.[281-282] However, the consumption of $LiNO_3$ is very fast due to the continual formation and collapse of passivation films, and growth of lithium dendrites during charging/discharging cycles.[283] Thus, the effectiveness of $LiNO_3$ in protecting and stabilizing lithium metal anode is questionable, particularly in long-term cycles. Therefore, a more efficient electrolyte additive strategies to form a more robust passivation layer on the lithium anode surface is needed.

Zu et al. developed the facile method of using copper acetate in electrolyte as lithium metal stabilizer in polysulfide-rich environment.[284] The copper sulfide formed assisted the formation of a film with better physical and chemical characteristics,[284] which helps to promote the homogeneity and mechanical strength of passivation layer on lithium anode surface. With less active sites for lithium deposition and stronger suppression to dendritic

growth, the passivation film is able to remain its surface morphology and structure in long-term cycles.[284] The generation of more robust passivation film was believed to be the result of active control of lithium deposition sites.[285] The existence of copper cations and polysulfides undermines the long-range order of crystalline lithium sulfide, attracting lithium ions deposited associated with the deposition of copper sulfide.[284] This spatial arrangement results from the different ionic radius and molecular interaction between transition metal sulfide and lithium sulfide. Based on this consideration, other transition metal cations would also have similar but varying effect on passivating the lithium metal anode surface. Thus, we here provide a detailed and informative comparison between different transition metal (Ni, Co, Mn, Zn) to discover the possibility of achieving the best results.

6.2 Experimental

6.2.1 Fabrication of electrodes and cell assembly

The electrode slurry was prepared by incorporating sulfur with conductive additive (nanostructured titanium nitride) with a wt. ratio of 65:35 by melt-diffusion method. Details of nanostructured titanium nitride synthesis have been described elsewhere.[194] The mixture was first heat above the melting temperature of sulfur around 115 °C and maintained for 30 minutes. 10 wt% of poly(acrylonitrile-methyl methacrylate) AN/MMA (94:6, Polysciences Inc) was added as binder and N-methyl pyrrolidinone (NMP, xxxx) as solvent to the slurry. The slurry was then coated on Al foil and dried at 80 °C under vacuum for 10 h to form the S cathode.

1,3-Dioxalane, 1,2-Dimethoxyethane, LiTFSI, $LiNO_3$ (add the acetates) were purchased from Aldrich and used as received. An electrolyte with 1 M of 1,3-Dioxalane, 1

M of 1,2-Dimethoxyethane, 1 M LiTFSI, 2 wt% $LiNO_3$ and 0.03 M transition metal acetate (with Zn, Cu, Ni, Co, Mn cations) was prepared by stirring at 80 °C for 6 h. 8 μL of electrolyte solution was added onto S cathode. In addition, a Polypropylene separator (Celgard 2400), and lithium foil anode were used to assemble coin cells (CR2032) inside an argon filled glove box.

6.2.2 Material characterization and electrochemical measurements

Morphological features of the cathode materials were observed with scanning electron microscopy (TESCAN, model S9000). Galvanostatic discharge-charge tests were conducted using a Maccor Model 4200 Automated Test System between the voltage range of 1.6 to 3 V (vs. Li/Li+) at room temperature. Electrochemical Impedance Spectroscopy (EIS) and cyclic voltammetry (CV) experiments were performed using a Gamry potentiostat reference 3000. The scan rate was 0.5 mV s^{-1}. The minimum amplitude of AC voltage was 0.1 mV. The frequency was swept from 0.1 Hz to 100 kHz.

6.2.3 Mass change by electrochemical quartz crystal microbalance (eQCM)

The measurements of mass change of lithium metal anode over cycles were undertaken using an eQCM (Gamry 10M) and a Gamry potentiostat at room temperature. QCM crystals were formed from planar, 2.54 cm diameter AT-cut 5 M Hz quartz crystals coated on one side with Au. Prior to use, the Au crystal was ultra-sonicated in deionized water for 10 min and rinsed with isopropyl alcohol. A piece of lithium metal (0.3−0.5 mg) was then pressed onto to the Au QCM crystal.[286] The EQCM cell was assembled in an Ar-filled glovebox prior to in situ EQCM measurements as described previously.[287-288]

6.3 Results

A series of transition metal cations (Zn, Cu, Co, Ni, and Mn) acetate additives were utilized in cells at 0.2 C, in which the cathode consists of carbon nanofibers, polymer binder and sulfur as described earlier in the experiment section. The cycling performance (100 cycles) and stability decreases as the atomic number of transition metal elements decreases (Figure 1a). Cycling stability of 500 cycles of the lithium sulfur batteries with selected transition metal cations (Zn and Cu) additives was further studied by galvanostatic charge/discharge at 0.1 C (Fig. 1b). The initial capacity are 1590, 1560, and 1510 mAh g^{-1}, and capacity retention after 500 cycles are 70.1, 63.4, and 57.5%, for samples with Zn, Cu, and no additives, respectively. Moreover, Fig. 1c shows Coulombic efficiency (CE) of the samples with Zn, Cu, and no additives indicating the effectiveness of protective SEI on lithium metal anode with electrolyte additives. During charging/discharging cycles, the CE of the sample without any electrolyte additives indicates a lower efficiency below 96%. On the other hand, a remarkably higher CE were observed for the cells with zinc and copper cations added (>99% and >97%), which could be ascribed to the effective formation of more stable SEI film with less dendritic growth over lithium metal surface. The enhanced electrochemical performance and stability improves with increasing atomic number, which can be attributed to the better interruption of large coverage of lithium sulfide coating and smoother SEI film morphology.

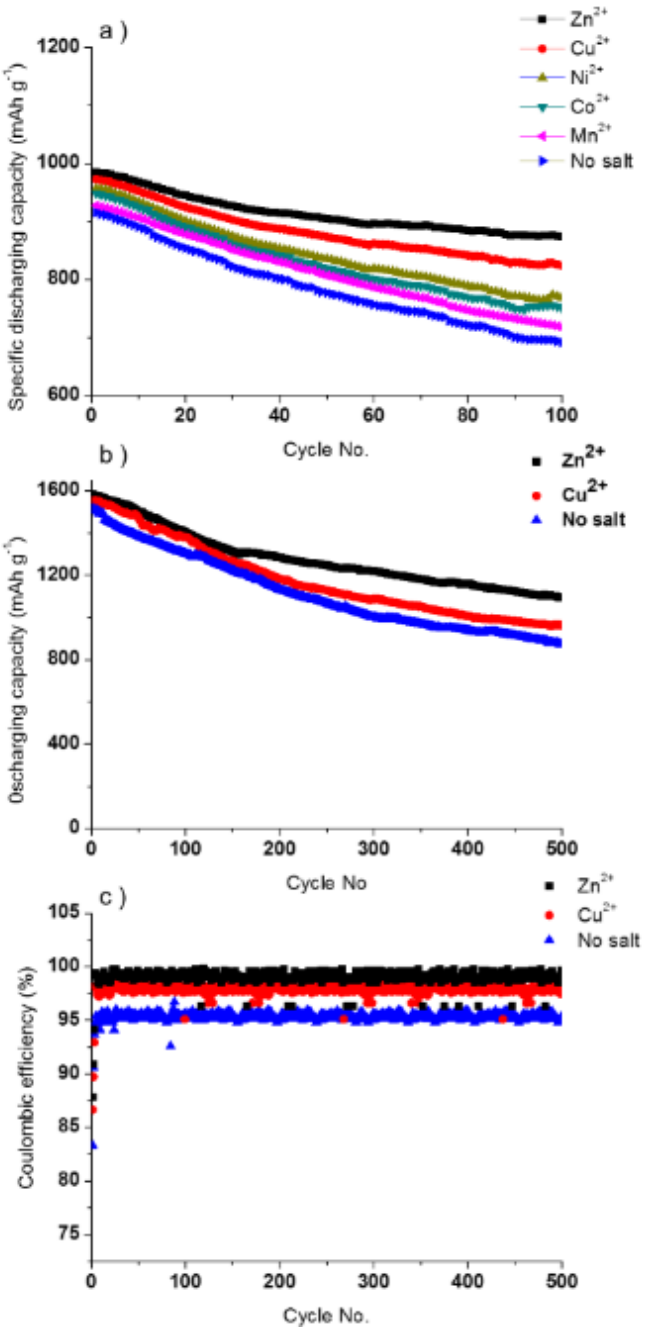

Figure 6.1 (a) Cycling performance of transition metal cations and no salt cells at 0.2 C for 100 cycles, (b) Cycling performance and (c) Coulombic efficiency of Zn, Cu, and no salt cells at 0.1 C for 500 cycles.

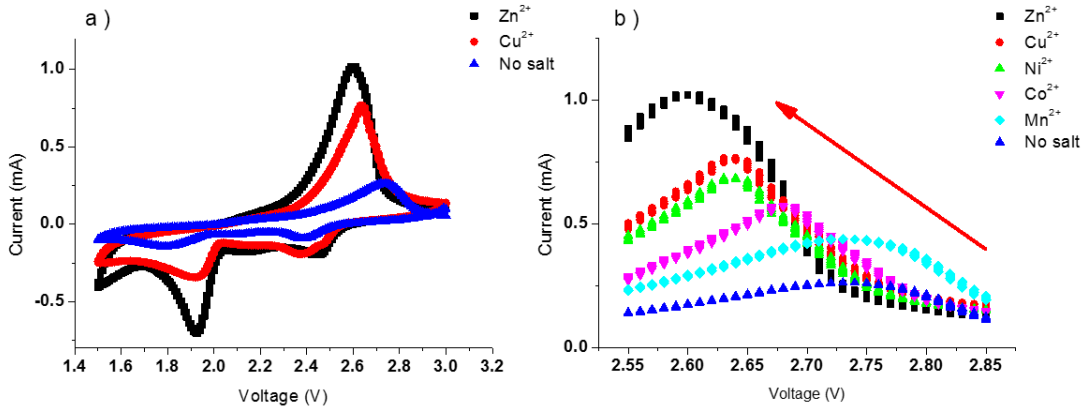

Figure 6.2 Cyclic voltammetry curves of cells with transition metal cation additives.

Fig. 2a shows cyclic voltammetry (CV) curves of samples with Zn, Cu, and no additives were performed to evaluate the reactivity of the redox reactions at a scan rate of 1 mV s^{-1} over the range of 1.5 V – 3 V. The CV curves show two characteristic cathodic peaks and one anodic peak for all samples.[135] The cathodic peaks around 2.3-2.5 V and 1.9-2.0 V represent the reduction of elemental sulfur to soluble long-chain polysulfides and from soluble polysulfides to insoluble ones, respectively.[289] The anodic peak around 2.6-2.75 V during oxidation represents the oxidation of lithium sulfide to polysulfide and then elemental sulfur.[289] The currents for cathodic and anodic peaks are -0.74 and 1.02, -0.36 and 0.79, -0.13 and 0.26 mA for Zn, Cu, and no salt additives. The cells with Zn and Cu cations show much high peak currents, suggesting a higher electrochemical reaction kinetics.[290] In addition, the shift of reduction current peaks to a higher voltage (data not shown, or S Fig) and of oxidation current peak to a lower voltage (Fig. 2b) correlate with the atomic number of the transition metal cations cells. The results suggest that transition metal cations with larger atomic numbers resulted in a bigger shift of the oxidation and reduction peak, indicate a better reversibility of the redox reaction which corresponds to better electrochemical performance and Coulombic efficiencies.

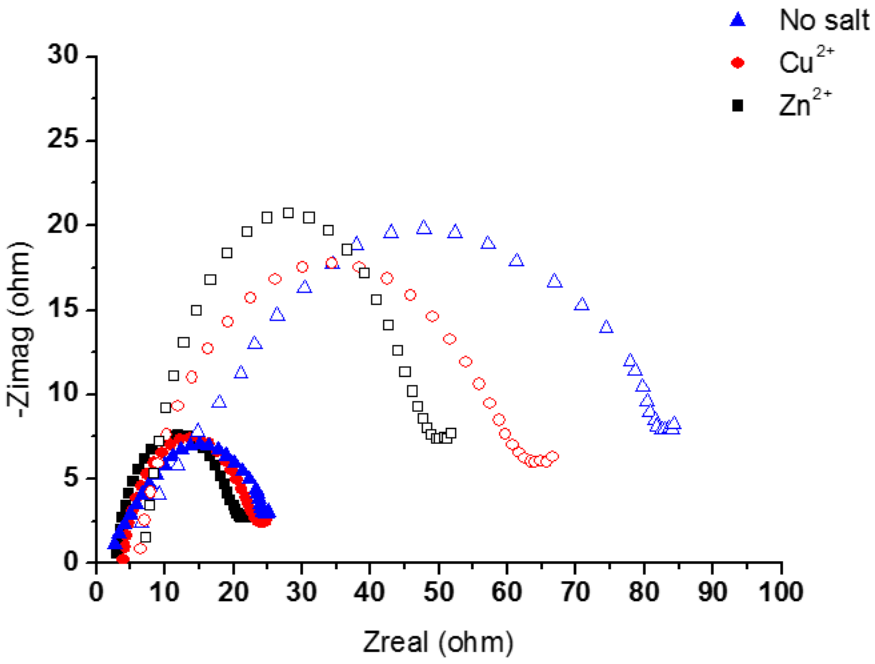

Figure 6.3 EIS spectra of cells with modified/unmodified electrolyte before and after 500 cycles.

Fig.3 shows the electrochemical impedance spectroscopy (EIS) spectra of Zn, Cu, and no salt samples initially and after 500 cycles. At initial cycles, the resistance of control cell with no salt (22.5 ohm) was slightly higher than that of cells with zinc acetate (17 ohm) or copper acetate added (20 ohm). After long-term cycling, the resistances indicate significant increase among all cells. The cell with no salt shows the largest charge transfer impedance of 78 ohm (246.7% increase), while the cells with zinc and copper cations exhibit 47.5 (178% increase) and 61 (205% increase) ohm, respectively. The lower charge transfer impedance of Zn and Cu cations samples after 500 cycles allow enhanced electron transfer ability and contribute to the better battery performance and higher capacity retention over cycles.

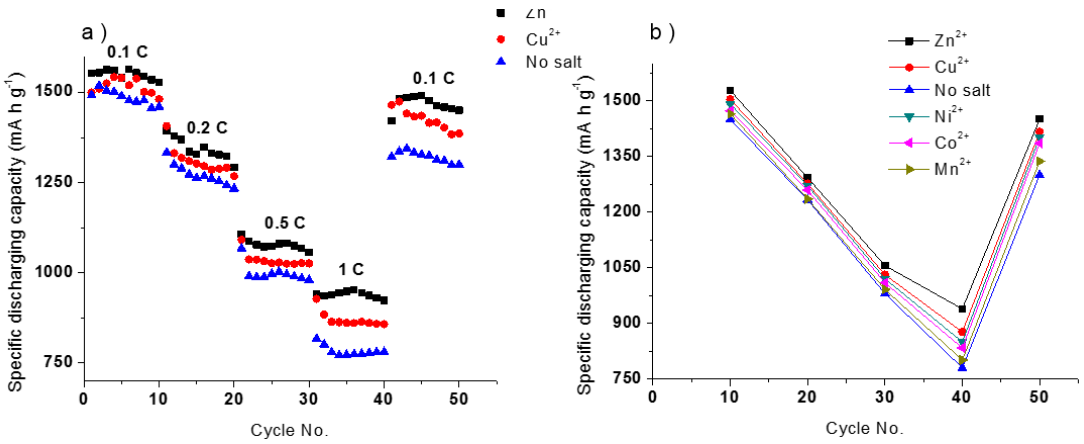

Figure 6.4 Rate capability measurements of cells with modified/unmodified electrolyte.

As shown in Fig. 4a, the rate capability was measured for the cells at various C-rates of 0.1 C, 0.2 C, 0.5 C, 1 C for 10 cycles each. The cell with zinc cation added was able to deliver the best discharging capacities of 1527, 1293, 942, and 918 mAh g^{-1} at 10^{th}, 20^{th}, 30^{th}, and 40^{th} cycle, respectively. On the contrary, the cell with copper cation added showed lower discharging capacities, although the capacities are still higher than that of cell with no salt, which exhibited lowest capacities and poorest battery stability under various current rates. Additionally, a remarkable discharging capacity of 1450 mAh g^{-1} (94.9% of 10th cycle) was recovered at 50^{th} cycle as the C-rates was decreased back to 0.1 C. For Cu and no salt sample, only 91.2 and 87.8 % of 10th cycle capacity were recovered at 50^{th} cycle, respectively. Apparently, the findings demonstrate that the cells with Zn and Cu cations additive are more resilient under high and varied charging/discharging current rates. In Fig. 4b, it is indicated that the descending order of rate capability corresponds with the atomic number of transition metal additives, which also follow the same trend of the long-term cycling performance.

Fig. 5 shows the mass change of Zn, Cu, and no salt samples measure by EQCM over 25 cycles. The mass changes (Δm) were measured based on the change of the resonant

frequency (Δf) of the quartz crystal attached to a lithium metal foil. The mass change of the electrode can be attributed to the chemical (electrolyte decomposition products, and parasitic byproducts) and electrochemical reactions (SEI film formation, lithium stripping and plating, and corrosion). Hence, $-\Delta f = C_f \Delta m$ where C_f is a constant which depends on specific characteristics of the quartz crystal used. It is observed that an increase of mass of lithium metal anode as a function of cycles for the Zn, Cu, and no salt cells. For the first 5 cycles, the cells with zinc and Cu additives indicate a larger mass change over the cell with no salt, which can be attributed to a faster deposition kinetics onto lithium anode surface and larger atomic weight (as compare to Li). However, the increasing rate of mass change of the no salt sample obviously outpaced the cells with Zn and Cu additives. This can be attributed to the fact that Zn or Cu sulfides collaborating with LiS to create a more uniform and dense passivation layer on Li anode surfaces. This will minimize lithium plating and dendrite growth, and subsequently lower surface area and fewer active sites resulting in lower mass accumulation. In fact, after 25 cycles, the cell with zinc additive showed the most stable performance with the least mass change around 1.9 mg, as compared to the cell with copper additive (~2.7 mg) and the no salt sample (~3.3 mg).

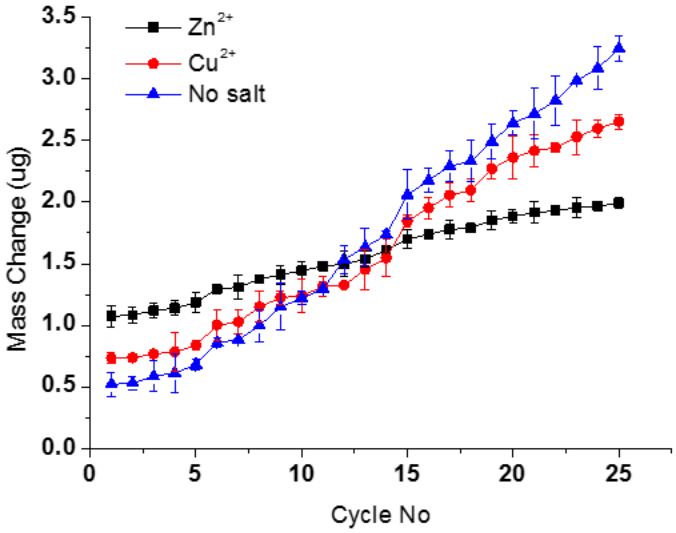

Figure 6.5 Mass change measurements of Li metal anodes in cells with modified/unmodified electrolyte.

Figure 6 shows SEM and EDS images of Li metal anodes with and without Zn acetate additive after 1 and 100 charging/discharging cycles. After the first cycle, the lithium surface without Zn additive showed nonuniform precipitates (Fig. 6a), which attributed to plated mossy-structure byproduct as the result of lithium metal reacting with electrolyte and $LiNO_3$.[281-282] This demonstrates the inadequate effectiveness of $LiNO_3$ to form and preserve a stable passivation layer on the lithium anode in an electrolyte environment with polysulfides. On the other hand, very few plated mossy-structure byproduct was observed on the lithium metal surface with Zinc cation additive (Fig. 6b). After the 100th cycle, the surface morphology of the sample without Zn additive exhibited a rougher morphology with buildup of particles and flakes byproducts. While the lithium surface in cell with Zn additive present a considerably smooth morphology with less but more uniform byproduct precipitation. The height profile of Fig. 6e indicated a smoother surface compared with Fig. 6a which can be ascribed to a collaborative effect between ZnS and LiS to form a more

homogeneous passivation layer. The inset of Fig. 6a-d clearly reveal the amount of sulfur precipitated on the surface of Zn additive lithium metal anodes is significantly smaller than without Zn additive after 100 cycles. Atomic % of sulfur increases from 13.4 to 29.3 and from 15.3 to 18.7 for no salt and Zn cation added samples, respectively. Similarly, smaller amount of sulfur precipitated on Cu additive lithium metal anode was observed after 100 cycles (images not shown). These findings are in good agreement with the trend of mass accumulation as described in Figure 5. The results further support the assistive protection effect of transition metal additive (Zn^{2+}) to minimize precipitation of sulfides and decomposition products.

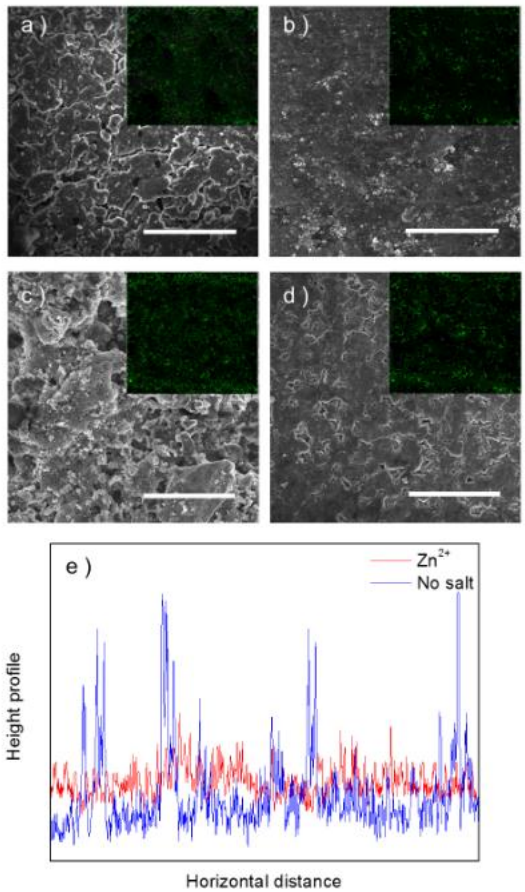

Figure 6.6 SEM images of Li metal anodes after 1 and 100 cycles in cells with unmodified electrolyte (a, c) and cells with zinc additive (b, d). The insets show EDX

mapping of sulfur element in each figures. The scale bar is 50 mm in length. (e) Height profile.

6.4 Conclusion

In summary, a facile method of protecting lithium metal anode is successfully proposed through introducing an in-situ formed passivation film. The transition metal cation additives efficiently improve the morphology, structure, and stability of SEI film over cycles. This strengthened passivation film not only beneficially controls the lithium plating sites to suppress the growth of lithium dendrite, but also serve as an effective barrier to block the contact between lithium metal with electrolyte. Furthermore, the generated protective layer, assisted by transition metal sulfide incorporated, also hinders the diffusion of polysulfide to lithium metal, which further alleviates the undesired electrochemical and chemical reaction with loss of active material and self-discharge. Outstanding battery stability, better redox kinetics and lower resistance over cycles are observed due to stable and smooth SEI film on lithium surface with fewer dendritic morphology and less accumulated insulating and uneven particles. It can be concluded that this simple application of cost-effective and ecofriendly transition metal acetate as electrolyte additive could be utilized as a promising strategy for industrial application of lithium sulfur batteries.

7 CHAPTER 7 CONCLUSION AND FUTURE WORK

7.1 Conclusion

Novel and highly structured materials have been pursued as sulfur-hosting materials to enhance the specific capacity and cycling stability of lithium-sulfur (Li-S) batteries. Herein, structured titanium nitride nanotubes with tunable dimensions are investigated for their performance on Li-S batteries. We firstly develop a facile method to synthesize TiN nanotubes through anodization of Ti foils and nitridation. Surface morphology and BET surface area are characterized. The change of interfacial resistance, electrochemical performance and stability of batteries are evaluated as a function of nanotube length and diameter. The best electrochemical performance in Li-S batteries observed is for the 30 μm long and 65 nm diameter TiN nanotubes, which has a high discharge capacity of 1338 mAh g^{-1} after 180 cycles at 0.1 C, and with only 0.064% average capacity decay per cycle. Furthermore, increase in nanotube length from 4.5 to 30 μm and decrease in nanotube diameter from 100 to 35 nm of titanium nitride enhance capacity by 19.1% and 24.7% after 180 discharge/charge cycles, respectively. This study suggests nano-structure with tunable geometry can play a significant role in battery performance and cyclability, and that TiN nanotubes could serve as a very promising cathode material for advanced Li-S batteries.

Nanostrucutred titanium nitride (TiN) and graphene composite electrodes have been fabricated through a facile ultrasonication method combined with melt-diffusion of elemental sulfur. Nanostructured TiN particles and tube arrays integrated with graphene

substrate lead to the formation of a porous structure with enhanced electrical conductivity and stabilized integrated structure. Such a framework may facilitate accessibility of electrolyte and fast transfer of charges. The specific capacities of the Li-S batteries with TiN nanotube/ and nanoparticles/ graphene composites are 1229 and 1085 mAh g-1 after 180 cycles under 0.1 C rate, respectively, which are significant better than pure TiN nanostructures. The specific capacity and capacity retention were investigated as a function of TiN nanotubes to graphene ratio. The optimal ratio was found to be 1:1 TiN/Graphene, with the highest capacity retention of 87.5% after 180 cycles. This optimal 3D hybrid structure may provide a balance of high specific capacity and electrochemical stability, allowing durable and efficient energy storage and conversion over long cycles.

To further address the issue of volume expansion and mechanical crack of electrodes as well as expand the area of research to satisfy more practical applications, silicon containing thick anode electrodes were investigated to provide a higher energy density and capacity for EV/HEV applications. In our study, a facile technique of adding a mechanical buffer between thick active material and current collector is proposed and tested by an in-situ measurement using white light interferometry. The electrodes with a modified structure deliver a significant improvement to mechanical stability as well as battery performance compared to conventional electrodes with the original structural design. Therefore, the methodology demonstrated here can probably be used to mitigate the deteriorating effect of mechanical failure in silicon-based electrodes, in which volume variation is usually considered as a severe issue, of lithium batteries.

The lithium metal anode in lithium sulfur batteries can be effectively protected with the application of transition metal acetate as electrolyte additive. The use of transition metal

cations greatly improved the nature of SEI film, making it possible to suppressing further degradation of lithium metal. The transition metal sulfide deposited on lithium surface effectively stabilize the passivation film by cooperating with lithium sulfide and electrolyte decomposition product and improving the smoothness and robustness of SEI film. The enhanced homogeneity of passivation layer greatly hinders the parasitic reaction between lithium metal and polysulfides as well as organic electrolyte, reducing the loss of active material and mitigating the poor Coulombic efficiency. On the other hand, the uniform and mechanically strong SEI film introduces less undesired lithium plating and further accumulation on active sites, which significantly suppresses the dendritic formation due to improved surface morphology and chemistry. Consequently, the findings provide a facile method of in-situ chemical formation of passivation layer protecting the lithium metal in batteries.

7.2 Future work

The issues with regard to cathode framework design, electrode structural modification and lithium metal anode protection has been deliberately discussed and solved to a degree. The next direction of lithium sulfur batteries to be practically applicable in industrial manufacture is to eradicate the negative effect of shuttling mechanism, enhance the stability and safety of batteries over cycles, and lower the cost. As a long term research objective, solid state electrolyte has been considered as a promising candidate with capability of solving all forementioned issues. Gel, ceramics, solid polymer, and their composite have already been initiated as fundamental approaches. Firstly, the utilization of solid-state electrolyte could greatly suppress uneven lithium plating and following growth of lithium dendrites. Thus, it could contribute a lot to enhance the overall safety

and stability of batteries in long term cycling. It is noted that this specific characteristic is not limited to the application of lithium sulfur batteries, but to the wide use of all lithium metal batteries, which is also considered as a valuable development direction of energy storage systems. On the other hand, the solid-state electrolyte could serve as a selective membrane to further inhibit the migration of soluble polysulfides and improve the overall battery performance. Unfortunately, the use of solid-state electrolyte is currently limited by its shortcomings, such as high interfacial impedance and low ionic conductivity. Corresponding novel design within interface and electrolyte material with less resistance to lithium ion diffusion is in great need, leading to an effective method of achieving a high-performance solid−state lithium sulfur battery.

REFERENCES

1. Halimah, P. N.; Santosa, S. P.; Jusuf, A.; Dirgantara, T., The Concept of Sandwich Panel Structures for Battery Protections in Electric Vehicles Subjected to Ground Impact. *2018 5th International Conference on Electric Vehicular Technology (Icevt)* **2018**, 142-146.
2. Fu, K.; Gong, Y. H.; Dai, J. Q.; Gong, A.; Han, X. G.; Yao, Y. G.; Wang, C. W.; Wang, Y. B.; Chen, Y. N.; Yan, C. Y.; Li, Y. J.; Wachsman, E. D.; Hu, L. B., Flexible, solid-state, ion-conducting membrane with 3D garnet nanofiber networks for lithium batteries. *P Natl Acad Sci USA* **2016,** *113* (26), 7094-7099.
3. Guo, J.; Zhang, M. G.; Yan, S. J.; Yan, X. Y.; Wei, S. W., Electrochemical properties of modified acetylene black/sulfur composite cathode material for lithium/sulfur batteries. *Ionics* **2018,** *24* (8), 2219-2225.
4. Huggins, R. A., Primary, Nonrechargeable Batteries. *Energy Storage* **2010**, 355-366.
5. Lee, Y. M.; Seo, J. E.; Lee, Y. G.; Lee, S. H.; Cho, K. Y.; Park, J. K., Effects of triacetoxyvinylsilane as SEI layer additive on electrochemical performance of lithium metal secondary battery. *Electrochem Solid St* **2007,** *10* (9), A216-A219.
6. Petkova, G.; Nikolov, P.; Pavlov, D., Influence of polymer additive on the performance of lead-acid battery negative plates. *J Power Sources* **2006,** *158* (2), 841-845.
7. Huret, B. S., Nickel-Cadmium Battery Performance on the Rise. *Electron Prod* **1990,** *32* (8), 47-48.
8. Li, L.; Wu, F.; Chen, R. J.; Gao, X. P.; Shan, Z. Q., A new regeneration process for spent nickel/metal hydride batteries. *T Nonferr Metal Soc* **2005,** *15* (4), 764-768.

9. Zhang, Z. R.; Gong, Z. L.; Yang, Y., Electrochemical performance and surface properties of bare and TiO2-coated cathode materials in lithium-ion batteries. *J Phys Chem B* **2004,** *108* (45), 17546-17552.

10. Kim, H. S.; Jeong, T. G.; Kim, Y. T., Electrochemical Properties of Lithium Sulfur Battery with Silicon Anodes Lithiated by Direct Contact Method. *J Electrochem Sci Te* **2016,** *7* (3), 228-233.

11. Girishkumar, G.; McCloskey, B.; Luntz, A. C.; Swanson, S.; Wilcke, W., Lithium - Air Battery: Promise and Challenges. *J Phys Chem Lett* **2010,** *1* (14), 2193-2203.

12. Zhang, T.; Imanishi, N.; Shimonishi, Y.; Hirano, A.; Takeda, Y.; Yamamoto, O.; Sammes, N., A novel high energy density rechargeable lithium/air battery. *Chem Commun* **2010,** *46* (10), 1661-1663.

13. Zhang, D.; Li, R. S.; Huang, T.; Yu, A. S., Novel composite polymer electrolyte for lithium air batteries. *J Power Sources* **2010,** *195* (4), 1202-1206.

14. Xu, W.; Xiao, J.; Wang, D. Y.; Zhang, J.; Zhang, J. G., Effects of Nonaqueous Electrolytes on the Performance of Lithium/Air Batteries. *J Electrochem Soc* **2010,** *157* (2), A219-A224.

15. Wang, C.; Chen, J. J.; Shi, Y. N.; Zheng, M. S.; Dong, Q. F., Preparation and performance of a core-shell carbon/sulfur material for lithium/sulfur battery. *Electrochim Acta* **2010,** *55* (23), 7010-7015.

16. Li, Y. J.; Zhan, H.; Huang, K. L.; Zhou, Y. H., All Solid State Lithium Sulfur Rechargeable Battery with PEO-based Polymer Electrolytes. *Acta Chim Sinica* **2010,** *68* (18), 1850-1854.

17. Zhang, S. C.; Zhang, L.; Wang, W. K.; Xue, W. J., A Novel cathode material based on

polyaniline used for lithium/sulfur secondary battery. *Synthetic Met* **2010,** *160* (17-18), 2041-2044.

18. Ji, X. L.; Nazar, L. F., Advances in Li-S batteries. *J Mater Chem* **2010,** *20* (44), 9821-9826.
19. Yang, Z. G.; Zhang, J. L.; Kintner-Meyer, M. C. W.; Lu, X. C.; Choi, D. W.; Lemmon, J. P.; Liu, J., Electrochemical Energy Storage for Green Grid. *Chem Rev* **2011,** *111* (5), 3577-3613.
20. Goodenough, J. B.; Kim, Y., Challenges for Rechargeable Li Batteries. *Chem Mater* **2010,** *22* (3), 587-603.
21. Manthiram, A.; Fu, Y. Z.; Chung, S. H.; Zu, C. X.; Su, Y. S., Rechargeable Lithium-Sulfur Batteries. *Chem Rev* **2014,** *114* (23), 11751-11787.
22. Zhang, S. S., Liquid electrolyte lithium/sulfur battery: Fundamental chemistry, problems, and solutions. *J Power Sources* **2013,** *231*, 153-162.
23. Park, C. W.; Ahn, J. H.; Ryu, H. S.; Kim, K. W.; Ahn, H. J., Room-temperature solid-state sodium/sulfur battery. *Electrochem Solid St* **2006,** *9* (3), A123-A125.
24. Ryu, H. S.; Ahn, H. J.; Kim, K. W.; Ahn, J. H.; Cho, K. K.; Nam, T. H., Self-discharge characteristics of lithium/sulfur batteries using TEGDME liquid electrolyte. *Electrochim Acta* **2006,** *52* (4), 1563-1566.
25. Akridge, J. R.; Mikhaylik, Y. V.; White, N., Li/S fundamental chemistry and application to high-performance rechargeable batteries. *Solid State Ionics* **2004,** *175* (1-4), 243-245.
26. Shim, J.; Striebel, K. A.; Cairns, E. J., The lithium/sulfur rechargeable cell - Effects of electrode composition and solvent on cell performance. *J Electrochem Soc* **2002,**

149 (10), A1321-A1325.

27. Mosavati, N.; Chitturi, V. R.; Arava, L. M. R.; Salley, S. O.; Ng, K. Y. S., Effects of Nickel Particle Size and Graphene Support on the Electrochemical Performance of Lithium/Dissolved Polysulfide Batteries. *Electrochim Acta* **2015,** *185*, 297-303.
28. Mosavati, N.; Chitturi, V. R.; Salley, S. O.; Ng, K. Y. S., Nanostructured titanium nitride as a novel cathode for high performance lithium/dissolved polysulfide batteries. *J Power Sources* **2016,** *321*, 87-93.
29. Wild, M.; O'Neill, L.; Zhang, T.; Purkayastha, R.; Minton, G.; Marinescu, M.; Offer, G. J., Lithium sulfur batteries, a mechanistic review. *Energ Environ Sci* **2015,** *8* (12), 3477-3494.
30. Barchasz, C.; Lepretre, J. C.; Alloin, F.; Patoux, S., New insights into the limiting parameters of the Li/S rechargeable cell. *J Power Sources* **2012,** *199*, 322-330.
31. Mikhaylik, Y. V.; Akridge, J. R., Polysulfide shuttle study in the Li/S battery system. *J Electrochem Soc* **2004,** *151* (11), A1969-A1976.
32. Zhang, B.; Qin, X.; Li, G. R.; Gao, X. P., Enhancement of long stability of sulfur cathode by encapsulating sulfur into micropores of carbon spheres. *Energ Environ Sci* **2010,** *3* (10), 1531-1537.
33. Barchasz, C.; Mesguich, F.; Dijon, J.; Lepretre, J. C.; Patoux, S.; Alloin, F., Novel positive electrode architecture for rechargeable lithium/sulfur batteries. *J Power Sources* **2012,** *211*, 19-26.
34. Evers, S.; Nazar, L. F., Graphene-enveloped sulfur in a one pot reaction: a cathode with good coulombic efficiency and high practical sulfur content. *Chem Commun* **2012,** *48* (9), 1233-1235.

35. Guo, J. C.; Xu, Y. H.; Wang, C. S., Sulfur-Impregnated Disordered Carbon Nanotubes Cathode for Lithium-Sulfur Batteries. *Nano Lett* **2011,** *11* (10), 4288-4294.

36. Swiderska-Mocek, A.; Rudnicka, E., Lithium-sulphur battery with activated carbon cloth-sulphur cathode and ionic liquid as electrolyte. *J Power Sources* **2015,** *273*, 162-167.

37. Thieme, S.; Bruckner, J.; Meier, A.; Bauer, I.; Gruber, K.; Kaspar, J.; Helmer, A.; Althues, H.; Schmuck, M.; Kaskel, S., A lithium-sulfur full cell with ultralong cycle life: influence of cathode structure and polysulfide additive. *J Mater Chem A* **2015,** *3* (7), 3808-3820.

38. Wang, H. L.; Yang, Y.; Liang, Y. Y.; Robinson, J. T.; Li, Y. G.; Jackson, A.; Cui, Y.; Dai, H. J., Graphene-Wrapped Sulfur Particles as a Rechargeable Lithium-Sulfur Battery Cathode Material with High Capacity and Cycling Stability. *Nano Lett* **2011,** *11* (7), 2644-2647.

39. Zhang, J.; Guo, J. X.; Xia, Y.; Gan, Y. P.; Huang, H.; Liang, C.; Du, G. H.; Tao, X. Y.; Zhang, W. K., Hierarchically assembled mesoporous carbon nanosheets with an ultra large pore volume for high-performance lithium-sulfur batteries. *New J Chem* **2019,** *43* (3), 1380-1387.

40. Li, D.; Han, F.; Wang, S.; Cheng, F.; Sun, Q.; Li, W. C., High Sulfur Loading Cathodes Fabricated Using Peapodlike, Large Pore Volume Mesoporous Carbon for Lithium-Sulfur Battery. *Acs Appl Mater Inter* **2013,** *5* (6), 2208-2213.

41. Shyamsunder, A.; Beichel, W.; Klose, P.; Pang, Q.; Scherer, H.; Hoffmann, A.; Murphy, G. K.; Krossing, I.; Nazar, L. F., Inhibiting Polysulfide Shuttle in Lithium-Sulfur Batteries through Low-Ion-Pairing Salts and a Triflamide Solvent. *Angew*

Chem Int Edit **2017,** *56* (22), 6192-6197.

42. Li, Z.; Han, Y.; Wei, J. H.; Wang, W. Q.; Cao, T. T.; Xu, S. M.; Xu, Z. H., Suppressing Shuttle Effect Using Janus Cation Exchange Membrane for High-Performance Lithium-Sulfur Battery Separator. *Acs Appl Mater Inter* **2017,** *9* (51), 44776-44781.
43. Li, H. P.; Sun, L. C.; Zhao, Y.; Tan, T. Z.; Zhang, Y. G., A novel CuS/graphene-coated separator for suppressing the shuttle effect of lithium/sulfur batteries. *Appl Surf Sci* **2019,** *466*, 309-319.
44. Lee, J. H.; Kang, J.; Kim, S. W.; Halim, W.; Frey, M. W.; Joo, Y. L., Effective Suppression of the Polysulfide Shuttle Effect in Lithium-Sulfur Batteries by Implementing rGO-PEDOT:PSS-Coated Separators via Air-Controlled Electrospray. *Acs Omega* **2018,** *3* (12), 16465-16471.
45. Kim, H. S.; Jeong, C. S.; Kim, Y. T., Shuttle inhibitor effect of lithium perchlorate as an electrolyte salt for lithium-sulfur batteries. *J Appl Electrochem* **2012,** *42* (2), 75-79.
46. Gu, M.; Lee, J.; Kim, Y.; Kim, J. S.; Jang, B. Y.; Lee, K. T.; Kim, B. S., Inhibiting the shuttle effect in lithium-sulfur batteries using a layer-by-layer assembled ion-permselective separator. *Rsc Adv* **2014,** *4* (87), 46940-46946.
47. Fan, L.; Chen, S. H.; Zhu, J. Y.; Ma, R. F.; Li, S. P.; Podila, R.; Rao, A. M.; Yang, G. Z.; Wang, C. X.; Liu, Q.; Xu, Z.; Yuan, L. X.; Huang, Y. H.; Lu, B. A., Simultaneous Suppression of the Dendrite Formation and Shuttle Effect in a Lithium-Sulfur Battery by Bilateral Solid Electrolyte Interface. *Adv Sci* **2018,** *5* (9).
48. Demir-Cakan, R., Targeting the role of lithium sulphide formation for the rapid capacity fading in lithium-sulphur batteries. *J Power Sources* **2015,** *282*, 437-443.
49. Chu, H.; Noh, H.; Kim, Y. J.; Yuk, S.; Lee, J. H.; Lee, J.; Kwack, H.; Kim, Y.; Yang,

D. K.; Kim, H. T., Achieving three-dimensional lithium sulfide growth in lithium-sulfur batteries using high-donor-number anions. *Nat Commun* **2019,** *10*.

50. Chen, L. P.; Li, X. F.; Xu, Y. H., Recent advances of polar transition-metal sulfides host materials for advanced lithium-sulfur batteries. *Funct Mater Lett* **2018,** *11* (6).
51. Celik, K. B.; Cengiz, E. C.; Sar, T.; Dursun, B.; Ozturk, O.; Akbas, M. Y.; Demir-Cakan, R., In-situ wrapping of tin oxide nanoparticles by bacterial cellulose derived carbon nanofibers and its application as freestanding interlayer in lithium sulfide based lithium-sulfur batteries. *J Colloid Interf Sci* **2018,** *530*, 137-145.
52. Wang, Y.; Sahadeo, E.; Rubloff, G.; Lin, C. F.; Lee, S. B., High-capacity lithium sulfur battery and beyond: a review of metal anode protection layers and perspective of solid-state electrolytes. *J Mater Sci* **2019,** *54* (5), 3671-3693.
53. Ma, G. Q.; Wen, Z. Y.; Wu, M. F.; Shen, C.; Wang, Q. S.; Jin, J.; Wu, X. W., A lithium anode protection guided highly-stable lithium-sulfur battery. *Chem Commun* **2014,** *50* (91), 14209-14212.
54. Chen, J. Z.; Henderson, W. A.; Pan, H. L.; Perdue, B. R.; Cao, R. G.; Hu, J. Z.; Wan, C.; Han, K. S.; Mueller, K. T.; Zhang, J. G.; Shao, Y. Y.; Liu, J., Improving Lithium-Sulfur Battery Performance under Lean Electrolyte through Nanoscale Confinement in Soft Swellable Gels. *Nano Lett* **2017,** *17* (5), 3061-3067.
55. Karaseva, E. V.; Kuzmina, E. V.; Kolosnitsyn, D. V.; Shakirova, N. V.; Sheina, L. V.; Kolosnitsyn, V. S., The mechanism of effect of support salt concentration in electrolyte on performance of lithium-sulfur cells. *Electrochim Acta* **2019,** *296*, 1102-1114.
56. Strubel, P.; Althues, H.; Kaskel, S., Zinc-salt templating of hierarchical porous

carbons for low electrolyte high energy lithium-sulfur batteries (LE-LiS). *Carbon* **2016,** *107*, 705-710.

57. Xiong, S. Z.; Xie, K.; Diao, Y.; Hong, X. B., Properties of surface film on lithium anode with LiNO3 as lithium salt in electrolyte solution for lithium-sulfur batteries. *Electrochim Acta* **2012,** *83*, 78-86.
58. Jeong, T. G.; Chun, J.; Cho, B. W.; Lee, J.; Kim, Y. T., Enhanced performance of sulfur-infiltrated bimodal mesoporous carbon foam by chemical solution deposition as cathode materials for lithium sulfur batteries. *Sci Rep-Uk* **2017,** *7*.
59. Yuan, S. Y.; Bao, J. L.; Wang, L. N.; Xia, Y. Y.; Truhlar, D. G.; Wang, Y. G., Graphene-Supported Nitrogen and Boron Rich Carbon Layer for Improved Performance of Lithium-Sulfur Batteries Due to Enhanced Chemisorption of Lithium Polysulfides. *Adv Energy Mater* **2016,** *6* (5).
60. Liu, S. K.; Xie, K.; Li, Y. J.; Chen, Z. X.; Hong, X. B.; Zhou, L. J.; Yuan, J. F.; Zheng, C. M., Graphene oxide wrapped hierarchical porous carbon-sulfur composite cathode with enhanced cycling and rate performance for lithium sulfur batteries. *Rsc Adv* **2015,** *5* (8), 5516-5522.
61. Wei, S. C.; Zhang, H.; Huang, Y. Q.; Wang, W. K.; Xia, Y. Z.; Yu, Z. B., Pig bone derived hierarchical porous carbon and its enhanced cycling performance of lithium-sulfur batteries. *Energ Environ Sci* **2011,** *4* (3), 736-740.
62. Zeng, J. H.; Wang, Y. F.; Gou, S. Q.; Zhang, L. P.; Chen, Y.; Jiang, J. X.; Shi, F., Sulfur in Hyper-cross-linked Porous Polymer as Cathode in Lithium-Sulfur Batteries with Enhanced Electrochemical Properties. *Acs Appl Mater Inter* **2017,** *9* (40), 34783-34792.

63. Zeng, S. B.; Li, L. G.; Zhao, D. K.; Liu, J.; Niu, W. H.; Wang, N.; Chen, S. W., Polymer-Capped Sulfur Copolymers as Lithium-Sulfur Battery Cathode: Enhanced Performance by Combined Contributions of Physical and Chemical Confinements. *J Phys Chem C* **2017,** *121* (5), 2495-2503.

64. Hu, H.; Cheng, H. Y.; Liu, Z. F.; Li, G. J.; Zhu, Q. C.; Yu, Y., In Situ Polymerized PAN-Assisted S/C Nanosphere with Enhanced High-Power Performance as Cathode for Lithium/Sulfur Batteries. *Nano Lett* **2015,** *15* (8), 5116-5123.

65. Wang, J. L.; Yang, J.; Xie, J. Y.; Xu, N. X.; Li, Y., Sulfur-carbon nano-composite as cathode for rechargeable lithium battery based on gel electrolyte. *Electrochem Commun* **2002,** *4* (6), 499-502.

66. Ji, X. L.; Lee, K. T.; Nazar, L. F., A highly ordered nanostructured carbon-sulphur cathode for lithium-sulphur batteries. *Nat Mater* **2009,** *8* (6), 500-506.

67. Zhou, H. L.; Wang, D. X.; Fu, A. P.; Liu, X. H.; Wang, Y. Q.; Li, Y. H.; Guo, P. Z.; Li, H. L.; Zhao, X. S., Mesoporous carbon spheres with tunable porosity prepared by a template-free method for advanced lithium-sulfur batteries. *Mater Sci Eng B-Adv* **2018,** *227*, 9-15.

68. Zheng, J. M.; Gu, M.; Wagner, M. J.; Hays, K. A.; Li, X. H.; Zuo, P. J.; Wang, C. M.; Zhang, J. G.; Liu, J.; Xiao, J., Revisit Carbon/Sulfur Composite for Li-S Batteries. *J Electrochem Soc* **2013,** *160* (10), A1624-A1628.

69. Zhao, X.; Ahn, H. J.; Kim, K. W.; Cho, K. K.; Ahn, J. H., Polyaniline-Coated Mesoporous Carbon/Sulfur Composites for Advanced Lithium Sulfur Batteries. *J Phys Chem C* **2015,** *119* (15), 7996-8003.

70. Zhao, Q. N.; Zhao, K. Q.; Ji, G. P.; Guo, X. L.; Han, M.; Wen, J.; Ren, Z. L.; Zhao, S.

C.; Gao, Z.; Wang, R. H.; Li, M.; Sun, K. A.; Hu, N.; Xu, C. H., High sulfur loading, rGO-linked and polymer binder-free cathodes based on rGO wrapped N,P-codoped mesoporous carbon as sulfur host for Li-S batteries. *Chem Eng J* **2019,** *361*, 1043-1052.

71. Zhao, Q.; Zhu, Q. H.; Miao, J. W.; Guan, Z. X.; Liu, H.; Chen, R. J.; An, Y. B.; Wu, F.; Xu, B., Three-Dimensional Carbon Current Collector Promises Small Sulfur Molecule Cathode with High Areal Loading for Lithium-Sulfur Batteries. *Acs Appl Mater Inter* **2018,** *10* (13), 10882-10889.
72. Zhou, X. Z.; Ma, Q. R.; Zhang, X. W.; Lu, X. F.; Wang, J. W.; Wang, Q. T., 3D-Mesoporous Carbon Infiltrated with Sulfur for High-Rate Stable Lithium-Sulfur Batteries. *Chemistryselect* **2017,** *2* (14), 4131-4137.
73. Xu, N. N.; Zhu, T. S.; Qiao, J. L.; Zhang, F. Y.; Chen, Z. W., Nitrogen and sulfur co-doped mesoporous carbon as cathode catalyst for H-2/O-2 alkaline membrane fuel cell effect of catalyst/bonding layer loading. *Int J Hydrogen Energ* **2016,** *41* (21), 9159-9166.
74. Xu, N.; Qian, T.; Liu, X. J.; Liu, J.; Chen, Y.; Yang, C. L., Greatly Suppressed Shuttle Effect for Improved Lithium Sulfur Battery Performance through Short Chain Intermediates. *Nano Lett* **2017,** *17* (1), 538-543.
75. Xin, S.; Yin, Y. X.; Wan, L. J.; Guo, Y. G., Encapsulation of Sulfur in a Hollow Porous Carbon Substrate for Superior Li-S Batteries with Long Lifespan. *Part Part Syst Char* **2013,** *30* (4), 321-325.
76. Xin, S.; Gu, L.; Zhao, N. H.; Yin, Y. X.; Zhou, L. J.; Guo, Y. G.; Wan, L. J., Smaller Sulfur Molecules Promise Better Lithium-Sulfur Batteries. *J Am Chem Soc* **2012,** *134*

(45), 18510-18513.

77. Wang, T. L.; Shi, P. C.; Chen, J. J.; Cheng, S.; Xiang, H. F., Effects of porous structure of carbon hosts on preparation and electrochemical performance of sulfur/carbon composites for lithium-sulfur batteries. *J Nanopart Res* **2016,** *18* (1).

78. Xiao, Z. B.; Yang, Z.; Nie, H. G.; Lu, Y. Q.; Yang, K. Q.; Huang, S. M., Porous carbon nanotubes etched by water steam for high-rate large-capacity lithium-sulfur batteries. *J Mater Chem A* **2014,** *2* (23), 8683-8689.

79. He, M.; Yuan, L. X.; Zhang, W. X.; Huang, Y. H., Porous carbon nanotubes improved sulfur composite cathode for lithium-sulfur battery. *J Solid State Electr* **2013,** *17* (6), 1641-1647.

80. Hagen, M.; Dorfler, S.; Althues, H.; Tubke, J.; Hoffmann, M. J.; Kaskel, S.; Pinkwart, K., Lithium-sulphur batteries - binder free carbon nanotubes electrode examined with various electrolytes. *J Power Sources* **2012,** *213*, 239-248.

81. Chen, M.; Yu, C.; Liu, S. H.; Fan, X. M.; Zhao, C. T.; Zhang, X.; Qiu, J. S., Micro-sized porous carbon spheres with ultra-high rate capability for lithium storage. *Nanoscale* **2015,** *7* (5), 1791-1795.

82. Jayaprakash, N.; Shen, J.; Moganty, S. S.; Corona, A.; Archer, L. A., Porous Hollow Carbon@Sulfur Composites for High-Power Lithium-Sulfur Batteries. *Angew Chem Int Edit* **2011,** *50* (26), 5904-5908.

83. Han, S. C.; Song, M. S.; Lee, H.; Kim, H. S.; Ahn, H. J.; Lee, J. Y., Effect of multiwalled carbon nanotubes on electrochemical properties of lithium sulfur rechargeable batteries. *J Electrochem Soc* **2003,** *150* (7), A889-A893.

84. Chu, R. X.; Lin, J.; Wu, C. Q.; Zheng, J.; Chen, Y. L.; Zhang, J.; Han, R. H.; Zhang,

Y.; Guo, H., Reduced graphene oxide coated porous carbon-sulfur nanofiber as a flexible paper electrode for lithium-sulfur batteries. *Nanoscale* **2017,** *9* (26), 9129-9138.

85. Li, Q.; Zhang, Z. A.; Guo, Z. P.; Lai, Y. Q.; Zhang, K.; Li, J., Improved cyclability of lithium-sulfur battery cathode using encapsulated sulfur in hollow carbon nanofiber@nitrogen-doped porous carbon core-shell composite. *Carbon* **2014,** *78*, 1-9.
86. Tan, Y. B.; Jia, Z. Q.; Lou, P. L.; Cui, Z. H.; Guo, X. X., Self-assembly sandwiches of reduced graphene oxide layers with zeolitic-imidazolate-frameworks-derived mesoporous carbons as polysulfides reservoirs for lithium-sulfur batteries. *J Power Sources* **2017,** *341*, 68-74.
87. Du, W. C.; Zhang, J.; Yin, Y. X.; Guo, Y. G.; Wan, L. J., Sulfur Confined in Sub-Nanometer-Sized 2D Graphene Interlayers and Its Electrochemical Behavior in Lithium-Sulfur Batteries. *Chem-Asian J* **2016,** *11* (19), 2690-2694.
88. Guo, J. C., Graphene oxide based cathode for lithium-sulfur batteries. *Abstr Pap Am Chem S* **2016,** *252*.
89. Wang, L.; Yi, Z. C.; Wang, X.; Zhang, Y. G.; Jin, M. L.; Zhou, G. F., A Novel Binder-Free Sulfur/Polypyrrole Cathode for Lithium/Sulfur Batteries. *Int J Electrochem Sc* **2017,** *12* (6), 5521-5528.
90. Li, M. Y.; Carter, R.; Douglas, A.; Oakes, L.; Pint, C. L., Sulfur Vapor-Infiltrated 3D Carbon Nanotube Foam for Binder-Free High Areal Capacity Lithium-Sulfur Battery Composite Cathodes. *Acs Nano* **2017,** *11* (5), 4877-4884.
91. Guo, J. L.; Zhang, X. L.; Du, X. Y.; Zhang, F. X., A Mn3O4 nano-wall array based

binder-free cathode for high performance lithium-sulfur batteries. *J Mater Chem A* **2017,** *5* (14), 6447-6454.

92. Chen, Y.; Lu, S. T.; Zhou, J.; Wu, X. H.; Qin, W.; Ogoke, O.; Wu, G., 3D graphene framework supported Li2S coated with ultra-thin Al2O3 films: binder-free cathodes for high-performance lithium sulfur batteries. *J Mater Chem A* **2017,** *5* (1), 102-112.
93. Sun, L.; Wang, D. T.; Luo, Y. F.; Kong, W. B.; Wu, Y.; Zhang, L. N.; Jiang, K. L.; Li, Q. Q.; Zhang, Y. H.; Wang, J. P.; Fan, S. S., Sulfur Embedded in a Mesoporous Carbon Nanotube Network as a Binder-Free Electrode for High-Performance Lithium Sulfur Batteries. *Acs Nano* **2016,** *10* (1), 1300-1308.
94. Kong, W. B.; Sun, L.; Wu, Y.; Jiang, K. L.; Li, Q. Q.; Wang, J. P.; Fan, S. S., Binder-free polymer encapsulated sulfur-carbon nanotube composite cathodes for high performance lithium batteries. *Carbon* **2016,** *96*, 1053-1059.
95. Lu, S. T.; Chen, Y.; Wu, X. H.; Wang, Z. D.; Lv, L. Y.; Qin, W.; Jiang, L. X., Binder-free cathodes based on sulfur-carbon nanofibers composites for lithium-sulfur batteries. *Rsc Adv* **2014,** *4* (35), 18052-18064.
96. Elazari, R.; Salitra, G.; Garsuch, A.; Panchenko, A.; Aurbach, D., Sulfur-Impregnated Activated Carbon Fiber Cloth as a Binder-Free Cathode for Rechargeable Li-S Batteries. *Adv Mater* **2011,** *23* (47), 5641-+.
97. Dorfler, S.; Felhosi, I.; Marek, T.; Thieme, S.; Althues, H.; Nyikos, L.; Kaskel, S., High power supercap electrodes based on vertical aligned carbon nanotubes on aluminum. *J Power Sources* **2013,** *227*, 218-228.
98. Dou, X. Y.; Zhou, Z. P.; Tan, P. H.; Song, L.; Liu, L. F.; Zhao, X. W.; Luo, S. D.; Yan, X. Q.; Liu, D. F.; Wang, J. X.; Gao, Y.; Zhang, Z. X.; Yuan, H. J.; Zhou, W. Y.; Xie, S.

S., Surface-enhanced resonant Raman spectroscopy (SERRS) of single-walled carbon nanotubes absorbed on the Ag-coated anodic aluminum oxide (AAO) surface. *Physica E* **2005,** *27* (4), 469-473.

99. Ma, Y. C.; Huang, Y. D.; Wang, X. C.; Jia, D. Z.; Tang, X. C., One-pot synthesis of Fe3O4/C nanocomposites by PEG-assisted co-precipitation as anode materials for high-rate lithium-ion batteries. *J Nanopart Res* **2014,** *16* (10).
100. Wang, Z. H.; Chen, Y. L.; Battaglia, V.; Liu, G., Improving the performance of lithium-sulfur batteries using conductive polymer and micrometric sulfur powder. *Abstr Pap Am Chem S* **2014,** *248*.
101. Wang, Z. H.; Chen, Y. L.; Battaglia, V.; Liu, G., Improving the performance of lithium-sulfur batteries using conductive polymer and micrometric sulfur powder. *J Mater Res* **2014,** *29* (9), 1027-1033.
102. Duan, L.; Lu, J. C.; Liu, W. Y.; Huang, P.; Wang, W. S.; Liu, Z. C., Fabrication of conductive polymer-coated sulfur composite cathode materials based on layer-by-layer assembly for rechargeable lithium-sulfur batteries. *Colloid Surface A* **2012,** *414*, 98-103.
103. Yang, Y.; Yu, G. H.; Cha, J. J.; Wu, H.; Vosgueritchian, M.; Yao, Y.; Bao, Z. A.; Cui, Y., Improving the Performance of Lithium-Sulfur Batteries by Conductive Polymer Coating. *Acs Nano* **2011,** *5* (11), 9187-9193.
104. Yu, X. G.; Xie, J. Y.; Yang, J.; Huang, H. J.; Wang, K.; Wen, Z. S., Lithium storage in conductive sulfur-containing polymers. *J Electroanal Chem* **2004,** *573* (1), 121-128.
105. Wang, J. L.; Yang, J.; Xie, J. Y.; Xu, N. X., A novel conductive polymer-sulfur composite cathode material for rechargeable lithium batteries. *Adv Mater* **2002,** *14*

(13-14), 963-+.

106. Liang, X.; Wen, Z. Y.; Liu, Y.; Wang, X. Y.; Zhang, H.; Wu, M. F.; Huang, L. Z., Preparation and characterization of sulfur-polypyrrole composites with controlled morphology as high capacity cathode for lithium batteries. *Solid State Ionics* **2011,** *192* (1), 347-350.
107. Sun, M. M.; Zhang, S. C.; Jiang, T.; Zhang, L.; Yu, J. H., Nano-wire networks of sulfur-polypyrrole composite cathode materials for rechargeable lithium batteries. *Electrochem Commun* **2008,** *10* (12), 1819-1822.
108. Wu, F.; Chen, J. Z.; Li, L.; Zhao, T.; Chen, R. J., Improvement of Rate and Cycle Performence by Rapid Polyaniline Coating of a MWCNT/Sulfur Cathode. *J Phys Chem C* **2011,** *115* (49), 24411-24417.
109. Li, X. G.; Rao, M. M.; Li, W. S., Sulfur encapsulated in porous carbon nanospheres and coated with conductive polyaniline as cathode of lithium-sulfur battery. *J Solid State Electr* **2016,** *20* (1), 153-161.
110. Zou, Y. L.; Duan, J. L.; Qi, Z. A.; Wang, Y.; Dong, S. J.; Li, Z. Y., Nonfilling polyaniline coating of sulfur/acetylene black for high-performance lithium sulfur batteries. *J Electroanal Chem* **2018,** *811*, 46-52.
111. Li, S.; Cen, Y.; Xiang, Q.; Aslam, M. K.; Hu, B. B.; Li, W.; Tang, Y.; Yu, Q.; Liu, Y. P.; Chen, C. G., Vanadium dioxide- reduced graphene oxide binary host as an efficient polysulfide plague for highperformance lithium- sulfur batteries. *J Mater Chem A* **2019,** *7* (4), 1658-1668.
112. Hou, Y. X.; Xiao, J.; Guo, Y. F.; Qi, M.; Jiang, A. H.; Li, Y. W., Gaseous-phase, silica-coated sulfur particles as a cathode material for high-performance lithium/sulfur

batteries. *J Mater Sci-Mater El* **2017,** *28* (12), 8901-8907.

113. Meng, X. B.; Liu, Y. Z.; Cao, Y. Q.; Ren, Y.; Lu, W. Q.; Elam, J. W., High-Performance High-Loading Lithium-Sulfur Batteries by Low Temperature Atomic Layer Deposition of Aluminum Oxide on Nanophase S Cathodes. *Adv Mater Interfaces* **2017,** *4* (17).

114. Doeff, M. M.; Hollingsworth, J.; Shim, J.; Lee, Y. J.; Striebel, K.; Reimer, J. A.; Cairns, E. J., Sulfur-doped aluminum-substituted manganese oxide spinels for lithium-ion battery applications. *J Electrochem Soc* **2003,** *150* (8), A1060-A1066.

115. Liang, X.; Kwok, C. Y.; Lodi-Marzano, F.; Pang, Q.; Cuisinier, M.; Huang, H.; Hart, C. J.; Houtarde, D.; Kaup, K.; Sommer, H.; Brezesinski, T.; Janek, J.; Nazar, L. F., Tuning Transition Metal Oxide-Sulfur Interactions for Long Life Lithium Sulfur Batteries: The "Goldilocks" Principle. *Adv Energy Mater* **2016,** *6* (6).

116. Song, B. H.; Li, W. D.; Yan, P. F.; Oh, S. M.; Wang, C. M.; Manthiram, A., A facile cathode design combining Ni-rich layered oxides with Li-rich layered oxides for lithium-ion batteries. *J Power Sources* **2016,** *325*, 620-629.

117. Mohanty, S. P.; Kishore, B.; Nookala, M., Composites of Sulfur-Titania Nanotubes Prepared by a Facile Solution Infiltration Route as Cathode Material in Lithium-Sulfur Battery. *J Nanosci Nanotechno* **2018,** *18* (10), 6830-6837.

118. Xu, J. H.; Jin, B.; Li, H.; Jiang, Q., Sulfur/alumina/polypyrrole ternary hybrid material as cathode for lithium-sulfur batteries. *Int J Hydrogen Energ* **2017,** *42* (32), 20749-20758.

119. Dong, K.; Wang, S. P.; Zhang, H. Y.; Wu, J. P., Preparation and electrochemical performance of sulfur-alumina cathode material for lithium-sulfur batteries. *Mater*

Res Bull **2013,** *48* (6), 2079-2083.

120. Choi, S.; Su, D. W.; Shin, M.; Park, S.; Wang, G. X., Pomegranate-Structured Silica/Sulfur Composite Cathodes for High-Performance Lithium-Sulfur Batteries. *Chem-Asian J* **2018,** *13* (5), 568-576.
121. Chen, Y. H.; Tarascon, J. M.; Guery, C., Exploring sulfur solubility in ionic liquids for the electrodeposition of sulfide films with their electrochemical reactivity toward lithium. *Electrochim Acta* **2013,** *99*, 46-53.
122. Seh, Z. W.; Li, W. Y.; Cha, J. J.; Zheng, G. Y.; Yang, Y.; McDowell, M. T.; Hsu, P. C.; Cui, Y., fSulphur-TiO2 yolk-shell nanoarchitecture with internal void space for long-cycle lithium-sulphur batteries. *Nat Commun* **2013,** *4*.
123. Cui, Z. M.; Zu, C. X.; Zhou, W. D.; Manthiram, A.; Goodenough, J. B., Mesoporous Titanium Nitride-Enabled Highly Stable Lithium-Sulfur Batteries. *Adv Mater* **2016,** *28* (32), 6926-+.
124. Mikhaylik, Y.; Kovalev, I.; Schock, R.; Kumaresan, K.; Xu, J.; Affinito, J., High Energy Rechargeable Li-S Cells for EV Application. Status, Remaining Problems and Solutions. *Ecs Transactions* **2010,** *25* (35), 23-34.
125. Zheng, M. S.; Chen, J. J.; Dong, Q. F., The enhanced electrochemical performance of lithium/sulfur battery with protected lithium anode. *Adv Mater Res-Switz* **2012,** *476-478*, 676-680.
126. Aurbach, D.; Pollak, E.; Elazari, R.; Salitra, G.; Kelley, C. S.; Affinito, J., On the Surface Chemical Aspects of Very High Energy Density, Rechargeable Li-Sulfur Batteries. *J Electrochem Soc* **2009,** *156* (8), A694-A702.
127. Muldoon, J.; Bucur, C. B.; Oliver, A. G.; Sugimoto, T.; Matsui, M.; Kim, H. S.; Allred,

G. D.; Zajicek, J.; Kotani, Y., Electrolyte roadblocks to a magnesium rechargeable battery. *Energ Environ Sci* **2012,** *5* (3), 5941-5950.

128. Meng, X. H.; Savage, P. E.; Deng, D., Trash to Treasure: From Harmful Algal Blooms to High-Performance Electrodes for Sodium-Ion Batteries. *Environ Sci Technol* **2015,** *49* (20), 12543-12550.
129. Meng, X. H.; Deng, D., Trash to Treasure: Waste Eggshells Used as Reactor and Template for Synthesis of Co9S8 Nanorod Arrays on Carbon Fibers for Energy Storage. *Chem Mater* **2016,** *28* (11), 3897-3904.
130. Meng, X. H.; Deng, D., Core-Shell Ti@Si Coaxial Nanorod Arrays Formed Directly on Current Collectors for Lithium-Ion Batteries. *Acs Appl Mater Inter* **2015,** *7* (12), 6867-6874.
131. Mahmood, N.; Zhang, C. Z.; Yin, H.; Hou, Y. L., Graphene-based nanocomposites for energy storage and conversion in lithium batteries, supercapacitors and fuel cells. *J Mater Chem A* **2014,** *2* (1), 15-32.
132. Li, Q.; Mahmood, N.; Zhu, J. H.; Hou, Y. L.; Sun, S. H., Graphene and its composites with nanoparticles for electrochemical energy applications. *Nano Today* **2014,** *9* (5), 668-683.
133. Armand, M.; Tarascon, J. M., Building better batteries. *Nature* **2008,** *451* (7179), 652-657.
134. Rauh, R. D.; Shuker, F. S.; Marston, J. M.; Brummer, S. B., Formation of Lithium Polysulfides in Aprotic Media. *J Inorg Nucl Chem* **1977,** *39* (10), 1761-1766.
135. Jin, B.; Kim, J. U.; Gu, H. B., Electrochemical properties of lithium-sulfur batteries. *J Power Sources* **2003,** *117* (1-2), 148-152.

136. Ma, Y. W.; Zhang, H. Z.; Wu, B. S.; Wang, M. R.; Li, X. F.; Zhang, H. M., Lithium Sulfur Primary Battery with Super High Energy Density: Based on the Cauliflower-like Structured C/S Cathode. *Sci Rep-Uk* **2015,** *5*.

137. Ji, X. L.; Evers, S.; Black, R.; Nazar, L. F., Stabilizing lithium-sulphur cathodes using polysulphide reservoirs. *Nat Commun* **2011,** *2*.

138. Huff, L. A.; Rapp, J. L.; Baughman, J. A.; Rinaldi, P. L.; Gewirth, A. A., Identification of lithium-sulfur battery discharge products through Li-6 and S-33 solid-state MAS and Li-7 solution NMR spectroscopy. *Surf Sci* **2015,** *631*, 295-300.

139. Jeong, S. S.; Lim, Y.; Choi, Y. J.; Cho, G. B.; Kim, K. W.; Ahn, H. J.; Cho, K. K., Electrochemical properties of lithium sulfur cells using PEO polymer electrolytes prepared under three different mixing conditions. *J Power Sources* **2007,** *174* (2), 745-750.

140. Dominko, R.; Patel, M. U. M.; Lapornik, V.; Vizintin, A.; Kozelj, M.; Tusar, N. N.; Arcon, I.; Stievano, L.; Aquilanti, G., Analytical Detection of Polysulfides in the Presence of Adsorption Additives by Operando X-ray Absorption Spectroscopy. *J Phys Chem C* **2015,** *119* (33), 19001-19010.

141. Fu, Y. Z.; Su, Y. S.; Manthiram, A., Sulfur-Carbon Nanocomposite Cathodes Improved by an Amphiphilic Block Copolymer for High-Rate Lithium-Sulfur Batteries. *Acs Appl Mater Inter* **2012,** *4* (11), 6046-6052.

142. Zhang, S. S.; Read, J. A., A new direction for the performance improvement of rechargeable lithium/sulfur batteries. *J Power Sources* **2012,** *200*, 77-82.

143. Yin, Y. X.; Xin, S.; Guo, Y. G.; Wan, L. J., Lithium-Sulfur Batteries: Electrochemistry, Materials, and Prospects. *Angew Chem Int Edit* **2013,** *52* (50), 13186-13200.

144. Qie, L.; Zu, C. X.; Manthiram, A., A High Energy Lithium-Sulfur Battery with Ultrahigh-Loading Lithium Polysulfide Cathode and its Failure Mechanism. *Adv Energy Mater* **2016,** *6* (7).

145. Pope, M. A.; Aksay, I. A., Structural Design of Cathodes for Li-S Batteries. *Adv Energy Mater* **2015,** *5* (16).

146. Cheon, S. E.; Ko, K. S.; Cho, J. H.; Kim, S. W.; Chin, E. Y.; Kim, H. T., Rechargeable lithium sulfur battery - II. Rate capability and cycle characteristics. *J Electrochem Soc* **2003,** *150* (6), A800-A805.

147. Cheon, S. E.; Ko, K. S.; Cho, J. H.; Kim, S. W.; Chin, E. Y.; Kim, H. T., Rechargeable lithium sulfur battery - I. Structural change of sulfur cathode during discharge and charge. *J Electrochem Soc* **2003,** *150* (6), A796-A799.

148. Barchasz, C.; Molton, F.; Duboc, C.; Lepretre, J. C.; Patoux, S.; Alloin, F., Lithium/Sulfur Cell Discharge Mechanism: An Original Approach for Intermediate Species Identification. *Anal Chem* **2012,** *84* (9), 3973-3980.

149. Hao, Z. X.; Yuan, L. X.; Chen, C. J.; Xiang, J. W.; Li, Y. Y.; Huang, Z. M.; Hu, P.; Huang, Y. H., TiN as a simple and efficient polysulfide immobilizer for lithium-sulfur batteries. *J Mater Chem A* **2016,** *4* (45), 17711-17717.

150. Mosavati, N.; Salley, S. O.; Ng, K. Y. S., Characterization and electrochemical activities of nanostructured transition metal nitrides as cathode materials for lithium sulfur batteries. *J Power Sources* **2017,** *340*, 210-216.

151. Pang, Q.; Liang, X.; Kwok, C. Y.; Nazar, L. F., Review-The Importance of Chemical Interactions between Sulfur Host Materials and Lithium Polysulfides for Advanced Lithium-Sulfur Batteries. *J Electrochem Soc* **2015,** *162* (14), A2567-A2576.

152. Evers, S.; Yim, T.; Nazar, L. F., Understanding the Nature of Absorption/Adsorption in Nanoporous Polysulfide Sorbents for the Li-S Battery. *J Phys Chem C* **2012,** *116* (37), 19653-19658.

153. Yu, D. L.; Song, Y.; Zhu, X. F.; Yang, R. Q.; Han, A. J., Morphological evolution of TiO2 nanotube arrays with lotus-root-shaped nanostructure. *Appl Surf Sci* **2013,** *276*, 711-716.

154. Yu, D. L.; Song, Y.; Zhu, X. F.; Yang, C. Y.; Yang, B.; Xiao, H. P., Fabrication of bundle-free TiO2 nanotube arrays with wide open top via a modified two-step anodization process. *Mater Lett* **2013,** *109*, 211-213.

155. Zhu, X. F.; Song, Y.; Liu, L.; Wang, C. Y.; Zheng, J.; Jia, H. B.; Wang, X. L., Electronic currents and the formation of nanopores in porous anodic alumina. *Nanotechnology* **2009,** *20* (47).

156. Su, Z. X.; Zhou, W. Z., Formation Mechanism of Porous Anodic Aluminium and Titanium Oxides. *Adv Mater* **2008,** *20* (19), 3663-+.

157. Houser, J. E.; Hebert, K. R., The role of viscous flow of oxide in the growth of self-ordered porous anodic alumina films. *Nat Mater* **2009,** *8* (5), 415-420.

158. Zhang, G. G.; Li, W. F.; Xie, K. Y.; Yu, F.; Huang, H. T., A One-Step and Binder-Free Method to Fabricate Hierarchical Nickel-Based Supercapacitor Electrodes with Excellent Performance. *Adv Funct Mater* **2013,** *23* (29), 3675-3681.

159. Li, Z.; Zhang, J. T.; Lou, X. W., Hollow Carbon Nanofibers Filled with MnO2 Nanosheets as Efficient Sulfur Hosts for Lithium-Sulfur Batteries. *Angew Chem Int Edit* **2015,** *54* (44), 12886-12890.

160. Hart, C. J.; Cuisinier, M.; Liang, X.; Kundu, D.; Garsuch, A.; Nazar, L. F., Rational

design of sulphur host materials for Li-S batteries: correlating lithium polysulphide adsorptivity and self-discharge capacity loss. *Chem Commun* **2015,** *51* (12), 2308-2311.

161. Tang, C.; Zhang, Q.; Zhao, M. Q.; Huang, J. Q.; Cheng, X. B.; Tian, G. L.; Peng, H. J.; Wei, F., Nitrogen-Doped Aligned Carbon Nanotube/Graphene Sandwiches: Facile Catalytic Growth on Bifunctional Natural Catalysts and Their Applications as Scaffolds for High-Rate Lithium-Sulfur Batteries. *Adv Mater* **2014,** *26* (35), 6100-+.
162. Zhang, S. T.; Zheng, M. B.; Lin, Z. X.; Li, N. W.; Liu, Y. J.; Zhao, B.; Pang, H.; Cao, J. M.; He, P.; Shi, Y., Activated carbon with ultrahigh specific surface area synthesized from natural plant material for lithium-sulfur batteries. *J Mater Chem A* **2014,** *2* (38), 15889-15896.
163. Song, J. X.; Yu, Z. X.; Gordin, M. L.; Wang, D. H., Advanced Sulfur Cathode Enabled by Highly Crumpled Nitrogen-Doped Graphene Sheets for High-Energy-Density Lithium-Sulfur Batteries. *Nano Lett* **2016,** *16* (2), 864-870.
164. Sun, F. G.; Wang, J. T.; Long, D. H.; Qiao, W. M.; Ling, L. C.; Lv, C. X.; Cai, R., A high-rate lithium-sulfur battery assisted by nitrogen-enriched mesoporous carbons decorated with ultrafine La2O3 nanoparticles. *J Mater Chem A* **2013,** *1* (42), 13283-13289.
165. Schuster, J.; He, G.; Mandlmeier, B.; Yim, T.; Lee, K. T.; Bein, T.; Nazar, L. F., Spherical Ordered Mesoporous Carbon Nanoparticles with High Porosity for Lithium-Sulfur Batteries. *Angew Chem Int Edit* **2012,** *51* (15), 3591-3595.
166. Yuan, L. X.; Yuan, H. P.; Qiu, X. P.; Chen, L. Q.; Zhu, W. T., Improvement of cycle property of sulfur-coated multi-walled carbon nanotubes composite cathode for

lithium/sulfur batteries. *J Power Sources* **2009,** *189* (2), 1141-1146.

167. Dorfler, S.; Hagen, M.; Althues, H.; Tubke, J.; Kaskel, S.; Hoffmann, M. J., High capacity vertical aligned carbon nanotube/sulfur composite cathodes for lithium-sulfur batteries. *Chem Commun* **2012,** *48* (34), 4097-4099.
168. Bai, J. B.; Allaoui, A., Effect of the length and the aggregate size of MWNTs on the improvement efficiency of the mechanical and electrical properties of nanocomposites - experimental investigation. *Compos Part a-Appl S* **2003,** *34* (8), 689-694.
169. Zelenak, V.; Badanicova, M.; Halamova, D.; Cejka, J.; Zukal, A.; Murafa, N.; Goerigk, G., Amine-modified ordered mesoporous silica: Effect of pore size on carbon dioxide capture. *Chem Eng J* **2008,** *144* (2), 336-342.
170. Joo, S. H.; Kwon, K.; You, D. J.; Pak, C.; Chang, H.; Kim, J. M., Preparation of high loading Pt nanoparticles on ordered mesoporous carbon with a controlled Pt size and its effects on oxygen reduction and methanol oxidation reactions. *Electrochim Acta* **2009,** *54* (24), 5746-5753.
171. Kiani, M. A.; Mousavi, M. F.; Ghasemi, S., Size effect investigation on battery performance: Comparison between micro- and nano-particles of beta-Ni(OH)(2) as nickel battery cathode material. *J Power Sources* **2010,** *195* (17), 5794-5800.
172. Wang, L.; Yao, M. L.; Hu, X.; Hu, G. S.; Lu, J. Q.; Luo, M. F.; Fan, M. H., Amine-modified ordered mesoporous silica: The effect of pore size on CO2 capture performance. *Appl Surf Sci* **2015,** *324*, 286-292.
173. Wu, H.; Chan, G.; Choi, J. W.; Ryu, I.; Yao, Y.; McDowell, M. T.; Lee, S. W.; Jackson, A.; Yang, Y.; Hu, L. B.; Cui, Y., Stable cycling of double-walled silicon nanotube battery anodes through solid-electrolyte interphase control. *Nat Nanotechnol* **2012,** *7*

(5), 309-314.

174. Yuan, Z.; Peng, H. J.; Huang, J. Q.; Liu, X. Y.; Wang, D. W.; Cheng, X. B.; Zhang, Q., Hierarchical Free-Standing Carbon-Nanotube Paper Electrodes with Ultrahigh Sulfur-Loading for Lithium-Sulfur Batteries. *Adv Funct Mater* **2014,** *24* (39), 6105-6112.

175. Cheng, X. B.; Huang, J. Q.; Zhang, Q.; Peng, H. J.; Zhao, M. Q.; Wei, F., Aligned carbon nanotube/sulfur composite cathodes with high sulfur content for lithium-sulfur batteries. *Nano Energy* **2014,** *4*, 65-72.

176. Patil, A.; Choi, J. W.; Yoon, S. J., Review of issue and challenges facing rechargeable nanostructured lithium batteries. *Ieee Nmdc 2006: Ieee Nanotechnology Materials and Devices Conference 2006, Proceedings* **2006**, 196-197.

177. Tarascon, J. M.; Armand, M., Issues and challenges facing rechargeable lithium batteries. *Nature* **2001,** *414* (6861), 359-367.

178. Su, Y. S.; Manthiram, A., A new approach to improve cycle performance of rechargeable lithium-sulfur batteries by inserting a free-standing MWCNT interlayer. *Chem Commun* **2012,** *48* (70), 8817-8819.

179. Zhang, S. S., New insight into liquid electrolyte of rechargeable lithium/sulfur battery. *Electrochim Acta* **2013,** *97*, 226-230.

180. Zeng, W. D.; Xing, J. H.; Chen, J. C. M.; Ng, K. Y. S.; Oshihara, K.; Cheng, M. M. C., Design of advanced thick anode for Li-ion battery by inserting a graphite/polymer buffer layer: An in-situ mechanical study. *Electrochim Acta* **2018,** *281*, 282-291.

181. Ji, L. W.; Rao, M. M.; Aloni, S.; Wang, L.; Cairns, E. J.; Zhang, Y. G., Porous carbon nanofiber-sulfur composite electrodes for lithium/sulfur cells. *Energ Environ Sci* **2011,**

4 (12), 5053-5059.

182. Han, P. X.; Yue, Y. H.; Wang, X. G.; Ma, W.; Dong, S. M.; Zhang, K. J.; Zhang, C. J.; Cui, G. L., Graphene nanosheet-titanium nitride nanocomposite for high performance electrochemical capacitors without extra conductive agent addition. *J Mater Chem* **2012,** *22* (47), 24918-24923.
183. Li, B.; Li, S. M.; Liu, J. H.; Wang, B.; Yang, S. B., Vertically Aligned Sulfur-Graphene Nanowalls on Substrates for Ultrafast Lithium-Sulfur Batteries. *Nano Lett* **2015,** *15* (5), 3073-3079.
184. Sun, L.; Kong, W. B.; Jiang, Y.; Wu, H. C.; Jiang, K. L.; Wang, J. P.; Fan, S. S., Super-aligned carbon nanotube/graphene hybrid materials as a framework for sulfur cathodes in high performance lithium sulfur batteries. *J Mater Chem A* **2015,** *3* (10), 5305-5312.
185. Xiao, L. F.; Cao, Y. L.; Xiao, J.; Schwenzer, B.; Engelhard, M. H.; Saraf, L. V.; Nie, Z. M.; Exarhos, G. J.; Liu, J., A Soft Approach to Encapsulate Sulfur: Polyaniline Nanotubes for Lithium-Sulfur Batteries with Long Cycle Life. *Adv Mater* **2012,** *24* (9), 1176-1181.
186. Sun, Z. H.; Zhang, J. Q.; Yin, L. C.; Hu, G. J.; Fang, R. P.; Cheng, H. M.; Li, F., Conductive porous vanadium nitride/graphene composite as chemical anchor of polysulfides for lithium-sulfur batteries. *Nat Commun* **2017,** *8*.
187. Li, C. C.; Shi, J. J.; Zhu, L.; Zhao, Y. Y.; Lu, J.; Xu, L. Q., Titanium nitride hollow nanospheres with strong lithium polysulfide chemisorption as sulfur hosts for advanced lithium-sulfur batteries. *Nano Res* **2018,** *11* (8), 4302-4312.
188. Li, Z.; Zhang, J. T.; Guan, B. Y.; Wang, D.; Liu, L. M.; Lou, X. W., A sulfur host based

on titanium monoxide@carbon hollow spheres for advanced lithium-sulfur batteries. *Nat Commun* **2016,** *7*.

189. Sakamoto, J. S.; Dunn, B., Vanadium oxide-carbon nanotube composite electrodes for use in secondary lithium batteries. *J Electrochem Soc* **2002,** *149* (1), A26-A30.
190. Han, S. C.; Kim, H. S.; Kang, Y. M.; Ahn, H. J.; Ahn, H. J., The effect of large surface area nickel on the cycle life of sulfur cathode for lithium/sulfur battery. *Elec Soc S* **2003**, 381-388.
191. Liu, X.; Huang, J. Q.; Zhang, Q.; Mai, L. Q., Nanostructured Metal Oxides and Sulfides for Lithium-Sulfur Batteries. *Adv Mater* **2017,** *29* (20).
192. Tao, X. Y.; Wang, J. G.; Ying, Z. G.; Cai, Q. X.; Zheng, G. Y.; Gan, Y. P.; Huang, H.; Xia, Y.; Liang, C.; Zhang, W. K.; Cui, Y., Strong Sulfur Binding with Conducting Magneli-Phase TinO2n-1 Nanomaterials for Improving Lithium-Sulfur Batteries. *Nano Lett* **2014,** *14* (9), 5288-5294.
193. Liang, X.; Garsuch, A.; Nazar, L. F., Sulfur Cathodes Based on Conductive MXene Nanosheets for High-Performance Lithium-Sulfur Batteries. *Angew Chem Int Edit* **2015,** *54* (13), 3907-3911.
194. Zeng, W. D.; Wang, Z.; Cheng, M. M. C.; Ng, K. Y. S., Structured Titanium Nitride Nanotube Arrays/Sulfur Composite as Cathode Materials for Advanced Lithium Sulfur Battery. *J Electrochem Soc* **2018,** *165* (5), A1011-A1018.
195. Sharma, S.; Cui, Y.; He, Q.; Mohammadi, R.; Li, Z. G., Data-driven optimization of railway maintenance for track geometry. *Transport Res C-Emer* **2018,** *90*, 34-58.
196. Zhao, M. Q.; Liu, X. F.; Zhang, Q.; Tian, G. L.; Huang, J. Q.; Zhu, W. C.; Wei, F., Graphene/Single-Walled Carbon Nanotube Hybrids: One-Step Catalytic Growth and

Applications for High-Rate Li-S Batteries. *Acs Nano* **2012,** *6* (12), 10759-10769.

197. Peng, H. J.; Huang, J. Q.; Zhao, M. Q.; Zhang, Q.; Cheng, X. B.; Liu, X. Y.; Qian, W. Z.; Wei, F., Nanoarchitectured Graphene/CNT@Porous Carbon with Extraordinary Electrical Conductivity and Interconnected Micro/Mesopores for Lithium- Sulfur Batteries. *Adv Funct Mater* **2014,** *24* (19), 2772-2781.
198. Manthiram, A.; Chung, S. H.; Zu, C. X., Lithium-Sulfur Batteries: Progress and Prospects. *Adv Mater* **2015,** *27* (12), 1980-2006.
199. Sun, L.; Li, M. Y.; Jiang, Y.; Kong, W. B.; Jiang, K. L.; Wang, J. P.; Fan, S. S., Sulfur Nanocrystals Confined in Carbon Nanotube Network As a Binder-Free Electrode for High-Performance Lithium Sulfur Batteries. *Nano Lett* **2014,** *14* (7), 4044-4049.
200. Song, J. X.; Gordin, M. L.; Xu, T.; Chen, S. R.; Yu, Z. X.; Sohn, H.; Lu, J.; Ren, Y.; Duan, Y. H.; Wang, D. H., Strong Lithium Polysulfide Chemisorption on Electroactive Sites of Nitrogen-Doped Carbon Composites For High-Performance Lithium-Sulfur Battery Cathodes. *Angew Chem Int Edit* **2015,** *54* (14), 4325-4329.
201. Li, X. L.; Cao, Y. L.; Qi, W.; Saraf, L. V.; Xiao, J.; Nie, Z. M.; Mietek, J.; Zhang, J. G.; Schwenzer, B.; Liu, J., Optimization of mesoporous carbon structures for lithium-sulfur battery applications. *J Mater Chem* **2011,** *21* (41), 16603-16610.
202. He, Z.; Mansfeld, F., Exploring the use of electrochemical impedance spectroscopy (EIS) in microbial fuel cell studies. *Energ Environ Sci* **2009,** *2* (2), 215-219.
203. Mao, Y. Y.; Li, G. R.; Guo, Y.; Li, Z. P.; Liang, C. D.; Peng, X. S.; Lin, Z., Foldable interpenetrated metal-organic frameworks/carbon nanotubes thin film for lithium-sulfur batteries. *Nat Commun* **2017,** *8*.
204. Li, Z.; Wu, H. B.; Lou, X. W., Rational designs and engineering of hollow micro-

/nanostructures as sulfur hosts for advanced lithium-sulfur batteries. *Energ Environ Sci* **2016,** *9* (10), 3061-3070.

205. Zhou, G. M.; Pei, S. F.; Li, L.; Wang, D. W.; Wang, S. G.; Huang, K.; Yin, L. C.; Li, F.; Cheng, H. M., A Graphene-Pure-Sulfur Sandwich Structure for Ultrafast, Long-Life Lithium-Sulfur Batteries. *Adv Mater* **2014,** *26* (4), 625-631.
206. Zhou, G. M.; Yin, L. C.; Wang, D. W.; Li, L.; Pei, S. F.; Gentle, I. R.; Li, F.; Cheng, H. M., Fibrous Hybrid of Graphene and Sulfur Nanocrystals for High-Performance Lithium-Sulfur Batteries. *Acs Nano* **2013,** *7* (6), 5367-5375.
207. Ates, M. N.; Mukerjee, S.; Abraham, K. M., A Li-Rich Layered Cathode Material with Enhanced Structural Stability and Rate Capability for Li-on Batteries. *J Electrochem Soc* **2014,** *161* (3), A355-A363.
208. Kang, H. S.; Sun, Y. K., Freestanding Bilayer Carbon-Sulfur Cathode with Function of Entrapping Polysulfide for High Performance Li-S Batteries. *Adv Funct Mater* **2016,** *26* (8), 1225-1232.
209. Li, N. W.; Zheng, M. B.; Lu, H. L.; Hu, Z. B.; Shen, C. F.; Chang, X. F.; Ji, G. B.; Cao, J. M.; Shi, Y., High-rate lithium-sulfur batteries promoted by reduced graphene oxide coating. *Chem Commun* **2012,** *48* (34), 4106-4108.
210. Zheng, W.; Liu, Y. W.; Hu, X. G.; Zhang, C. F., Novel nanosized adsorbing sulfur composite cathode materials for the advanced secondary lithium batteries. *Electrochim Acta* **2006,** *51* (7), 1330-1335.
211. Xu, L. F.; Li, J. Q.; Ouyang, M. G.; Hua, J. F.; Yang, G., Multi-mode control strategy for fuel cell electric vehicles regarding fuel economy and durability. *Int J Hydrogen Energ* **2014,** *39* (5), 2374-2389.

212. Wang, H. W.; Zhang, X. B.; Ouyang, M. G., Energy consumption of electric vehicles based on real-world driving patterns: A case study of Beijing. *Appl Energ* **2015,** *157*, 710-719.

213. Song, Z. Y.; Li, J. Q.; Han, X. B.; Xu, L. F.; Lu, L. G.; Ouyang, M. G.; Hofmann, H., Multi-objective optimization of a semi-active battery/supercapacitor energy storage system for electric vehicles. *Appl Energ* **2014,** *135*, 212-224.

214. Song, Z. Y.; Hofmann, H.; Li, J. Q.; Han, X. B.; Zhang, X. W.; Ouyang, M. G., A comparison study of different semi-active hybrid energy storage system topologies for electric vehicles. *J Power Sources* **2015,** *274*, 400-411.

215. Hausbrand, R.; Stratmann, M.; Rohwerder, M., The physical meaning of electrode potentials at metal surfaces and polymer/metal interfaces: Consequences for delamination. *J Electrochem Soc* **2008,** *155* (7), C369-C379.

216. Haftbaradaran, H.; Xiao, X. C.; Verbrugge, M. W.; Gao, H. J., Method to deduce the critical size for interfacial delamination of patterned electrode structures and application to lithiation of thin-film silicon islands. *J Power Sources* **2012,** *206*, 357-366.

217. Rahman, M. A.; Song, G. S.; Bhatt, A. I.; Wong, Y. C.; Wen, C. E., Nanostructured Silicon Anodes for High-Performance Lithium-Ion Batteries. *Adv Funct Mater* **2016,** *26* (5), 647-678.

218. Hwang, T. H.; Lee, Y. M.; Kong, B. S.; Seo, J. S.; Choi, J. W., Electrospun Core-Shell Fibers for Robust Silicon Nanoparticle-Based Lithium Ion Battery Anodes. *Nano Lett* **2012,** *12* (2), 802-807.

219. Guo, J. C.; Yang, Z. C.; Archer, L. A., Mesoporous silicon@carbon composites via

nanoparticle-seeded dispersion polymerization and their application as lithium-ion battery anode materials. *J Mater Chem A* **2013,** *1* (18), 5709-5714.

220. Chan, C. K.; Peng, H. L.; Liu, G.; McIlwrath, K.; Zhang, X. F.; Huggins, R. A.; Cui, Y., High-performance lithium battery anodes using silicon nanowires. *Nat Nanotechnol* **2008,** *3* (1), 31-35.
221. Chan, C. K.; McDowell, M. T.; Cui, Y., Silicon Nanowire Electrodes for Lithium-Ion Battery Negative Electrodes. *Nanomaterials for Lithium-Ion Batteries: Fundamentals and Applications* **2014**, 1-68.
222. Zheng, H. H.; Li, J.; Song, X. Y.; Liu, G.; Battaglia, V. S., A comprehensive understanding of electrode thickness effects on the electrochemical performances of Li-ion battery cathodes. *Electrochim Acta* **2012,** *71*, 258-265.
223. Datta, M. K.; Maranchi, J.; Chung, S. J.; Epur, R.; Kadakia, K.; Jampani, P.; Kumta, P. N., Amorphous silicon-carbon based nano-scale thin film anode materials for lithium ion batteries. *Electrochim Acta* **2011,** *56* (13), 4717-4723.
224. Singh, M.; Kaiser, J.; Hahn, H., Thick Electrodes for High Energy Lithium Ion Batteries. *J Electrochem Soc* **2015,** *162* (7), A1196-A1201.
225. Zhou, X. S.; Wan, L. J.; Guo, Y. G., Electrospun Silicon Nanoparticle/Porous Carbon Hybrid Nanofibers for Lithium-Ion Batteries. *Small* **2013,** *9* (16), 2684-2688.
226. Sethuraman, V. A.; Van Winkle, N.; Abraham, D. P.; Bower, A. F.; Guduru, P. R., Real-time stress measurements in lithium-ion battery negative-electrodes. *J Power Sources* **2012,** *206*, 334-342.
227. Sethuraman, V. A.; Srinivasan, V.; Bower, A. F.; Guduru, P. R., In Situ Measurements of Stress-Potential Coupling in Lithiated Silicon. *J Electrochem Soc* **2010,** *157* (11),

A1253-A1261.

228. Sethuraman, V. A.; Nguyen, A.; Chon, M. J.; Nadimpalli, S. P. V.; Wang, H.; Abraham, D. P.; Bower, A. F.; Shenoy, V. B.; Guduru, P. R., Stress Evolution in Composite Silicon Electrodes during Lithiation/Delithiation. *J Electrochem Soc* **2013,** *160* (4), A739-A746.

229. Sethuraman, V. A.; Chon, M. J.; Shimshak, M.; Van Winkle, N.; Guduru, P. R., In situ measurement of biaxial modulus of Si anode for Li-ion batteries. *Electrochem Commun* **2010,** *12* (11), 1614-1617.

230. Sethuraman, V. A.; Chon, M. J.; Shimshak, M.; Srinivasan, V.; Guduru, P. R., In situ measurements of stress evolution in silicon thin films during electrochemical lithiation and delithiation. *J Power Sources* **2010,** *195* (15), 5062-5066.

231. Dini, D.; Passerini, S.; Scrosati, B.; Decker, F., Stress changes in electrochromic thin film electrodes: Laser beam deflection method (LBDM) as a tool for the analysis of intercalation processes. *Sol Energ Mat Sol C* **1999,** *56* (3-4), 213-221.

232. Decker, F.; Pileggi, R.; Passerini, S.; Scrosati, B., A Comparison of the Electrochromic Behavior and the Mechanical-Properties of Wo3 and Niox Thin-Film Electrodes. *J Electrochem Soc* **1991,** *138* (11), 3182-3186.

233. Yi, R.; Dai, F.; Gordin, M. L.; Chen, S. R.; Wang, D. H., Micro-sized Si-C Composite with Interconnected Nanoscale Building Blocks as High-Performance Anodes for Practical Application in Lithium-Ion Batteries. *Adv Energy Mater* **2013,** *3* (3), 295-300.

234. Yang, J. H.; Chen, J.; Cheng, M. M. C., In-situ Monitor Electrochemical Processes in Batteries Using Vibrating Microcantilevers. *P Ieee Int Freq Cont* **2014**, 28-31.

235. Wang, S.; Gao, Z. S.; Li, M. J.; Ye, J. F.; Cheng, J. L.; Yang, Z. M.; Yuan, Q., Design, assembly and calibration of white-light microscopy interferometer. *Proc Spie* **2015,** *9677*.

236. Kim, S. W.; Kim, G. H., Thickness-profile measurement of transparent thin-film layers by white-light scanning interferometry. *Appl Optics* **1999,** *38* (28), 5968-5973.

237. Kim, G. H.; Kim, S. W., White light scanning interferometry for thickness measurement of thin film layers. *P Soc Photo-Opt Ins* **1999,** *3783*, 239-246.

238. Timoshenko, S., Analysis of bi-metal thermostats. *J Opt Soc Am Rev Sci* **1925,** *11* (3), 233-255.

239. Shapiro, B.; Smela, E., Bending actuators with maximum curvature and force and zero interfacial stress. *J Intel Mat Syst Str* **2007,** *18* (2), 181-186.

240. Gomadam, P. M.; Weidner, J. W., Modeling volume changes in porous electrodes. *J Electrochem Soc* **2006,** *153* (1), A179-A186.

241. Garrick, T. R.; Kanneganti, K.; Huang, X. Y.; Weidner, J. W., Modeling Volume Change due to Intercalation into Porous Electrodes. *J Electrochem Soc* **2014,** *161* (8), E3297-E3301.

242. Langlois, E. D.; Shaw, G. A.; Kramar, J. A.; Pratt, J. R.; Hurley, D. C., Spring constant calibration of atomic force microscopy cantilevers with a piezosensor transfer standard. *Rev Sci Instrum* **2007,** *78* (9).

243. Derjaguin, Muller, and Toporov Theory of Adhesion. In *Encyclopedia of Tribology*, Wang, Q. J.; Chung, Y.-W., Eds. Springer US: Boston, MA, 2013; pp 710-710.

244. Hopcroft, M. A.; Nix, W. D.; Kenny, T. W., What is the Young's Modulus of Silicon? *J Microelectromech S* **2010,** *19* (2), 229-238.

245. Grimsditch, M., Shear Elastic-Modulus of Graphite. *J Phys C Solid State* **1983,** *16* (5), L143-L144.

246. Fedotov, A. F., Prediction of effective elasticity moduli of porous composite materials. *Russian Journal of Non-Ferrous Metals* **2016,** *57* (3), 251-255.

247. Zhang, S. D.; Sakane, M.; Nagasawa, T.; Kobayashi, K., Mechanical Properties of Copper Thin Films Used in Electronic Devices. *Procedia Engineer* **2011,** *10*, 1497-1502.

248. Yoshio, M.; Wang, H. Y.; Fukuda, K.; Hara, Y.; Adachi, Y., Effect of carbon coating on electrochemical performance of treated natural graphite as lithium-ion battery anode material. *J Electrochem Soc* **2000,** *147* (4), 1245-1250.

249. Nie, M. Y.; Chalasani, D.; Abraham, D. P.; Chen, Y. J.; Bose, A.; Lucht, B. L., Lithium Ion Battery Graphite Solid Electrolyte Interphase Revealed by Microscopy and Spectroscopy. *J Phys Chem C* **2013,** *117* (3), 1257-1267.

250. Wang, K. P.; Huang, Y. Y.; Chandra, A.; Hu, K. X., Interfacial shear stress, peeling stress, and die cracking stress in trilayer electronic assemblies. *Ieee T Compon Pack T* **2000,** *23* (2), 309-316.

251. Arora, P.; White, R. E.; Doyle, M., Capacity fade mechanisms and side reactions in lithium-ion batteries. *J Electrochem Soc* **1998,** *145* (10), 3647-3667.

252. Waag, W.; Kabitz, S.; Sauer, D. U., Experimental investigation of the lithium-ion battery impedance characteristic at various conditions and aging states and its influence on the application. *Appl Energ* **2013,** *102*, 885-897.

253. Xing, J. H.; Wu, S. Y.; Ng, K. Y. S., Electrodeposition of ultrathin nickel-cobalt double hydroxide nanosheets on nickel foam as high-performance supercapacitor electrodes.

Rsc Adv **2015,** *5* (108), 88780-88786.

254. Cannarella, J.; Leng, C. Z.; Arnold, C. B., On the Coupling Between Stress and Voltage in Lithium Ion Pouch Cells. *Proc Spie* **2014,** *9115*.
255. Zhou, X. S.; Cao, A. M.; Wan, L. J.; Guo, Y. G., Spin-coated silicon nanoparticle/graphene electrode as a binder-free anode for high-performance lithium-ion batteries. *Nano Res* **2012,** *5* (12), 845-853.
256. Yoon, I.; Abraham, D. P.; Lucht, B. L.; Bower, A. F.; Guduru, P. R., In Situ Measurement of Solid Electrolyte Interphase Evolution on Silicon Anodes Using Atomic Force Microscopy. *Adv Energy Mater* **2016,** *6* (12).
257. Yao, Y.; McDowell, M. T.; Ryu, I.; Wu, H.; Liu, N. A.; Hu, L. B.; Nix, W. D.; Cui, Y., Interconnected Silicon Hollow Nanospheres for Lithium-Ion Battery Anodes with Long Cycle Life. *Nano Lett* **2011,** *11* (7), 2949-2954.
258. Wang, X. L.; An, K.; Cai, L.; Feng, Z. L.; Nagler, S. E.; Daniel, C.; Rhodes, K. J.; Stoica, A. D.; Skorpenske, H. D.; Liang, C. D.; Zhang, W.; Kim, J.; Qi, Y.; Harris, S. J., Visualizing the chemistry and structure dynamics in lithium-ion batteries by in-situ neutron diffraction. *Sci Rep-Uk* **2012,** *2*.
259. Sim, B.; Kim, E. H.; Park, J.; Lee, M., Highly enhanced mechanical stability of indium tin oxide film with a thin Al buffer layer deposited on plastic substrate. *Surf Coat Tech* **2009,** *204* (3), 309-312.
260. Kim, T.; Mo, Y. H.; Nahm, K. S.; Oh, S. M., Carbon nanotubes (CNTs) as a buffer layer in silicon/CNTs composite electrodes for lithium secondary batteries. *J Power Sources* **2006,** *162* (2), 1275-1281.
261. Kim, G. S.; Lee, S. Y.; Hahn, J. H.; Lee, B. Y.; Han, J. G.; Lee, J. H.; Lee, S. Y., Effects

of the thickness of Ti buffer layer on the mechanical properties of TiN coatings. *Surf Coat Tech* **2003,** *171* (1-3), 83-90.

262. Cheng, X. B.; Yan, C.; Huang, J. Q.; Li, P.; Zhu, L.; Zhao, L. D.; Zhang, Y. Y.; Zhu, W. C.; Yang, S. T.; Zhang, Q., The gap between long lifespan Li-S coin and pouch cells: The importance of lithium metal anode protection. *Energy Storage Mater* **2017,** *6*, 18-25.
263. Aurbach, D., Introduction to the Focus Issue on Lithium-Sulfur Batteries: Materials, Mechanisms, Modeling, and Applications. *J Electrochem Soc* **2018,** *165* (1), Y1-Y1.
264. Lee, Y. M.; Choi, N. S.; Park, J. H.; Park, J. K., Electrochemical performance of lithium/sulfur batteries with protected Li anodes. *J Power Sources* **2003,** *119*, 964-972.
265. Xi, X. T.; Li, W. H.; Hou, B. H.; Yang, Y.; Gu, Z. Y.; Wu, X. L., Dendrite-Free Lithium Anode Enables the Lithium//Graphite Dual-Ion Battery with Much Improved Cyclic Stability. *ACS Appl Energ Mater* **2019,** *2* (1), 201-206.
266. Zhao, C. Z.; Chen, P. Y.; Zhang, R.; Chen, X.; Li, B. Q.; Zhang, X. Q.; Cheng, X. B.; Zhang, Q., An ion redistributor for dendrite-free lithium metal anodes. *Sci Adv* **2018,** *4* (11).
267. Zhang, K.; Lee, G. H.; Park, M.; Li, W. J.; Kang, Y. M., Recent Developments of the Lithium Metal Anode for Rechargeable Non-Aqueous Batteries. *Adv Energy Mater* **2016,** *6* (20).
268. Xu, W.; Wang, J. L.; Ding, F.; Chen, X. L.; Nasybutin, E.; Zhang, Y. H.; Zhang, J. G., Lithium metal anodes for rechargeable batteries. *Energ Environ Sci* **2014,** *7* (2), 513-537.

269. Kanamura, K., Promising anode active materials for the coming lithium secondary batteries .4. Morphological control for lithium metal as anode material of rechargeable lithium battery. *Denki Kagaku* **1997,** *65* (9), 722-729.

270. Ma, G. Q.; Wen, Z. Y.; Wang, Q. S.; Shen, C.; Jin, J.; Wu, X. W., Enhanced cycle performance of a Li-S battery based on a protected lithium anode. *J Mater Chem A* **2014,** *2* (45), 19355-19359.

271. Xu, X. L.; Wang, S. J.; Wang, H.; Xu, B.; Hu, C.; Jin, Y.; Liu, J. B.; Yan, H., The suppression of lithium dendrite growth in lithium sulfur batteries: A review. *J Energy Storage* **2017,** *13*, 387-400.

272. Yu, B. C.; Park, K.; Jang, J. H.; Goodenough, J. B., Cellulose-Based Porous Membrane for Suppressing Li Dendrite Formation in Lithium-Sulfur Battery. *Acs Energy Lett* **2016,** *1* (3), 633-637.

273. Cheng, X. B.; Peng, H. J.; Huang, J. Q.; Wei, F.; Zhang, Q., Dendrite-Free Nanostructured Anode: Entrapment of Lithium in a 3D Fibrous Matrix for Ultra-Stable Lithium-Sulfur Batteries. *Small* **2014,** *10* (21), 4257-4263.

274. Wu, F.; Qian, J.; Chen, R. J.; Lu, J.; Li, L.; Wu, H. M.; Chen, J. Z.; Zhao, T.; Ye, Y. S.; Amine, K., An Effective Approach To Protect Lithium Anode and Improve Cycle Performance for Li-S Batteries. *Acs Appl Mater Inter* **2014,** *6* (17), 15542-15549.

275. Choi, N. S.; Lee, Y. M.; Seol, W.; Lee, J. A.; Park, J. K., Protective coating of lithium metal electrode for interfacial enhancement with gel polymer electrolyte. *Solid State Ionics* **2004,** *172* (1-4), 19-24.

276. Imanishi, N.; Hasegawa, S.; Zhang, T.; Hirano, A.; Takeda, Y.; Yamamoto, O., Lithium anode for lithium-air secondary batteries. *J Power Sources* **2008,** *185* (2), 1392-1397.

277. Zheng, G. Y.; Lee, S. W.; Liang, Z.; Lee, H. W.; Yan, K.; Yao, H. B.; Wang, H. T.; Li, W. Y.; Chu, S.; Cui, Y., Interconnected hollow carbon nanospheres for stable lithium metal anodes. *Nat Nanotechnol* **2014,** *9* (8), 618-623.

278. Lin, Z.; Liu, Z. C.; Fu, W. J.; Dudney, N. J.; Liang, C. D., Phosphorous Pentasulfide as a Novel Additive for High-Performance Lithium-Sulfur Batteries. *Adv Funct Mater* **2013,** *23* (8), 1064-1069.

279. Yan, C.; Cheng, X. B.; Zhao, C. Z.; Huang, J. Q.; Yang, S. T.; Zhang, Q., Lithium metal protection through in-situ formed solid electrolyte interphase in lithium-sulfur batteries: The role of polysulfides on lithium anode. *J Power Sources* **2016,** *327*, 212-220.

280. Liu, S.; Li, G. R.; Gao, X. P., Lanthanum Nitrate As Electrolyte Additive To Stabilize the Surface Morphology of Lithium Anode for Lithium-Sulfur Battery. *Acs Appl Mater Inter* **2016,** *8* (12), 7783-7789.

281. Yan, C.; Yao, Y. X.; Chen, X.; Cheng, X. B.; Zhang, X. Q.; Huang, J. Q.; Zhang, Q., Lithium Nitrate Solvation Chemistry in Carbonate Electrolyte Sustains High-Voltage Lithium Metal Batteries. *Angew Chem Int Edit* **2018,** *57* (43), 14055-14059.

282. Liu, Y. Y.; Lin, D. C.; Li, Y. Z.; Chen, G. X.; Pei, A.; Nix, O.; Li, Y. B.; Cui, Y., Solubility-mediated sustained release enabling nitrate additive in carbonate electrolytes for stable lithium metal anode. *Nat Commun* **2018,** *9*.

283. Jozwiuk, A.; Berkes, B. B.; Weiss, T.; Sommer, H.; Janek, J.; Brezesinski, T., The critical role of lithium nitrate in the gas evolution of lithium-sulfur batteries. *Energ Environ Sci* **2016,** *9* (8), 2603-2608.

284. Zu, C. X.; Manthiram, A., Stabilized Lithium-Metal Surface in a Polysulfide-Rich

Environment of Lithium-Sulfur Batteries. *J Phys Chem Lett* **2014,** *5* (15), 2522-2527.

285. Jing, H. K.; Kong, L. L.; Liu, S.; Li, G. R.; Gao, X. P., Protected lithium anode with porous Al2O3 layer for lithium-sulfur battery. *J Mater Chem A* **2015,** *3* (23), 12213-12219.

286. Tellier, C. R., Effect of Crystal Orientation on the Surface Texture of Chemically Etched Quartz Plates, the Case of Cuts Close to the at-Cut. *Ieee T Ultrason Ferr* **1986,** *33* (1), 127-127.

287. Torres, W. R.; Davia, F.; del Pozo, M.; Tesio, A. Y.; Calvo, E. J., EQCM and RDE/RRDE Study of Soluble Iron Phthalocyanine Bifunctional Catalyst for the Lithium-Oxygen Battery. *J Electrochem Soc* **2017,** *164* (14), A3785-A3792.

288. Wu, H. L.; Huff, L. A.; Esbenshade, J. L.; Gewirth, A. A., In Situ EQCM Study Examining Irreversible Changes the Sulfur-Carbon Cathode in Lithium-Sulfur Batteries. *Acs Appl Mater Inter* **2015,** *7* (37), 20820-20828.

289. Barchasz, C.; Lepretre, J. C.; Patoux, S.; Alloin, F., Electrochemical properties of ether-based electrolytes for lithium/sulfur rechargeable batteries. *Electrochim Acta* **2013,** *89*, 737-743.

290. Cruz, R.; Mendez, B. A.; Monroy, M.; Gonzalez, I., Cyclic voltammetry applied to evaluate reactivity in sulfide mining residues. *Appl Geochem* **2001,** *16* (14), 1631-1640.

ABSTRACT

NOVEL CATHODE FRAMEWORK, EFFECTIVE ELECTROLYTE MODIFICATION, AND ELECTRODE STRUCTURAL IMPROVEMENT OF HIGH-PERFORMANCE LITHIUM SULFUR BATTERIES

by

WENDUO ZENG

August 2019

Advisors: Dr. Simon Ng and Dr. Mark Cheng

Major: Materials Science and Engineering

Degree: Doctor of Philosophy

Firstly, TiN nanotube arrays have been investigated as an effective skeleton in cathode of lithium sulfur batteries. A series of TiN nanotubes with various diameter and length have been synthesized and tested. Moreover, graphene nanoplatelets have been utilized as a structural anchor to support the TiN nanotubes, and the synergetic effect of composite material and its enhancement on Li-S battery electrochemical performance and cycling stability have been studied. Secondly, the improvement of electrode structural design has been evaluated for their effectiveness by using an in-situ characterization method with electrochemical testing and structural characterization. Lastly, the facile method of using transition metal cations as electrolyte additive has been proven to be capable of protecting lithium metal anode effectively.

As a summary, the result of the research could result in a more rational design of novel lithium sulfur batteries with high performance. It serves as an alternative to conventional lithium ion batteries, rendering more practical approaches possible to large-scale

production of electric automotive with lower cost and wider application of digital electronics.

AUTOBIOGRAPHICAL STATEMENT

EDUCATION

M.S., Materials Science, Stony Brook University, May 2015

B.E., Materials Science, University of Science and Technology Beijing, June 2009

PUBLICATIONS

1. Wenduo Zeng, Junheng Xing, K.Y. Simon Ng and Mark Ming-Cheng Cheng, "Design of advanced anode for Li-ion battery by inserting a graphite/polymer buffer layer: an in-situ mechanical study," Electrochimica Acta, Volume 281, 10 August 2018, Pages 282-291.
2. Wenduo Zeng, Zhao Wang, Mark Ming-Cheng Cheng and K. Y. Simon Ng, "Structured titanium nitride nanotube arrays as novel cathode materials for advanced lithium sulfur battery," Journal of the Electrochemical Society, 2018 volume 165, issue 5, A1011-A1018.
3. Wenduo Zeng, Mark Ming-Cheng Cheng and K. Y. Simon Ng, "Novel Cathode Framework of Nanostructured Titanium Nitride/Graphene for Advanced Lithium Sulfur Batteries," Submitted to ChemElectroChem, 2019.
4. Wenduo Zeng, Mark Ming-Cheng Cheng and K. Y. Simon Ng, "Novel Transition Metal Cations as Electrolyte Additives for Lithium Sulfur Batteries", to be submitted to Journal of Applied Electrochemistry, 2019.
5. Naisheng Jiang, Mani Sen, Wenduo Zeng, Zhizhao Chen, Justin Cheung, Maya Endoh, Koga, Tadanori Koga, Masafumi Fukuto, Guangcui Yuan, Sushil Satija, Jan Michael Carrillo, Bobby Sumpter, "Structure-induced switching of interpolymer adhesion at a solid-polymer melt interface," 2018, **14**, 1108-1119.
6. Naisheng Jiang, Jiaxun Wang, Xiaoyu Di, Justin Cheung, Wenduo Zeng, Maya K. Endoh, Tadanori Koga and Sushil K. Satija, "Nanoscale adsorbed structures as a robust approach for tailoring polymer film stability," Soft Matter, 12, 1801-1809, 2016.